

Investigation of the longitudinal charge distribution of electron bunches at the VUV-FEL using the transverse deflecting cavity LOLA

Diploma Thesis
of
Andy Bolzmann

submitted to the
Department of Physics of the Bayerische Julius-Maximilians Universität Würzburg

prepared at
Deutsches Elektronen-Synchrotron (DESY), Hamburg

Hamburg, Oktober 2005

Abstract

The Vacuum-Ultraviolet Free Electron Laser (VUV-FEL) at DESY in Hamburg produces photon pulses with high brilliance in the VUV up to soft X-ray regime. Since electron bunches with a high peak-current are required, investigation of the longitudinal bunch shape and bunch length is necessary. The transverse deflecting radio-frequency (RF) cavity LOLA streaks the electron beam and makes the longitudinal charge-distribution visible on a screen by optical transition radiation. This allows for measurements with a resolution of down to 17 fs.

In this thesis the commissioning and first measurements of LOLA are discussed. The realization of the synchronization and the calibration of the experimental-setup are presented. The investigation of the longitudinal charge-distribution reveals a rich substructure within the bunches, for example a double-spike is seen in the head, followed by a long tail. The bunch shape is found to be strongly dependent on the phase of the RF field of the accelerating modules. Because the spike and the tail are seen distinctly with LOLA, it was possible to measure the transverse emittance of the spike.

Zusammenfassung

Der Vacuum-Ultraviolett-Freie-Elektronen-Laser (VUV-FEL) am DESY in Hamburg erzeugt Lichtpulse mit hoher Brillianz im Bereich vom VUV bis weicher Röntgenstrahlung. Weil dazu Elektronenpakete mit hohem Spitzenstrom benötigt werden, ist die Erforschung der longitudinalen Struktur und der Länge der Elektronenpakete notwendig. Die transversal ablenkende Hochfrequenz-Kavität LOLA schert den Elektronenstrahl und macht die longitudinale Ladungsverteilung mittels optischer Übergangsstrahlung sichtbar. Damit sind Messungen mit einer Auflösung von bis zu 17 fs möglich.

Im Rahmen dieser Arbeit werden die Inbetriebnahme von LOLA und erste Messungen diskutiert. Die Verwirklichung der Synchronisation und die Kalibration des experimentellen Aufbaus werden dargelegt. Die Untersuchung der longitudinalen Ladungsverteilung enthüllte eine reichhaltige Unterstruktur der Elektronenpakete, zum Beispiel in Form einer Doppelspitze im vorderen Bereich, gefolgt von einem langen Schweif. Diese Struktur hängt stark von der Phase der Hochfrequenzfelder in den Beschleunigermodulen ab. Weil Kopf und Schweif der Elektronenpakete mit Hilfe von LOLA getrennt darstellbar sind, konnte ebenfalls die transversale Emittanz des Kopfes gemessen werden.

Figure on the title page: The longitudinal charge distribution of an electron bunch at the TTF free electron laser while delivering SASE laser radiation for users.

Andy Bolzmann
Deutsches Elektronen-Synchrotron
Notkestraße 85
22607 Hamburg, Germany
e-mail: andy.bolzmann@desy.de

German title:
Untersuchung der longitudinalen Ladungsverteilung von Elektronenpaketen am VUV-FEL mit Hilfe der transversal ablenkenden Kavität
LOLA

Published under DESY report numbers:
DESY-THESIS-2005-046
TESLA-FEL 2005-04

Printed by the DESY copy center.
This document was typeset using \LaTeX and KOMA-Script.

Contents

1 Introduction	1	4.1 The frequency generating setup	18
1.1 An overview of the generations of synchrotron radiation sources	1	4.2 Temporary solution	19
1.2 The VUV-FEL	2	5 Calibration measurements	20
2 Theory	3	5.1 Measurement of the RF power of LOLA	20
2.1 Linear beam dynamics	3	5.2 The phaseshifter	21
2.1.1 The transfer-matrix formalism	3	5.3 Correlation between the dimensions of OTR screen and CCD camera	22
2.1.2 The Twiss-Parameters	4	5.4 Position dependence of the sensitivity at the OTR station	23
2.1.3 The emittance	4	5.4.1 Comparison with theoretical values	23
2.2 The bunch compressor	5	5.5 The longitudinal resolution	25
2.2.1 An estimation of the bunch length	7	6 Measurements	28
2.2.2 Coherent synchrotron radiation	9	6.1 Longitudinal charge distribution	28
2.3 The field distribution of the RF of LOLA	9	6.2 ACC1 phase scan	30
3 The experimental setup around LOLA and the principle of measurement	12	6.2.1 Data analysis	30
3.1 The cavity	12	6.2.2 Comparison with simulations	30
3.2 The screen	13	6.2.3 Discussion of the results	31
3.3 The camera and its optical system	13	6.3 Emittance of the spike	32
3.3.1 The resolution of the optical system	13	6.3.1 Considerations on the experimental setup	32
3.4 The kicker	14	6.3.2 Data analysis	33
3.5 The beam position monitors	15	6.3.3 Comparison of bunch parameters from different origins	33
3.6 The magnets around LOLA	16	7 Conclusion	35
3.6.1 The quadrupole magnets	16	A The Panofsky-Wenzel theorem	36
3.6.2 The steerer magnets	16	B Tables	37
3.7 The collimator	16		
4 Realization of the synchronization	18		

List of Figures

1.1	Peak brilliance of various synchrotron radiation sources	1	5.3	Calibration of the power measurement	21
1.2	Layout of the VUV-FEL	2	5.4	Calibration of the power measurement using two diodes	21
2.1	Definition of the coordinate-system	3	5.5	Vertical kick vs. RF phase	21
2.2	The phase-space ellipse	5	5.6	Expected zero-crossing distances vs. RF phase at display	22
2.3	The principle of bunch compression using a magnetic C-chicane	6	5.7	Behavior of the phaseshifter measured with a network analyzer	22
2.4	The principle of longitudinal phase-space shaping	6	5.8	A photograph of the screen holder showing the calibration marks	22
2.5	A simulation of the influence of bunch compressors	7	5.9	Position dependence of the OTR intensity	23
2.6	Principle of energy transfer due to CSR	9	5.10	Examples for integration of OTR using spherical angles	24
2.7	Energy loss per unit length along the bunch due to CSR	9	5.11	Coordinate transformation from spherical to lens-parameters	24
2.8	Field pattern of the TM_{01} - and the TM_{11} -mode	10	5.12	Position dependence of intensity compared with theoretical predictions	25
2.9	Time snap-shot of the electric field distribution of the TM_{11} -mode	11	5.13	Principle of resolution calibration	26
3.1	The layout of the facility around LOLA	12	5.14	Dependence of the RF phase on the vertical position at the screen of LOLA	26
3.2	Cut-away view of the cavity LOLA	12	6.1	Bunch shape and longitudinal profiles at different RF power	28
3.3	The off-axis screen	13	6.2	Spike width in fs vs. RF power	29
3.4	Sketch of the optical system of the camera of LOLA	13	6.3	Spike width in μm at the screen vs. deflecting voltage	29
3.5	Measurement of the MTF	14	6.4	Beam images and longitudinal profiles at different compressions	30
3.6	The modulation transfer function of the optical system	14	6.5	The bunch length at different compressions	30
3.7	The transfer function of the optical system	14	6.6	Comparison of measured and simulated longitudinal profiles of [Kim05]	31
3.8	Sketch of the timing of the kicker pulse	15	6.7	Comparison of measured and simulated longitudinal profiles of [Doh05]	31
3.9	Dispersion at the screen of LOLA	15	6.8	Examples of bunches at different quadrupole currents	33
3.10	Principle of a stripline BPM	15	6.9	Horizontal and vertical spike-width vs. quadrupole current	33
3.11	The focussing properties of a quadrupole	16			
4.1	Synchronization of the RF with the accelerating modules	18			
5.1	Principle of RF power measurement	20			
5.2	Characteristic curve of a diode	20			

List of Tables

6.1	Beam-parameters of the spike at the position of LOLA	33	B.1	Calibration of the RF power measurement	37
6.2	Widths of unstreaked bunches at the screen of LOLA	34	B.2	Behavior of the phaseshifter measured with a network analyzer	37
			B.3	A precise power measurement using attenuators .	38

1 Introduction

In this thesis, the theory, commissioning, and results of the transverse deflecting cavity, LOLA IV, for longitudinal bunch shape and bunch length measurements at the DESY Vavuum-Ultraviolet Free Electron Laser (VUV-FEL) are presented. The design of the linear accelerator foresees bunch lengths in the order of 100 fs and below. This poses a serious challenge for diagnosing the longitudinal structure of these bunches. LOLA promises resolution down to 17 fs.

1.1 An overview of the generations of synchrotron radiation sources

Since its discovery by Floyd Haber in 1947 at the synchrotron accelerator facility of General Electric, the worlds understanding of synchrotron radiation has evolved from a disturbing side-effect of particle acceleration to a very important tool with applications in many fields of research. In the 60's, first experiments with (photo-electrons) spectroscopy were done. In the 70's scattering experiments profitted from the high intensity and spectral tunability of the synchrotron radiation generated in accelerator facilities. Today biologists investigate the submolecular structure of proteins, solid-state physicists and chemists analyze surfactants on semiconductors and earth-scientists irradiate very small samples of material in high-pressure chambers to research how the matter behaves under the extreme conditions within the interior of the earth.

The first experiments with synchrotron radiation at accelerator facilities were done parasitically, simultaneously with high-energy collision experiments, and were, therefore, dependent on their operating conditions. In spite of this, radiation sources of the 1st generation were more advantageous than the common laboratory sources, because of the polarization and the short pulse length.

Due to the success of the synchrotron-light experiments and the growing community of experimenters, particle storage-rings were built solely for the purpose of synchrotron-radiation production. The brilliance of the emitted light was 10^6 times higher than the light of a common cathode X-ray tube. The quality of these 2nd generation sources was improved by the introduction of wigglers and undulators. These insertion-devices of the 3rd generation consist of magnets, arranged in a spatially alternating structure that force the charged particles to oscillate transversely. The radiation emitted at each oscillation adds up and delivers, in combination with other improvements, a photon beam brilliance 6-10 orders of magnitude larger than the brilliance generated by sources of the 2nd generation.

Free electron lasers (FEL) are sometimes called the 4th generation of synchrotron radiation sources. The electron beam, accelerated in a linear accelerator or stored in a storage ring, produces laser radiation in undulators. Another increase in brilliance by up to 10 orders of magnitude is achieved by the principle of Self-Amplified Spontaneous Emission (SASE). An overview of the peak brilliance of the different generations is given in Fig. 1.1.

There are two types of free electron lasers. The low-gain FEL uses an optical resonator to amplify the radi-

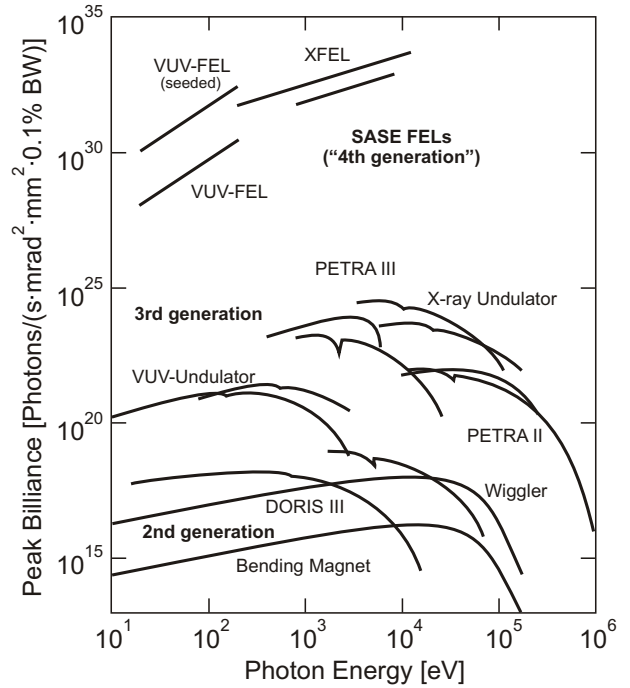


Figure 1.1: Peak brilliance of various synchrotron radiation sources compared with the SASE FELs.

ation. The light is reflected with mirrors, so that each electron bunch interacts with the light pulse, generated by the previous electron bunch, and produces photons with the same wavelength. This principle works only for wavelengths larger than 150 nm because of the poor reflectivity of mirrors below 150 nm. For the shorter wavelengths of vacuum ultra-violet (VUV) and X-ray radiation, the amplification and saturation have to take place within a single pass of the electron bunch through the undulator.

In the undulator, the electrons start to emit photons spontaneously with random phase. The radiation with the wavelength

$$\lambda_{\text{ph}} = \frac{\lambda_{\text{u}}}{2\gamma_{\text{rel}}^2} \left(1 + \frac{K^2}{2} \right) \quad \text{with} \quad K = \frac{eB_{\text{u}}\lambda_{\text{u}}}{2\pi m_e c} \quad (1.1)$$

fulfills the resonance condition of the undulator. Here λ_{u} is the period length of the undulator, $\gamma_{\text{rel}} = E/m_e c^2$, E the energy of the electron, m_e the rest mass of the electron, e the elementary charge, c the velocity of light in the vacuum and B_{u} the peak magnetic field in the undulator. The wavelength of the photons can be tuned by changing the energy of the electrons. The electrons interact with the electric field of the light and rearrange themselves in a longitudinal charge-density modulation called micro-bunching, which enhances the power and coherence of radiation. [And00] This process is called Self-Amplified-Spontaneous-Emission (SASE) and produces laser quality light.

In the case of a mono-energetic electron beam with an energy that fulfills the resonance condition, the energy-gain $G = E_{\text{final}}/E_{\text{initial}}$ of the radiation along the undulator as

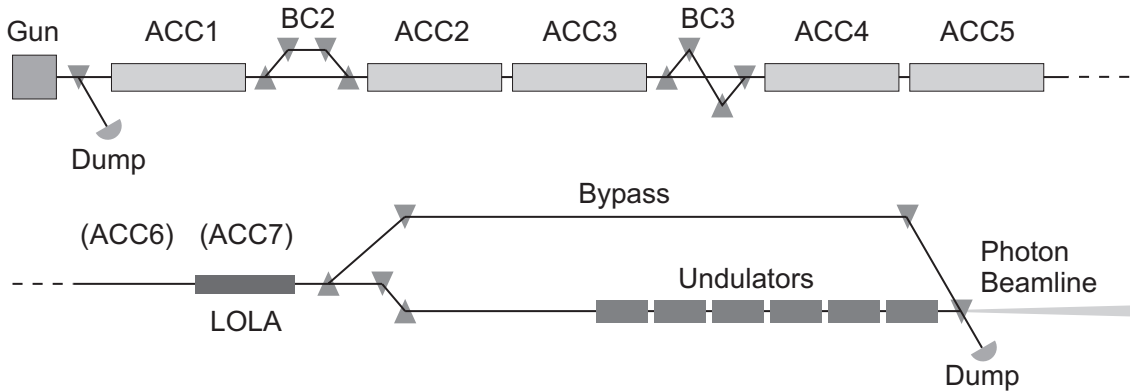


Figure 1.2: Layout of the 260 m long VUV-FEL. The electron bunches are produced in the RF photocathode gun. The five acceleration modules ACC1-ACC5 are able to increase the beam energy up to 800 MeV. Another enhancement up to 1 GeV can be achieved by introducing two additional modules ACC6 and ACC7. The bunches are compressed in the two magnetic chicanes BC2 and BC3 by a total factor of 40. Before the beam is led through the undulator section, or alternatively through the bypass, it can be analyzed by the transverse deflecting cavity LOLA.

a function of the longitudinal position z is given by

$$G(z) \sim \exp\left(\frac{z}{L_G}\right), \quad (1.2)$$

where L_G is the gain-length that is proportional to

$$L_G \sim \left(\frac{\sigma_t^2}{I_0}\right)^{\frac{1}{3}}. \quad (1.3)$$

Here σ_t is the transverse rms beam size and I_0 is the peak current. High gain of the radiation can only be achieved if the gain-length is smaller than the undulator length and the peak current has to be high enough. To generate radiation with a wavelength of 6 nm at the VUV-FEL, a peak current of about 2500 A is required [TFR02]. At low energies the space charge forces due to this high charge-density would cause the beam size to increase so dramatically, that it would be useless for the FEL process. Conventional diagnostic tools like streak cameras cannot presently measure bunch lengths of less than 200 fs. The best resolution presently available for longitudinal bunch-length measurements is provided by LOLA, with a minimum resolution of about 17 fs.

1.2 The VUV-FEL

The work on the TESLA Test Facility (TTF) started in 1992. As the name implies, the new device was intended to perform various tests for the TeV-Energy Super-conducting Linear Accelerator (TESLA) [Bri01]. The 100 m long linac of the TTF1 accelerated electron bunches using very high field-gradients in super-conducting cavities. Until the end of 2002 the free electron laser produced SASE radiation with wavelengths between 180-80 nm. Materials scientists and solid state physicists performed the first experiments with this radiation. They scattered photons with wavelengths of about 80 nm off of clusters of inert gas atoms to investigate multiple ionizations [Wab02].

Then the linac has been extended and since the beginning of 2004 the 260 m long VUV-FEL has been in use. In the final setup electron energies up to 1 GeV will be achievable, which will result in wavelength down to 6 nm of the fundamental mode of the FEL (see Eq. (1.1)). In January 2005, the first SASE radiation with 30 nm was produced.

Since June 2005 the VUV-FEL has operated part-time as a user facility.

The schematic of the VUV-FEL is shown in Fig. 1.2. The radio frequency (RF) photocathode gun generates electron bunches with a charge of up to 4 nC. The nominal charge is 1 nC. The gun produces bunch trains with a length of up to 800 μ s and a repetition rate between 1-10 Hz. The bunches within a train are currently separated by 1 μ s. Behind the gun the electrons have an energy of 4.7 MeV. The bunch length amounts to 1.7 mm [Sch04]. This is large with respect to the wavelength of the RF. Especially at small, non-relativistic energies, the space-charge of the electrons cause an expansion of the emittance. To minimize these space-charge effects, bunches with smaller charge-density are produced and compressed longitudinally at ultra-relativistic energies.

The 1.3 GHz RF in ACC1, the first of five super-conducting niobium acceleration modules, boosts the energy up to 126 MeV. The bunch compressor BC2¹ reduces the bunch length by a factor of eight. After acceleration in ACC2 and ACC3 up to 380 GeV, the bunch is compressed in BC3 by a factor of five [Stu04]. The last two modules ACC4 and ACC5 increase the beam energy up to 450 MeV. The necessary space for two additional modules ACC6 and ACC7 is reserved for a later upgrade. Within this region, the transverse deflecting cavity LOLA is installed to investigate the longitudinal bunch shape. After the SASE laser-light is generated in the six 4.5 m long undulators, it is directed into five photon beam-lines leading to the experimental stations. The electron beam is deflected by a dipole magnet and is absorbed in the dump. To protect the undulators during accelerator studies, the beam can also be led to the dump through the bypass.

In February 2003 the German Federal Ministry of Education and Research approved the European X-ray FEL (XFEL). The commissioning of the 3 km long accelerator will start in 2012. The wavelength of the radiation will amount to 6-0.085 nm according to beam energies of 10-20 GeV (see Eq. (1.1)). Supplying 10 experimental stations at 5 beam-lines, the XFEL will produce leading-edge research at DESY. [XFEL]

¹ Due to historical reasons, the naming of the bunch compressors starts with two.

2 Theory

2.1 Linear beam dynamics

In this section, the formalism to describe the motion of the beam within the accelerator beam-line is introduced. Furthermore, important properties of the beam, like emittance, will be defined.

2.1.1 The transfer-matrix formalism

In accelerator physics, it is convenient to divide the particle motion into a design orbit and a small-amplitude oscillation with respect to this reference trajectory. One defines the coordinates of the particles with respect to the coordinate-system that travels along the reference trajectory through the accelerator (see Fig. 2.1). Instead of the time coordinate, one uses the spatial coordinate s , measured with respect to an initial reference point, to define the position within the accelerator. The motion of a particle can be described using the canonical phase-space coordinates (x, p_x, y, p_y, s, p_s) , where x and y denote the horizontal and vertical displacement from the design orbit and s is the coordinate along the reference orbit. The corresponding canonical momentum components are p_x , p_y and p_s . It is common in accelerator physics to use the “geometrical” coordinates as defined below instead of the canonical ones. The geometrical phase-space coordinates describing the motion of the particles are

$$\begin{pmatrix} x(s) \\ x'(s) \\ y(s) \\ y'(s) \\ l(s) \\ \delta(s) \end{pmatrix}, \quad (2.1)$$

where x , y , and l are the horizontal, vertical, and longitudinal distance to the reference particle, $x' = \frac{dx}{ds}$ and $y' = \frac{dy}{ds}$ are the derivatives with respect to the reference coordinate, and $\delta = \frac{p-p_0}{p_0}$ is the relative momentum deviation from the momentum p_0 of the reference particle. In case of a constant longitudinal momentum p_s , also these coordinates are canonical conjugated.

If the beam-line consists only of drift-spaces, dipole, and quadrupole magnets, the equations of motion for the transverse position-offsets become

$$\begin{aligned} x''(s) + K_x(s)x(s) &= \frac{1}{\rho_x(s)}\delta \\ y''(s) + K_y(s)y(s) &= \frac{1}{\rho_y(s)}\delta, \end{aligned} \quad (2.2)$$

where $\rho_x(s)$, $\rho_y(s)$ are the bending radii of the reference trajectory. Furthermore applies

$$\begin{aligned} K_x(s) &= \frac{1}{\rho_x^2(s)} - k(s) \\ K_y(s) &= \frac{1}{\rho_y^2(s)} + k(s) \end{aligned} \quad (2.3)$$

with

$$k(s) = \frac{q}{p}g(s), \quad (2.4)$$

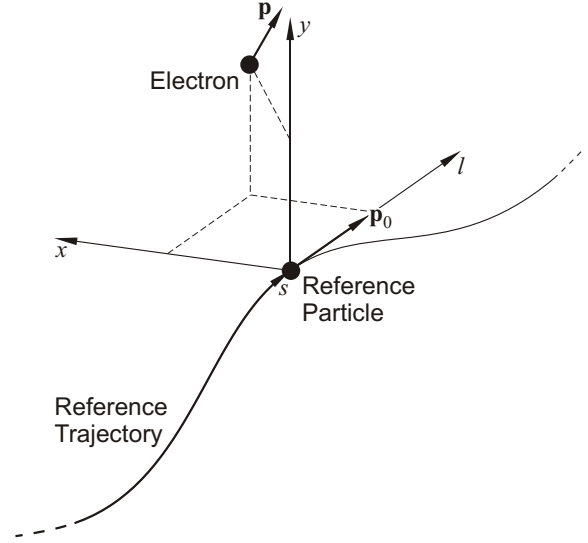


Figure 2.1: Definition of the coordinate-system. The reference particle is located at the position s . The phase-space coordinates of the electrons of the bunch refer to the coordinate-system of this reference particle.

where q is the charge and p the momentum of the particle, and $g(s)$ is the gradient of the magnetic field at the position s . K_x and K_y are called the focussing functions.

Using a matrix formalism the solution of Eq. (2.2) can be expressed as

$$\begin{aligned} \mathbf{x}(s) &= \mathbf{R}_x(s, s_0) \cdot \mathbf{x}(s_0) \quad \text{with } \mathbf{x}(s) = \begin{pmatrix} x(s) \\ x'(s) \end{pmatrix} \\ \mathbf{y}(s) &= \mathbf{R}_y(s, s_0) \cdot \mathbf{y}(s_0) \quad \text{with } \mathbf{y}(s) = \begin{pmatrix} y(s) \\ y'(s) \end{pmatrix}. \end{aligned} \quad (2.5)$$

\mathbf{R}_x and \mathbf{R}_y are the transfer-matrices for the horizontal and the vertical plane, respectively. The general transfer-matrix \mathbf{R} for a constant focussing function K (hard-edge model) is [Lee99]

$$\mathbf{R} = \begin{cases} \begin{pmatrix} \cos(\sqrt{K}d) & \frac{1}{\sqrt{K}}\sin(\sqrt{K}d) \\ -\sqrt{K}\sin(\sqrt{K}d) & \cos(\sqrt{K}d) \end{pmatrix} & \text{for } K > 0 \\ \begin{pmatrix} \cosh(\sqrt{|K|}d) & \frac{1}{\sqrt{|K|}}\sinh(\sqrt{|K|}d) \\ \sqrt{|K|}\sinh(\sqrt{|K|}d) & \cosh(\sqrt{|K|}d) \end{pmatrix} & \text{for } K < 0, \end{cases} \quad (2.6)$$

where $d = s - s_0$.

In a quadrupole where $\frac{1}{\rho} = 0$ there is $K_x = -K_y$. This means that a horizontally focussing quadrupole is de-focussing vertically, and vice-versa. To achieve a focussing in both transverse directions, combinations of quadrupoles are used. Common setups are FODO, where the quadrupoles are spaced equally with alternating field, and doublets, where two quadrupoles with opposite field are put closely together to yield focussing in both planes.

In the thin-lens approximation, with $d \rightarrow 0$, the transfer-matrix for a quadrupole reduces to [Lee99]

$$\mathbf{R}_{\text{quad}} = \begin{pmatrix} 1 & 0 \\ -1/f & 1 \end{pmatrix}, \quad (2.7)$$

with the focal length f given by

$$f = \lim_{d \rightarrow 0} \frac{1}{Kd} \quad \text{with} \quad Kd = \text{const}. \quad (2.8)$$

The focal length is positive for a focussing quadrupole and negative for a de-focussing one.

The gradient of the magnetic field vanishes ($g=0$) within a dipole magnet. So, for the corresponding bending direction with the orbiting-angle $\theta = d/\rho$, the transfer-matrix will be

$$\mathbf{R}_{\text{dipole}} = \begin{pmatrix} \cos \theta & \rho \sin \theta \\ -\frac{1}{\rho} \sin \theta & \cos \theta \end{pmatrix}. \quad (2.9)$$

Here Eq. (2.3), Eq. (2.4) and Eq. (2.6) were used.

Within a drift-space, we have no magnetic field. Therefore, the gradient is zero and the bending radius goes to infinity. The resulting transfer-matrix is

$$\mathbf{R}_{\text{drift}} = \begin{pmatrix} 1 & d \\ 0 & 1 \end{pmatrix}. \quad (2.10)$$

Including the longitudinal phase-space consisting of the longitudinal displacement l and the relative momentum deviation δ , the matrix formalism expands to

$$\begin{pmatrix} x \\ x' \\ y \\ y' \\ l \\ \delta \end{pmatrix} = \begin{pmatrix} R_{11} & R_{12} & 0 & 0 & 0 & R_{16} \\ R_{21} & R_{22} & 0 & 0 & 0 & R_{26} \\ 0 & 0 & R_{33} & R_{34} & 0 & R_{36} \\ 0 & 0 & R_{43} & R_{44} & 0 & R_{46} \\ R_{51} & R_{52} & R_{53} & R_{54} & R_{55} & R_{56} \\ 0 & 0 & 0 & 0 & 0 & 1 \end{pmatrix} \cdot \begin{pmatrix} x_0 \\ x'_0 \\ y_0 \\ y'_0 \\ l_0 \\ \delta_0 \end{pmatrix}, \quad (2.11)$$

where the index 0 denotes that the quantity is given at the position s_0 . The matrix elements R_{13} , R_{14} , R_{23} , R_{24} , R_{31} , R_{32} , R_{41} and R_{42} are zero if there is no additional coupling between the transverse directions. The zeros in column five result from the independence of the transverse coordinates from the longitudinal displacement l . We use purely-static magnetic-fields. Therefore, the energy stays constant, as implied by the zeros and the one of row six. [Bro82] The elements R_{16} and R_{36} are called the dispersion

$$\begin{aligned} R_{16} &= D_x = \frac{\Delta x}{\Delta p/p_0} \\ R_{36} &= D_y = \frac{\Delta y}{\Delta p/p_0}, \end{aligned} \quad (2.12)$$

generated by the element described by \mathbf{R} . The matrix elements R_{26} and R_{46} describe the generated angular dispersions. The transfer-matrices given by Eq. (2.6) can be identified with the sub-matrices consisting of R_{11} , R_{12} , R_{21} , R_{22} and R_{33} , R_{34} , R_{43} , R_{44} .

The longitudinal displacement l after passing the magnet, depends on the transverse position-offset of the particle, but these contributions are usually negligible. In the case of fields which are constant in time, $R_{55} = 1$. Therefore, a change of the longitudinal displacement is only caused by the momentum deviation δ and the longitudinal dispersion R_{56} . In bunch compressors this quantity is very important (see Sec. 2.2).

The beam-line consists of many elements with a piecewise constant focussing function K . To calculate the phase-space coordinates from the start to the end of the linac, one has to multiply the corresponding transfer-matrices.

2.1.2 The Twiss-Parameters

The equation of transverse motion in an accelerator is given by Eq. (2.2). For particles with vanishing relative momentum deviation $\delta = 0$ and using the variable h instead of x or y it simplifies to

$$h''(s) + K_h(s)h(s) = 0. \quad (2.13)$$

The general solution of Eq. (2.2) becomes

$$h(s) = a\sqrt{\beta_h(s)} \cos(\psi_h(s) + \xi_h), \quad (2.14)$$

with the phase

$$\psi_h(s) = \int_0^s \frac{ds}{\beta_h(s)}. \quad (2.15)$$

a and ξ_h are constants to be determined from initial conditions. Eq. (2.14) denotes a pseudo-harmonic oscillation with a varying amplitude $\sqrt{\beta_h(s)}$. This transverse motion of the particles is called betatron-motion, $\beta_h(s)$ is the beta function. [Lee99]

With Eq. (2.14) and its derivative, the Courant-Snyder invariant a^2 is defined as

$$a^2 = \gamma_h(s)h^2(s) + 2\alpha_h(s)h(s)h'(s) + \beta_h(s)h'^2(s), \quad (2.16)$$

with

$$\gamma_h(s) = \frac{(1 + \frac{1}{4}\beta_h'^2(s))}{\beta_h(s)} \quad \text{and} \quad \alpha_h(s) = -\frac{1}{2}\beta_h'(s). \quad (2.17)$$

$\beta_h(s)$, $\alpha_h(s)$ and $\gamma_h(s)$ are called the Twiss parameters, especially $\beta_h(s)$ is the beta function. Eq. (2.16) is an equation of an ellipse, called the phase-space ellipse. In Fig. 2.2 the correlation between this ellipse and the Twiss parameters is illustrated. The Twiss-parameters and the phase-space ellipse are originally defined for circular accelerators and storage rings, where each particle travels on its own phase-space ellipse. This formalism is transferred to linear accelerators. For a detailed treatment see [RS93].

The Twiss-parameters are dependent on the spatial coordinate s , indicating that the shape of the ellipse changes along the accelerator. According to Liouville's theorem, the phase-space area given by $A = \pi a^2$ stays constant under the influence of conservative forces. In [RS93] the constance of the phase-space area is verified.

If the particle with the initial Twiss parameters ($\beta_h(s_0)$, $\alpha_h(s_0)$, $\gamma_h(s_0)$) and the Courant-Snyder invariant a^2 travels along the accelerator, the Twiss parameters at any position s can be calculated by

$$\begin{pmatrix} \beta_h(s) \\ \alpha_h(s) \\ \gamma_h(s) \end{pmatrix} = \begin{pmatrix} R_{11}^2 & -2R_{11}R_{12} & R_{12}^2 \\ -R_{21}R_{11} & 1+2R_{12}R_{21} & -R_{12}R_{22} \\ R_{21}^2 & -2R_{21}R_{22} & R_{22}^2 \end{pmatrix} \cdot \begin{pmatrix} \beta_h(s_0) \\ \alpha_h(s_0) \\ \gamma_h(s_0) \end{pmatrix}. \quad (2.18)$$

This equation results by equating Eq. (2.16) for the initial and final conditions, substituting $h(s_0)$ and $h'(s_0)$ with Eq. (2.5) and using $|\mathbf{R}| = 1$. The resulting matrix is called the Twiss matrix because it transforms the Twiss parameters through the entire beam-line.

2.1.3 The emittance

One of the most important issues in any accelerator is to collimate the beam in forward direction. The emittance characterizes, how well this has been done. A small emittance is desired and means a better focus of the momentum

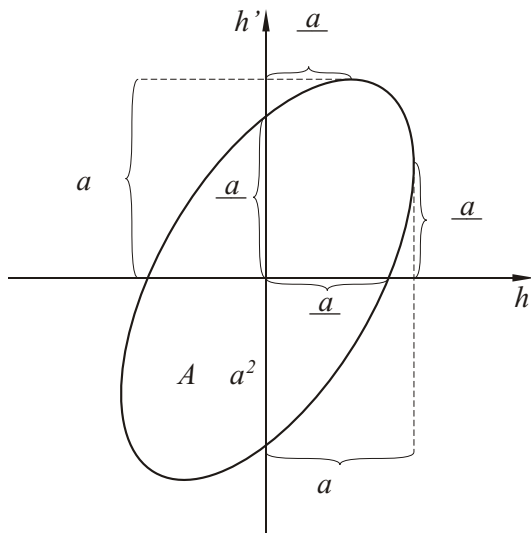


Figure 2.2: The phase-space ellipse. β , α and γ are the Twiss parameters. In case of a distribution of many particles, the ellipse encloses the rms of the particle distribution. The emittance ε is defined as the area A of the ellipse.

in forward direction. Putting it in equations, we approximate a realistic beam distribution function. If we neglect beam losses, diffusion processes and other disturbances which influence the particles in the bunch, each particle has its own Courant-Snyder invariant with invariant area. Assuming a normalized distribution function $\rho(h, h')$ with $\int \rho(h, h') dh dh' = 1$, the moments of the beam distribution are [Lee99]

$$\langle h \rangle = \int h \rho(h, h') dh dh' , \quad \langle h' \rangle = \int h' \rho(h, h') dh dh' , \quad (2.19)$$

$$\sigma_h^2 = \int (h - \langle h \rangle)^2 \rho(h, h') dh dh' , \quad \sigma_{h'}^2 = \int (h' - \langle h' \rangle)^2 \rho(h, h') dh dh' , \quad (2.20)$$

$$\sigma_{hh'} = \int (h - \langle h \rangle)(h' - \langle h' \rangle) \rho(h, h') dh dh' = r \sigma_h \sigma_{h'} , \quad (2.21)$$

where σ_h and $\sigma_{h'}$ are the rms beam-widths and divergence, $\sigma_{hh'}$ the correlation and r the correlation coefficient. The rms beam-emittance is then defined as

$$\varepsilon_{\text{rms}} = \sqrt{\sigma_h^2 \sigma_{h'}^2 - \sigma_{hh'}^2} = \sigma_h \sigma_{h'} \sqrt{1 - r^2} . \quad (2.22)$$

The rms emittance is equal to the area of the phase-space ellipse of the rms of the particle distribution as shown in Fig. 2.2. The rms beam-width $\sigma_{h, \text{rms}}$ and the rms beam-divergence $\sigma_{h', \text{rms}}$ are given by

$$\sigma_{h, \text{rms}} = \sqrt{\beta_h \frac{\varepsilon_h}{\pi}} , \quad \sigma_{h', \text{rms}} = \sqrt{\gamma_h \frac{\varepsilon_h}{\pi}} . \quad (2.23)$$

Within a beam-line composed of only drift-spaces, dipoles, and quadrupoles the emittance is invariant.

The emittance depends on the energy of the beam. In accelerator modules, the longitudinal momentum of the electrons is increased while the transverse momentum remains constant. Thus the angle between the direction of

motion and the design orbit gets smaller. This means that the emittance gets smaller. Because of this, the normalized emittance ε^n is usually defined as

$$\varepsilon^n = \beta \gamma \varepsilon , \quad (2.24)$$

where $\beta = v/c \approx 1$ and γ is the Lorentz factor.

2.2 The bunch compressor

Space charge forces are $\sim 1/\gamma^2$. Therefore, bunch compression has to take place at ultra-relativistic energies in so-called bunch compressors. A bunch compressor consists of several dipole magnets which force the bunch to travel along a chicane. The common types of bunch compressors are the C-chicane and the S-chicane. TTF is equipped with both types. BC2 is of the C-variety and BC3 of the S-type. For a detailed discussion about different variations of these chicanes see [Stu04]. The sketch of a C-chicane in Fig. 2.3 a) illustrates how this principle of bunch compression works. It is based on the energy dependence of the deflection of a charged particle by a magnetic field. Electrons with a higher energy ($\delta > 0$) are less strongly deflected by a magnetic field than the ones with lower energy and, therefore, have a shorter path length in a C-chicane. If a bunch has an energy distribution such that the trailing electrons have a higher energy than the leading ones, the particles will converge longitudinally and produce a higher charge-density.

Using the initial phase-space coordinates $(x_i, x'_i, y_i, y'_i, l_i, \delta_i)$ in front of the bunch compressor, one can calculate the phase-space coordinates after passing the chicane, via the transfer-matrix formalism given by Eq. (2.11). The final longitudinal position l_f of an electron within the bunch can be calculated to the first order from the initial position l_i and the initial, relative energy-deviation δ_i ¹ by

$$l_f \approx l_i + R_{56} \delta_i . \quad (2.25)$$

Here the contributions $R_{51}x_i$, $R_{52}x'_i$, $R_{53}y_i$ and $R_{54}y'_i$ are neglected [Stu04]. Because a particle with a higher energy than the reference particle ($\delta > 0$) moves forward with respect to the reference particle, the longitudinal dispersion R_{56} will be positive.

The initial, longitudinal, phase-space ellipse, as shown in Fig. 2.3 b), has a tilt, called the linear energy correlation $u = \frac{dE}{dl}$. Additionally, the energy of each electron deviates from this slope by $\varepsilon_{i,n}$, where n denotes the n -th electron. The rms is called the uncorrelated energy spread

$$\sigma_{\varepsilon, i} = \sqrt{\frac{1}{N} \sum_n \varepsilon_{i,n}^2} , \quad (2.26)$$

where N is the total number of particles. The total energy deviation of an electron with respect to the reference particle is then

$$\delta_n = \frac{u l_{i,n} + \varepsilon_{i,n}}{E_0} . \quad (2.27)$$

If we substitute Eq. (2.27) into Eq. (2.25), the longitudinal displacement of an ultra-relativistic particle after passing the bunch compressor will be

$$l_f \approx \left(1 + \frac{R_{56}u}{E_0}\right) l_i + \left(\frac{R_{56}}{E_0}\right) \varepsilon_i . \quad (2.28)$$

¹ For ultra-relativistic particles, $E \approx pc$. Therefore, the relative momentum-deviation δ also gives the relative energy-deviation $\delta = \frac{p-p_0}{p_0} \approx \frac{E-E_0}{E_0}$.

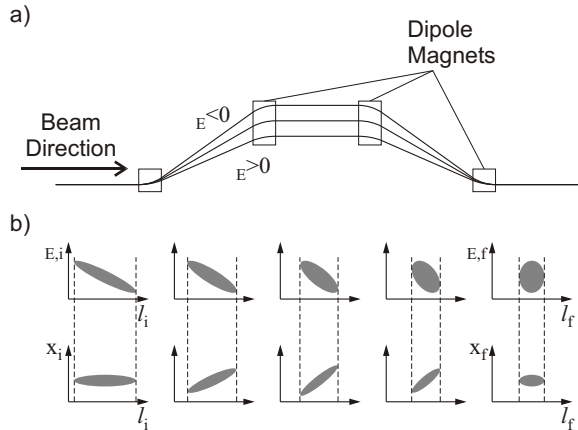


Figure 2.3: The principle of bunch compression using a magnetic C-chicane. a) Electrons with different energy deviations δ with respect to the reference particle have different path-lengths through the magnetic chicane. b) The longitudinal phase-space is sheared within the different sections of the bunch compressor. The final bunch length is limited by the uncorrelated energy spread. The different path-lengths manifest in different horizontal position-offsets x . The trailing, higher-energy electrons, therefore, catch up with the leading ones. Here the maximum compression is shown.

Assuming an initial rms bunch length $\sigma_{l,i} = \sqrt{\frac{1}{N} \sum_n l_{i,n}^2}$ at the moment of entry into the bunch compressor, the final rms bunch length can be calculated by

$$\sigma_{l,f} = \sqrt{\left(\frac{dl_f}{dl_i}\right)^2 \sigma_{l,i}^2 + \left(\frac{dl_f}{d\epsilon_i}\right)^2 \sigma_{\epsilon,i}^2}, \quad (2.29)$$

and finally [Stu04]

$$\sigma_{l,f} = \sqrt{\left(1 + \frac{R_{56}u}{E_0}\right)^2 \sigma_{l,i}^2 + \left(\frac{R_{56}}{E_0}\right)^2 \sigma_{\epsilon,i}^2}. \quad (2.30)$$

This equation shows that the shortness of the final bunch is limited by the uncorrelated energy spread, when $u = -E_0/R_{56}$.

Fig. 2.3 b) shows how the uncorrelated energy spread limits the final bunch length. While the bunch travels through the chicane, the longitudinal phase-space is sheared and the uncorrelated energy spread increases. The phase space area stays constant, according to Liouville's theorem. In the rightmost diagrams the bunch is fully compressed.

The upper calculations are restricted to the first-order. For large energy chirp and long bunches also second order effects have to be considered. The higher order effects are twofold: The nonlinearity of the displacement and the curvature of the RF acceleration. The energy dependent longitudinal displacement can up to second order be written as

$$l_f = l_i + R_{56}\delta + T_{566}\delta^2 + \dots \quad (2.31)$$

The second order matrix element can be estimated as $T_{566} \approx -\frac{3}{2}R_{56}$ [Stu04]. Therefore, the second-order term always decreases the longitudinal displacement.

The RF used to accelerate the electron bunch causes a quadratic curvature in the longitudinal phase-space distribution. The reason is the sinusoidal time dependence of

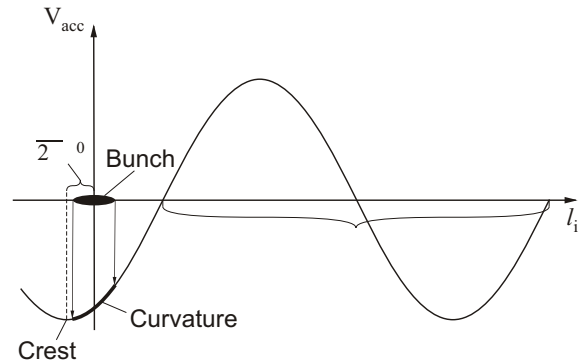


Figure 2.4: The principle of longitudinal phase-space shaping. Because of the sinusoidal time dependence of the accelerating RF wave, the electrons undergo an acceleration depending on the longitudinal displacement l_i within the bunch. The leading particles experience a lower voltage V_{acc} than the trailing ones and gain, therefore, less energy. The resulting energy chirp depends on the phase offset ϕ_0 with respect to the crest. Because the bunch length is much smaller than the wavelength λ of the RF wave, the curvature can be expanded into a polynomial of the second order. Note that the accelerating voltage has to be negative for electrons. This sketch is not drawn to scale.

the RF electric field. The energy E_f of an electron after undergoing the acceleration will be

$$E_f = E_{0,i} + \Delta E_i + e|V_{acc}| \cos\left(\frac{2\pi l_i}{\lambda} + \phi_0\right), \quad (2.32)$$

where $\Delta E_i = E_i - E_{0,i}$ is the initial energy deviation with respect to the initial energy $E_{0,i}$ of the reference particle, e is the elementary charge, V_{acc} the accelerating voltage, λ the wavelength of the RF and ϕ_0 the phase offset with respect to on-crest. ϕ_0 is also called the off-crest phase and is defined with respect to the bunch center. To achieve the desired energy chirp, the off-crest phase has to be negative. With decreasing ϕ_0 , the energy correlation decreases ($u < 0$), so that the compression, obtained in the bunch compressor, increases. A maximum compression is achieved at $\phi_0 \approx -13$ deg. If we would decrease the phase further the bunch will be over-compressed and the bunch length increases again.

The accelerating modules work with a frequency of 1.3 GHz. This corresponds to a wavelength of $\lambda = 231$ mm. The total bunch length in front of BC2 is measured at $\sigma_{Gunn} = 1.7$ mm [Sch04], thus $\sigma_{Gunn} \ll \lambda$. Therefore, we can expand Eq. (2.32) to the second order around $l_i = 0$ and get

$$E_f \approx E_{0,i} + \Delta E_i + e|V_{acc}| \left(\cos\phi_0 - \frac{2\pi}{\lambda} l_i \sin\phi_0 - \frac{2\pi^2}{\lambda^2} l_i^2 \cos\phi_0 \right). \quad (2.33)$$

With the final energy $E_{0,f}$ of the reference particle

$$E_{0,f} = E_{0,i} + e|V_{acc}| \cos\phi_0 \quad (2.34)$$

the relative energy deviation after the acceleration, in front

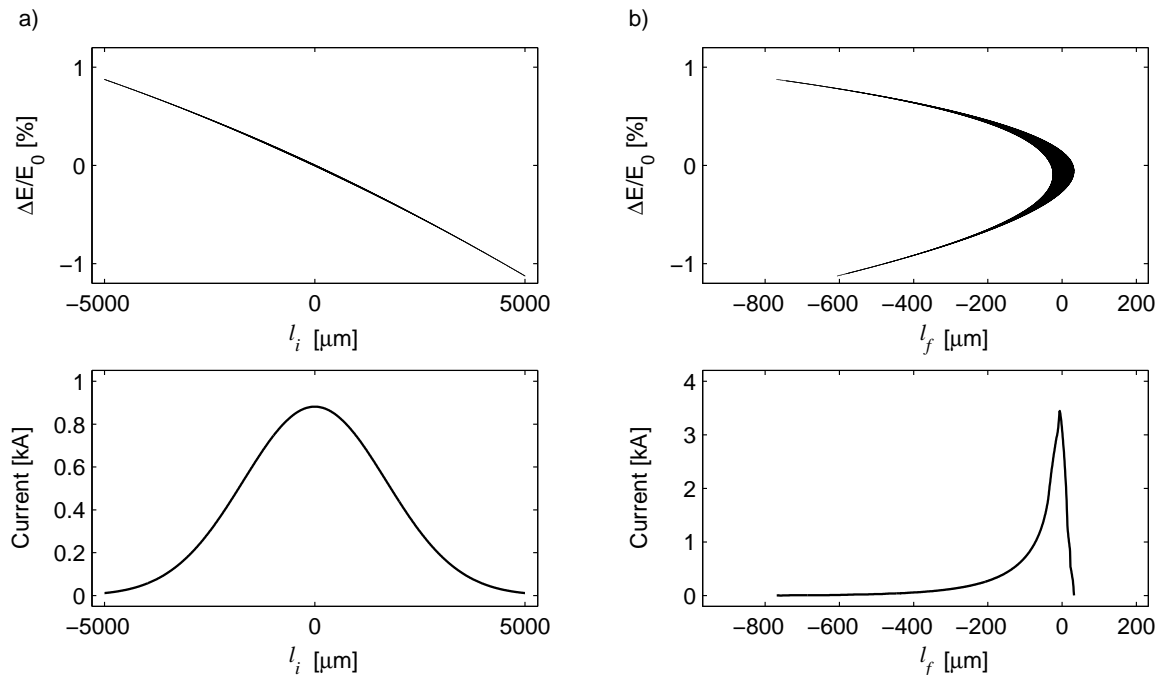


Figure 2.5: A simulation of the influence of bunch compressors. The figure shows the longitudinal phase-space distribution (upper plots) and the charge-density ρ (lower plots) before a) and after b) passing the bunch compressor. The phase-space distribution of about 110 000 electrons exhibits a tilt (chirp) and a small quadratic curvature. The longitudinal charge-distribution is Gaussian as well as the uncorrelated energy-spread within each slice of the bunch. Within the magnetic chicane, the phase-space folds over and forms a spike with a high charge-density in the head of the bunch. At TTF, the bunch is influenced by two bunch compressors. The resulting charge distribution is much more complicated than shown here.

of the bunch compressor will be

$$\begin{aligned} \delta &= \frac{\Delta E_f}{E_{0,f}} \\ &= \frac{1}{E_{0,f}} \left(E_{0,i} \delta_i - l_i e |V_{\text{acc}}| \frac{2\pi}{\lambda} \sin \phi_0 - l_i^2 e |V_{\text{acc}}| \frac{2\pi^2}{2\lambda^2} \cos \phi_0 \right) \end{aligned} \quad (2.35)$$

$$= A\delta_i + Bl_i + Cl_i^2 . \quad (2.36)$$

Here the quadratic displacement dependence of the energy is visible. This final energy deviation enters the bunch compressor as the initial energy deviation. We insert Eq. (2.36) into Eq. (2.31) and get with the estimations $\left| \frac{T_{566}}{R_{56}} \right| \approx \mathcal{O}(1)$ and $A\delta_i \ll 1$ [Stu04]

$$l_f \approx R_{56} A\delta_i + (1 + BR_{56}) l_i + (CR_{56} + B^2 T_{566}) l_i^2 . \quad (2.37)$$

Higher order terms are neglected. Because R_{56} and T_{566} have different signs the second order term does only vanish if $C > 0$. This is equivalent with an accelerating phase of $|\phi_0| > \frac{\pi}{2}$. In this range of ϕ_0 the cavity field would be decelerating, which is obviously excluded. To overcome this problem a third harmonic cavity will be installed [Flo01]. The frequency will be 3.9 GHz. With such a device, it will be possible to compensate the quadratic curvature of the longitudinal phase-space. The residual curvature then is of the third order. With this, the longitudinal phase-space distribution will become approximately linear over a wider range, so that a smoother compression can be achieved.

In Fig. 2.5, the results of a simulation are given in which a folding of the longitudinal phase-space is evident. The

initial phase-space distribution, as shown in part a), consists of several slices. They are not visible, because of the large number of 110 000 particles. The number of particles along the bunch varies according to a Gaussian distribution. Therefore, the charge-density ρ is also a Gaussian distribution, as shown in the lower plot of Fig. 2.5 a). The particles within a slice are distributed around the respective mean energy in a Gaussian distribution. This represents the uncorrelated energy spread. The whole charge-distribution is impressed with an energy modulation according to Eq. (2.36).

The longitudinal displacements of the particles after passing the bunch compressor are calculated using Eq. (2.31) and plotted in Fig. 2.5 b). The phase-space distribution folds over, with a large amount of particles contained in a narrow spike at the head of the bunch. Therefore, the charge-density is very high there.

2.2.1 An estimation of the bunch length

The electron bunch leaves the gun with an energy of $E_1 = 4.7$ MeV and a rms bunch length of $\sigma_{\text{Gun}} = 1.7$ mm [Sch04]. The particles within the bunch exhibit a random energy deviation called the uncorrelated energy spread. Measurements at the TTF showed an resolution-limited, uncorrelated, energy spread of $\sigma_{\epsilon, \text{high}} = 25$ keV, while simulations suggest that the spread is about 5 keV. Earlier measurements with a different gun yielded the predicted $\sigma_{\epsilon, \text{low}} = 5$ keV [Hue03]. After the bunch has passed the first accelerating module ACC1, its mean energy is $E_2 = 126$ MeV. In the first bunch compressor (BC2), the bunch experiences a matrix element of $R_{56,2} = 180$ mm.

The following modules (ACC2/3) accelerate the beam to an energy of $E_3 = 380$ MeV. In the normal case, the bunch enters these modules on-crest, so that the additional modulation of the energy is negligible. The second bunch compressor (BC3), which is an S-chicane, has an $R_{56,3} = 50$ mm [Stu04].

With these parameters, we are able to give an estimation of the bunch length. We consider two cases: First, we use only the BC2 and set the off-crest phase ϕ_0 , so that the longitudinal phase-space distribution folds over in BC2 at the initial longitudinal displacement of $l_i = 0$. Second, we use both bunch compressors. The phase-space distribution folds over in BC3 at $l_i = 0$. We will calculate the off-crest phases in ACC1 and the bunch lengths for both the high and the low value of the uncorrelated energy spread.

For the case of only one bunch compressor, we can use Eq. (2.30). At the position of the folding, the first term vanishes and the bunch length will be

$$\sigma_{f,high} = \frac{R_{56,2}}{E_2} \sigma_{\epsilon,high} = 119 \text{ fs} \quad (2.38)$$

$$\sigma_{f,low} = \frac{R_{56,2}}{E_2} \sigma_{\epsilon,low} = 24 \text{ fs} . \quad (2.39)$$

By setting the first term of Eq. (2.30) to zero, we obtain a condition for the energy correlation

$$u = -\frac{E_2}{R_{56,2}} . \quad (2.40)$$

Additionally, u can be calculated by deriving the energy given in Eq. (2.32) by the longitudinal displacement l_i of the particles and will be at the position $l_i = 0$

$$u = -\frac{2\pi}{\lambda} (E_2 - E_1) \sin \phi_0 . \quad (2.41)$$

By equating the last two equations, we obtain the off-crest phase

$$\phi_0 = \arcsin \left(\frac{\lambda}{2\pi} \frac{1}{E_2 - E_1} \frac{E_2}{R_{56,2}} \right) = 12.2 \text{ deg} . \quad (2.42)$$

In case of a folding of the phase-space distribution in the second bunch compressor, we first have to calculate the effective R_{56} , using Eq. (2.25). After passing BC2 the displacement l_2 of the particle with the initial displacement l_i will be

$$l_2 = l_i + R_{56,2} \frac{\Delta E}{E_2} , \quad (2.43)$$

where ΔE is the difference of the energy of the particle and the energy of the reference particle. Each particle gains approximately the same amount of energy in the acceleration modules ACC2 and ACC3. Therefore, ΔE stays constant and after passing BC3 the considered particle will have a longitudinal displacement l_3 of

$$l_3 = l_2 + R_{56,3} \frac{\Delta E}{E_3} . \quad (2.44)$$

Inserting Eq. (2.43) into Eq. (2.44) will lead to

$$l_3 = l_i + \left(R_{56,2} + R_{56,3} \frac{E_2}{E_3} \right) \frac{\Delta E}{E_2} . \quad (2.45)$$

With the definition of the expression in the brackets as the effective matrix element

$$R_{56,eff} := \left(R_{56,2} + R_{56,3} \frac{E_2}{E_3} \right) = 197 \text{ mm} , \quad (2.46)$$

we will get

$$l_3 = l_i + R_{56,eff} \frac{\Delta E}{E_2} . \quad (2.47)$$

This equation has the same shape as Eq. (2.25). Therefore, the bunch length can be calculated using Eq. (2.30), where the first term vanishes again. This results for the two values of the uncorrelated energy spread in

$$\sigma_{f3,high} = \frac{R_{56,eff}}{E_2} \sigma_{\epsilon,high} = 130 \text{ fs} \quad (2.48)$$

$$\sigma_{f3,low} = \frac{R_{56,eff}}{E_2} \sigma_{\epsilon,low} = 26 \text{ fs} . \quad (2.49)$$

Now we will calculate the off-crest phase ϕ_0 in ACC1, for the case of the folding of the phase-space distribution in BC3. We start with Eq. (2.27)

$$\delta = \frac{u_i l_i + \epsilon_i}{E_2} = \frac{\Delta E}{E_2} , \quad (2.50)$$

where u_i is the initial energy correlation in front of BC2 and ϵ_i is the energy deviation from the slope of the phase-space distribution given by u_i . It can be approximated by $\epsilon_i \ll u_i l_i$ and $\epsilon_2 \ll u_2 l_2$, where u_2 and ϵ_2 are the correlated and the uncorrelated energy deviation, respectively, after passing BC2. With the constance of ΔE after passing ACC1, this will lead to

$$\Delta E \approx u_i l_i \approx u_2 l_2 . \quad (2.51)$$

By inserting Eq. (2.43) into Eq. (2.51), we will get

$$u_i l_i = u_2 l_i + u_2 \frac{R_{56,2}}{E_2} \cdot u_i l_i . \quad (2.52)$$

We apply Eq. (2.30) to BC3 and obtain by setting the first term to zero

$$u_2 = -\frac{E_3}{R_{56,3}} . \quad (2.53)$$

Substituting this in Eq. (2.52) leads to

$$u_i = -\frac{1}{\frac{R_{56,3}}{E_3} + \frac{R_{56,2}}{E_2}} . \quad (2.54)$$

By equating Eq. (2.41) and Eq. (2.54), the off-crest phase ϕ_0 in ACC1 in case of two bunch compressors will be finally

$$\phi_0 = \arcsin \left(\frac{\lambda}{2\pi} \frac{1}{E_2 - E_1} \frac{1}{\frac{R_{56,3}}{E_3} + \frac{R_{56,2}}{E_2}} \right) = 11.2 \text{ deg} . \quad (2.55)$$

With this value, we can calculate the length of the respective part of the bunch after passing BC2, by inserting Eq. (2.41) into Eq. (2.30) and obtain

$$\sigma_{f23,high} = 493 \text{ fs} \quad (2.56)$$

$$\sigma_{f23,low} = 479 \text{ fs} . \quad (2.57)$$

The spike using two bunch compressors is obviously longer than the bunch compressed with only BC2. The reason is the larger matrix element $R_{56,eff}$. To obtain with $R_{56,eff}$ the same compression as with $R_{56,2}$ a smaller off-crest phase has to be used. This means, that the energy chirp is smaller. Therefore, the same uncorrelated energy deviation has a bigger, relative, influence.

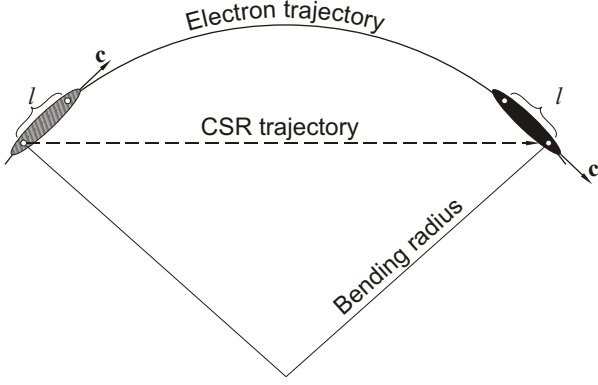


Figure 2.6: Principle of energy transfer due to CSR. The electrons propagate on a curved line. The radiation emitted in the tail of the bunch overtakes electrons in its head with a relative distance of Δl . There the radiation is partly absorbed.

2.2.2 Coherent synchrotron radiation

If a relativistic electron bunch is deflected by a transverse magnetic field, synchrotron radiation is emitted. The radiation is emitted in a wide frequency spectrum. The radiation is coherent in the wavelength range of $\lambda \gg \sigma_l$, with the bunch length σ_l . The total energy loss $\varepsilon_{\text{coh,tot}}$ due to coherent synchrotron radiation (CSR) of the bunch per unit length cdt scales like [Der95]

$$\frac{d\varepsilon_{\text{coh,tot}}}{cdt} \sim \frac{q^2}{\rho^{2/3}\sigma_l^{4/3}}, \quad (2.58)$$

where q is the total charge of the bunch and ρ the bending radius of the trajectory within the magnetic field. The energy loss is strongly enhanced for short bunch lengths and high bunch charge.

The effect of the CSR on the energy distribution inside the bunch is a geometrical effect as illustrated in Fig. 2.6. Since the bunch propagates on a curved trajectory and the emitted radiation travels along a straight line, the path lengths are different. Therefore, the electro-magnetic field emitted at the tail of the bunch, overtakes the leading electrons in a distance Δl with respect to the emitting electron, where l is the longitudinal phase-space coordinate. The interaction of the radiation with the bunch increases the energy spread and the emittance.

The energy loss ε per unit length at a position Δl in the bunch is given by [Sch01]

$$\frac{d\varepsilon}{cdt} = -\frac{qe}{2\pi\epsilon_0 3^{1/3}\rho^{2/3}} \int_{-\infty}^{\Delta l} \frac{1}{(\Delta l - \Delta l')^{1/3}} \frac{\partial\lambda(\Delta l')}{\partial(\Delta l')} d(\Delta l'), \quad (2.59)$$

where e is the elementary charge and ϵ_0 the permittivity in the vacuum. The longitudinal, one-dimensional charge distribution λ is normalized to unity ($\int \lambda(\Delta l)d(\Delta l) = 1$). Fig. 2.7 shows the energy loss for a Gaussian charge distribution with a bunch charge of 1 nC and a bunch length of $\sigma_l = 1$ mm, that propagates on a curve with bending radius of $\rho = 1.5$ m. The leading electrons absorb a fraction of the CSR emitted by the trailing electrons.

Due to the dependence on the derivative of the charge distribution in Eq. (2.59), the effect of CSR is strongly enhanced in charge distributions with large gradients. Therefore, a leading spike of the bunch acquires a large energy

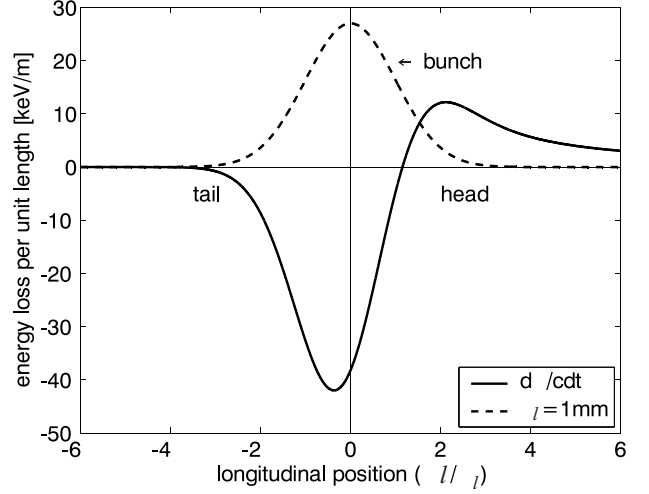


Figure 2.7: Energy loss per unit length along the bunch due to coherent synchrotron radiation. The longitudinal charge distribution (dashed line) has a Gaussian shape. The energy loss (solid line) was calculated using Eq. (2.59). The calculation and the figure originate from [Sch01].

modulation. Because this happens inside the bunch compressor, the dispersion is not fully compensated for this part of the bunch. This results in a transverse displacement of the spike with respect to the rest of the bunch, leading to emittance growth. The strong energy modulation also influences the longitudinal beam dynamics in the subsequent compression stages. A full account of the CSR effects is far beyond the scope of this document.

2.3 The field distribution of the RF of LOLA

A transverse deflecting cavity is well suited for studying the longitudinal bunch structure. The used RF modes have to be dipole modes. Unlike for acceleration modes, both the electric and the magnetic field contribute to the deflection.

The Panofsky-Wenzel theorem, that considers pure TE- or TM-modes, describes the required field properties to deflect ultra-relativistic particles (for reference see [Pan56]). Because of its fundamental importance, its derivation is shown in Sec. A. One might suggest, that a transverse, electric field is sufficient, to deflect a particle transversely. The Panofsky-Wenzel theorem reveals, that this is not the case. The total transverse momentum $\Delta\mathbf{p}_\perp$ of a particle with charge q and velocity v , gained in a cavity with the length L is [Nag04]

$$\Delta\mathbf{p}_\perp^{(2)}(L) = \Re \left\{ \frac{iq}{\omega} \cdot \int_{z=0}^{z=L} \nabla_\perp \mathbf{E}_z(z) \cdot e^{i\omega z/v} dz \right\}, \quad (2.60)$$

where z is the spatial coordinate along the cavity, $\omega = 2\pi f$ with f the frequency of the RF, and $\nabla_\perp \mathbf{E}_z$ the transverse gradient of the longitudinal component of the electric field. The longitudinal component \mathbf{E}_z of the electric field is zero, for a pure TE-mode. If there is a non-vanishing longitudinal component, that is constant over the whole aperture of the cavity, the transverse gradient is zero. In both cases the particle is not deflected. Physically, a pure TE-mode gives zero deflection because the electric and magnetic forces cancel. [Wan98]

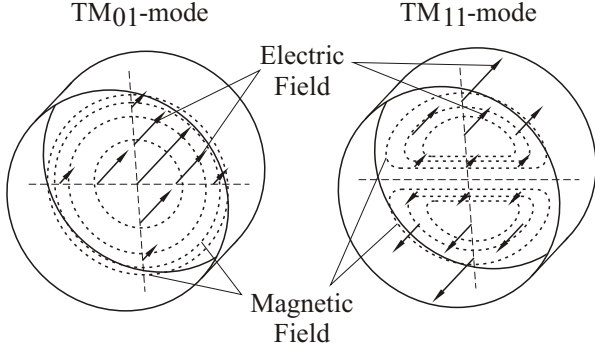


Figure 2.8: Field pattern of the TM₀₁- and the TM₁₁-mode.

Capable modes of a pillbox are the pure TM-modes TM₀₁₀ and TM₁₁₀² (see Fig. 2.8). The first one is only usable for off-axis particles because this mode is axial symmetric with zero transverse gradient of the longitudinal electric field on the axis. The TM₁₁₀-mode has a dipolar characteristic, the longitudinal electric field depends approximately linearly on the radius, yielding a strong and nearly uniform deflection. This was the main reason why the TM₁₁₀-mode was chosen for the RF deflecting cavity LOLA.

The TM₁₁₀-mode non-zero field components in cylindrical coordinates (r, θ, z) are [Wan98]

$$\begin{aligned} E_z &= E_0 J_1(k_D r) \cos \theta \\ B_r &= -i \frac{E_0}{c} \frac{J_1(k_D r)}{k_D r} \sin \theta \\ B_\theta &= -i \frac{E_0}{c} J_1'(k_D r) \cos \theta, \end{aligned} \quad (2.61)$$

where $E_0 = |E_0| \cdot e^{ik_D(z-ct)}$ is the alternating, complex amplitude, c the velocity of light, $k_D = \omega/c$ the deflecting-mode wave number, and J_1 the first order Bessel function of the first kind with its derivative $J_1' = \partial_{(k_D r)} J_1(k_D r) = \frac{1}{2}(J_0(k_D r) - J_2(k_D r))$. $J_0(k_D r)$ and $J_2(k_D r)$ are the zero- and the second-order Bessel function, respectively.

The field distribution within the real cavity with openings for entry and exit of the beam is different from the pure TM₁₁-mode, that can exist only in closed cavities. We assume an iris-loaded structure as an infinite array of pillbox cavities. Each cavity, also called cell, is excited in a TM₁₁-mode coupled through small apertures on the axis. The Slater perturbation theorem states that the perturbed resonant frequency ω is given by [Sla46]

$$\frac{\omega^2 - \omega_r^2}{\omega_r^2} = \frac{N}{U} (\Delta U_m - \Delta U_e), \quad (2.62)$$

where ω_r is the unperturbed frequency, N the number of the apertures per cell, U the unperturbed, electromagnetic, stored, energy, and ΔU_m and ΔU_e are the time-averaged, magnetic and electric, energy deviations, respectively, as a result of the perturbation. In the middle of the structure, each cell has two apertures, so that $N = 2$. The electric field of the TM₁₁-mode is zero on the axis of the structure, so that $\Delta U_e \approx 0$. But the magnetic field does not vanish on the axis, so that an inductive coupling takes place. The

² The indices give the number of maxima of the field in 1st φ -direction, 2nd r -direction and 3rd z -direction (cylindrical coordinates).

resulting energy deviation of the magnetic component with respect to the unperturbed energy is [Wan98]

$$\Delta U_m = -\frac{2}{3} a^3 \mu_0 H_0^2 (1 - e^{-\alpha h} \cos \Psi), \quad (2.63)$$

where a is the radius of the apertures, μ_0 the permeability in vacuum, H_0^2 the amplitude of the magnetic field strength, α the decay constant of the evanescent mode inside the aperture of thickness h , and $\Psi = kl$ is the phase advance per cell of the travelling wave, with k its wave number and l the axial length of each cell.

The energy U stored by the electro-magnetic field of the TM₁₁-mode in the unperturbed cavity is given by

$$U = \frac{\pi}{8} b^2 l \epsilon_0 E_0^2 J_0^2(3.832), \quad (2.64)$$

where b is the cavity radius, ϵ_0 the permittivity in the vacuum, E_0 the amplitude of the electric field and $J_0(3.832)$ the zero order Bessel function of the first kind at the zero-crossing of J_1 . The cavity radius b is related to the unperturbed, resonant frequency by $\omega_r = 3.832c/b$. Substituting Eq. (2.63) and Eq. (2.64) into Eq. (2.62), the dispersion relation will be

$$\omega = \frac{3.832c}{b} \sqrt{1 - \kappa (1 - e^{-\alpha h} \cos \Psi)}, \quad (2.65)$$

with

$$\kappa = \frac{32a^3 \mu_0 H_0^2}{2\pi b^2 l \epsilon_0 E_0^2 J_0^2(3.832)}. \quad (2.66)$$

The phase velocity v_p is then

$$v_p \equiv \frac{\omega}{k} = \frac{3.832cl}{b\Psi} \sqrt{1 - \kappa (1 - e^{-\alpha h} \cos \Psi)}. \quad (2.67)$$

Generally, $\kappa \ll 1$, so that the group velocity v_g can be written as

$$v_g \equiv -\frac{d\omega}{dk} = \frac{3.832cl}{2b} \kappa e^{-\alpha h} \sin \Psi. \quad (2.68)$$

Obviously, the dispersion of the TM₁₁-mode is negative and the phase velocity and the group velocity have different signs. At LOLA, the phase advance amounts to $\Psi = 2\pi/3$. This means that the wavelength of the RF spans three cells of the structure.

The field distribution within the real cavity with openings for entry and exit of the beam is different from the pure TM₁₁-mode, that can exist only in closed cavities. Longitudinal magnetic and transverse electric field components are introduced. Therefore, so-called hybrid modes are used in describing transverse deflecting RF cavities.

The Fourier-analyzed field components of the TM₁₁-like, TE-TM-hybrid mode in cylindrical coordinates of the first-order solution for the lowest-order deflection mode with the phase velocity at $v_p = c$ are [Alt64]

$$\begin{aligned} E_r &= E_0 \left[\left(\frac{1}{2} kr \right)^2 + \left(\frac{1}{2} ka \right)^2 \right] \cos \theta \\ E_\theta &= E_0 \left[\left(\frac{1}{2} kr \right)^2 - \left(\frac{1}{2} ka \right)^2 \right] \sin \theta \\ E_z &= iE_0 kr \cos \theta \\ Z_0 H_r &= -E_0 \left[\left(\frac{1}{2} kr \right)^2 - \left(\frac{1}{2} ka \right)^2 + 1 \right] \sin \theta \\ Z_0 H_\theta &= E_0 \left[\left(\frac{1}{2} kr \right)^2 + \left(\frac{1}{2} ka \right)^2 - 1 \right] \cos \theta \\ Z_0 H_z &= -iE_0 kr \sin \theta, \end{aligned} \quad (2.69)$$

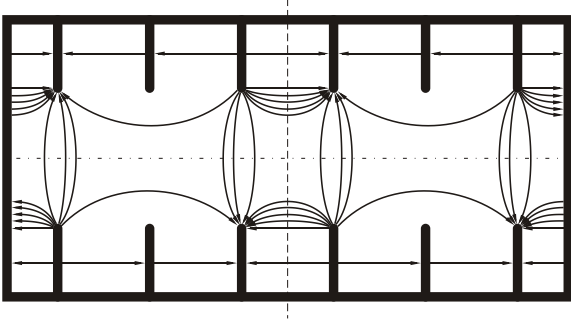


Figure 2.9: Time snap-shot of the electric field distribution of the TM_{11} -mode [Emm00]. The period spans three cells, so it is a $2\pi/3$ -mode. The field distribution in LOLA is given by Eq. (2.69).

where a is the radius of the aperture and Z_0 the free-space impedance. For a time snap-shot of the field distribution see Fig. 2.9. Using the Lorentz force on a particle with charge e the force in rectangular coordinates can be derived as

$$\begin{aligned} F_x &= 0 \\ F_y &= eE_0 \\ F_z &= ieE_0kr \cos \theta \end{aligned} \quad (2.70)$$

The transverse force is uniform in magnitude and direction over the aperture. Therefore, an aberration-free deflection is possible. Although the force arises from magnetic and electric fields it can be given using an equivalent electric field E_0 . The longitudinal force component F_z is 90 deg out of phase and linear dependent on the radius r . It is negligible small even for position-offsets of about a few millimeters.

The pointing vector gives the power that flows through an area. The integral over the whole aperture S gives the power P_z that flows through the cavity in longitudinal direction

$$P_z = \frac{1}{2} \Re \left\{ \int_S \mathbf{E} \times \mathbf{H}^* d\mathbf{S} \right\}, \quad (2.71)$$

with the complex conjugated magnetic field \mathbf{H}^* . For the field of LOLA this results in [Alt64]

$$P_z = \frac{1}{2} \pi a^2 \frac{|E_0|^2}{Z_0} \left(\frac{1}{2} ka \right)^2 \left[\frac{4}{3} \left(\frac{1}{2} ka \right)^2 - 1 \right]. \quad (2.72)$$

The expression in the squared brackets determines the sign of the power. For $ka < \sqrt{3}$ the power is negative and for $ka > \sqrt{3}$ it is positive. This determines if the wave is a forward or a backward travelling wave. In the case of LOLA using a frequency of 2.856 GHz the cross-over value of the aperture radius is $a = 29$ mm. The aperture of LOLA has a radius of 22.44 mm. This means that the wave travels backwards with respect to the group velocity. Thus the RF input coupler is mounted at the downstream end of the cavity (see Fig. 3.2).

The cavity is of the constant impedance type. This means that the aperture of the irises and the diameter of the structure are constant over the whole structure. Thus there is no compensation for the attenuation of the field along the cavity³. The field undergoes an attenuation of

4.14 dB while its travel through the structure. One can calculate the effective transverse deflecting voltage using

$$V_0 \approx 1.6 \text{ MV} \cdot \frac{L}{\text{m}} \sqrt{\frac{P_0}{\text{MW}}}, \quad (2.73)$$

where L is the length of the structure and P_0 the peak input power. With a general maximal input power at TTF of 18 MW, the deflecting voltage amounts to 24.7 MV. This corresponds to a kick angle of 3.18 deg and a vertical streak of 3.81 fs/px at the screen of LOLA.

³ This is in contrast to a constant-gradient structure where the group velocity is slowed down by decreasing the aperture so that the fields remain constant.

3 The experimental setup around LOLA and the principle of measurement

LOLA was developed at the Stanford Linear Accelerator Center (SLAC), California, USA. Its name is assembled from the first letters of the three designers Greg Loew, Rudy Larsen and Otto Altenmueller. In collaboration with SLAC, LOLA was installed at the TTF VUV-FEL to investigate longitudinal properties of the electron bunches.

The core of the setup is the 3.64 m long cavity. The electric field of a travelling wave deflects the electrons in vertical direction depending on the longitudinal position of the electrons in the bunch, and makes the head and the tail of the bunch separable. The bunch streaked in this way, hits an off-axis, optical transition radiation (OTR) screen. A dipole magnet with very fast rising and falling magnetic field, the kicker (Sec. 3.4), deflects one bunch of the bunch train onto the screen. The transition radiation is extracted through a window out of the vacuum chamber and imaged using a CCD camera.

Up- and downstream of the cavity there are correction magnets (steerers) and focussing magnets (quadrupoles). To measure the horizontal and vertical position of each bunch in a train, beam position monitors (BPMs) are used.

The different elements of the setup are treated in this chapter.

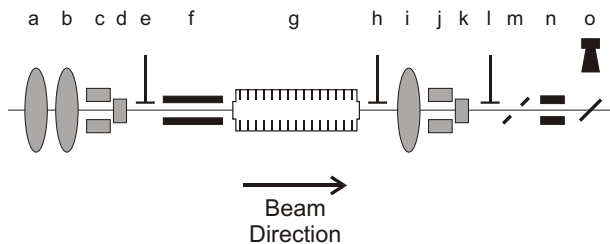


Figure 3.1: The layout of the experimental setup around LOLA. Elements: a - Quadrupole 1, b - Quadrupole 2, c - Horizontal Steerer 1, d - Vertical Steerer 1, e - BPM 1, f - Kicker, g - LOLA, h - BPM 2, i - Quadrupole 3, j - Horizontal Steerer 2, k - Vertical Steerer 2, l - BPM 3, m - OTR Screen of LOLA, n - Collimator, o - OTR Screen. This sketch was not drawn to scale.

3.1 The cavity

The LOLA cavity is the place where the deflection occurs. Such an RF transverse deflecting structure is an invention of the 60's [Alt64], [Loe65]. Several variations were tried until the final design was found with LOLA IV.

This cavity is a 3.64 m long disk-loaded waveguide structure made of copper. In Fig. 3.2 a cut-away view is shown. The structure consists of 104 each 35 mm long cells which are coupled via irises with a diameter of 44.88 mm.

The cavity is temperature stabilized at 45 degrees C. According to the expansion coefficient of copper, it is possible to change the resonance frequency by 50 kHz/K. Along the cavity a travelling electro-magnetic wave propagates with a frequency of 2.856 GHz. The RF is amplified by a klystron

to a power of up to 23 MW. The timing jitter of the klystron amounts to 68 fs, corresponding to 0.07 deg of the RF. A 75 m long waveguide leads the RF from the klystron to the cavity. The theoretical attenuation of the waveguide amounts to 1.6 dB, a measurement yielded 2.6 dB. Therefore, the maximal input power at LOLA amounts to 18 MW. As the RF phase shift of about 2.8 deg/K, the waveguide is heater stabilized at 35 degrees C. For more details see [Nag04].

As mentioned already, the TM_{11} -like hybrid mode used for the deflection of the electron bunches, is a dipole mode (see Fig. 2.8). The direction of the transverse field is determined by the position of the RF input coupler where the RF is fed into the cavity. At TTF the coupler is mounted at the top of the structure so that the deflection occurs vertically. Imperfections of the structure can cause a rotation of the polarization plane. To avoid this, two mode-locking holes are inserted into the disks (see Fig. 3.2) which cause an additional coupling of the fields of the adjacent cells. [Emm00]

Due to the travelling wave form of the exciting power, the whole RF power has to be coupled out and absorbed at the reverse end of the structure with respect to the input coupler. Otherwise, it would be reflected and a standing wave would form. For that purpose, a dry external load was installed. Due to the negative dispersion, the load is positioned at the upstream end and the input coupler at the downstream end of the cavity. [Nag04]

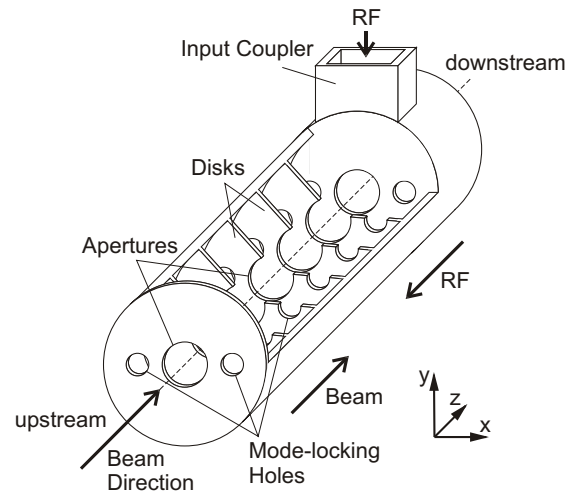


Figure 3.2: Cut-away view of the cavity LOLA. The RF is led into the cavity via an input coupler at the downstream end. The RF travels against the beam direction. Due to the negative group velocity of $v_g < 0$ with respect to the phase velocity, the wave travels downstream as fast as the beam. The big apertures in the disks cause a very strong coupling of the fields. The mode-locking holes avoid a possible rotation of the TM_{11} -mode.

3.2 The screen

To measure the charge distribution of the deflected bunch, an optical transition radiation screen is used. The screen used for LOLA consists of two components arranged horizontally at the left and at the right side of the beam. It is installed with an angle of 45 deg with respect to the incoming beam. Thus the radiation is led through a window out of the vacuum chamber with an angle of 90 deg.

Each screen has a width of 8 mm, a height of 26.5 mm and a thickness of 0.280 mm. The distance of the screens is 20 mm. Due to the horizontal rotation of 45 deg, the aperture for the beam is $\frac{20 \text{ mm}}{\sqrt{2}} = 14.1 \text{ mm}$. The total horizontal width of the electron bunch at this position is about 2 mm, the position-offset $\pm 1 \text{ mm}$. Thus, the un-kicked beam passes the screen without any disturbance.

The screens consist of aluminium coated silicon wafer. They are mounted at a vertically movable screen holder. At this holder there are 10 calibration boreholes (see Fig. 3.3). The horizontal and vertical distances to adjacent holes are 5 mm. They were used to calibrate how many μm at the screen correspond to one pixel at the CCD chip of the camera. For the results of this calibration see Sec. 5.3.

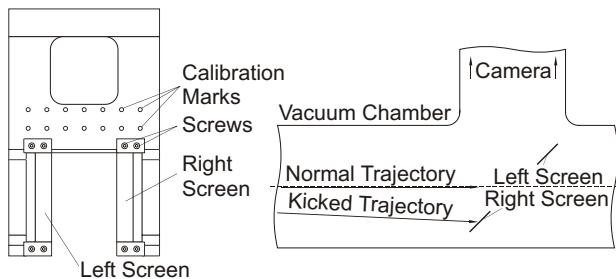


Figure 3.3: The off-axis screen of LOLA. The figure shows the screen holder with the two screens (left) and the positioning in the vacuum chamber (right). The calibration marks are used to correlate the mm at the screen and the pixel of the CCD chip. They have a distance of 5 mm. The left and the right screen have a distance of 20 mm. The un-kicked bunches pass the screen uninfluenced.

3.3 The camera and its optical system

After the bunch was deflected in the cavity it strikes the screen. The resulting optical transition radiation is guided to the camera via a mirror to reduce the overall radiation. Fig. 3.4 shows a sketch of the optical system. The total distance between CCD chip and screen amounts to 800 mm. The light is focused onto the CCD chip by a 200 mm objective with a lens aperture of 50 mm. Within the objective there is an aperture to improve the depth of field. It was adjusted to make a compromise between the depth of field and the total intensity of the light that enters the camera. With an effective aperture of $D = 25 \text{ mm}$ and a focal length of $f = 200 \text{ mm}$, the F-number κ of the objective amounts to

$$\kappa = \frac{f}{D} = 8 . \quad (3.1)$$

The camera is a digital camera BASLER A301f. It exhibits a sensor size of 658×494 pixels. Each pixel has a size of $9.9 \times 9.9 \mu\text{m}$. The output format is mono 8 bit/pixel. In this operation mode 640×480 pixels are used to take

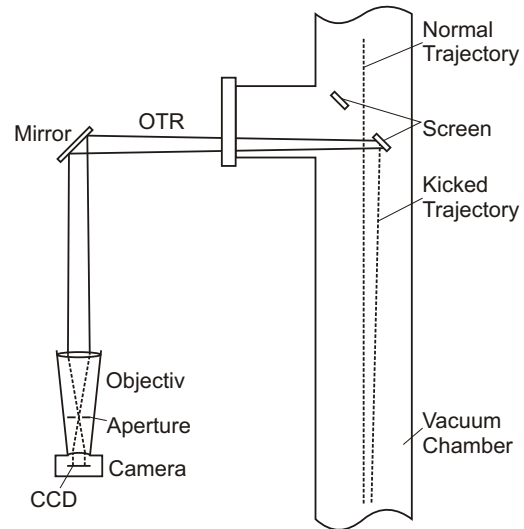


Figure 3.4: Sketch of the optical system of the camera of LOLA. While the normal trajectory remains uninfluenced the kicked bunch strikes the screen. The resulting OTR transmits a window of the vacuum chamber and is led via a mirror onto the CCD of the camera. The total length of this path is 800 mm. The objective has a focal length of 200 mm. The aperture increases the depth of field. This sketch is not drawn to scale.

LOLA images. The trigger occurs externally to synchronize the camera with the beam. The minimum exposure time is $1 \mu\text{s}$. The time difference of the first and the last photon produced by the bunch is less than 10 ps. Thus the resulting images are an integration over the whole light produced by the bunch.

3.3.1 The resolution of the optical system

To measure the resolution of an optical system, a sinusoidal test pattern is convenient. The M-19-80 transmission pattern was manufactured by APPLIED IMAGE Group-OPTICS, New York, USA. Fig. 3.5 shows a photograph of this pattern. It was illuminated diffusely from behind and recorded with the camera. The pattern was positioned at a distance of 800 mm to the camera so that it was in focus.

The pattern contains many different areas applied at a film. The divisions 1 and 4 in Fig. 3.5 a) exhibit different nuances of gray. They were not used for our measurement. In the divisions 2 and 3 sinusoidal modulations of transmittance are applied. Plots of the measured transmittance are shown in Fig. 3.5 b) and c). At a spatial frequency of 20 mm^{-1} (cycles per millimeter) in part c) the amplitude gets small and increases again. This is caused by the Moiré-Effect. It was hard to adjust the pattern so that the lines are parallel to the rows of pixels of the camera. So, especially for this area we had to find a region without any Moiré-Lines.

The ratio of the difference of the maximum and the minimum of the intensity I of the sine and their sum is defined as the modulation

$$M = \frac{I^+ - I^-}{I^+ + I^-} . \quad (3.2)$$

This ratio decreases with increasing spatial frequency. The ratio of the modulation in the image and the modulation of the object relating to the spatial frequency is called the

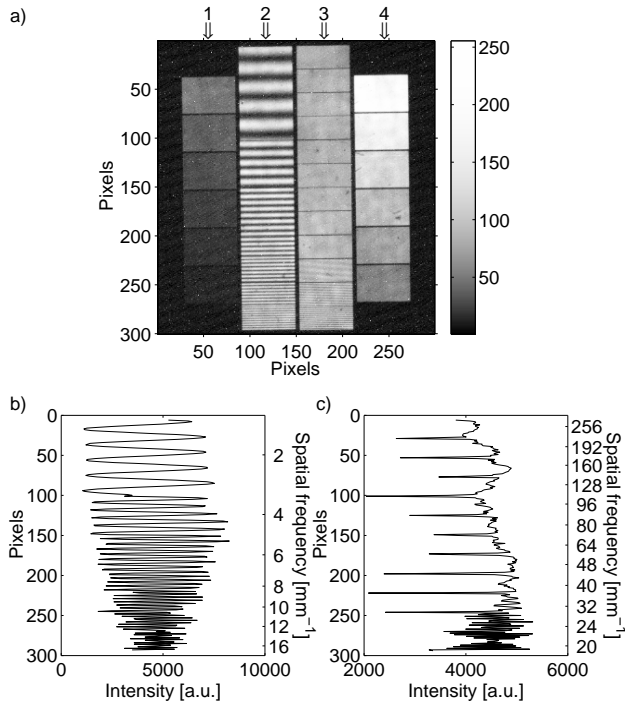


Figure 3.5: Measurement of the MTF. a) An image of the sinusoidal test pattern. Columns 1 and 4 are areas with different nuances of gray. Column 2 contains areas with sinusoidal modulations of higher and lower transmittance with spatial frequencies from 2 to 16 mm^{-1} . Column 3 is the same like column 2 with spatial frequencies from 20 to 256 mm^{-1} . b) and c) show the measured profiles of column 2 and 3 of part a), respectively.

modulation transfer function (MTF). For a more detailed description of the MTF see [Lam83].

While the frequency of the modulation increases with increasing spatial frequency up to 20 mm^{-1} it decreases at higher spatial frequency. This effect is called aliasing. An

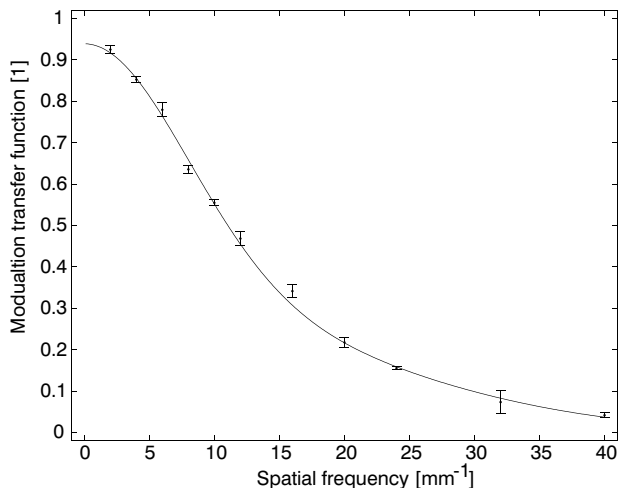


Figure 3.6: The modulation transfer function (MTF) of the optical system. The solid line represents a fit of the Fourier transformation of a convolution function, consisting of the step function of the pixels and a sum of two Gaussians.

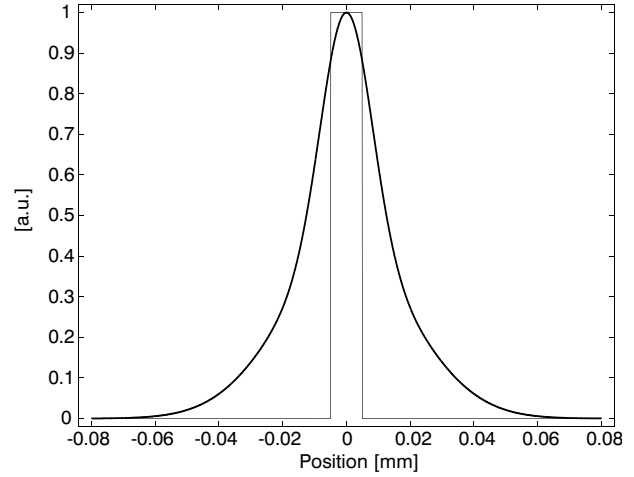


Figure 3.7: The transfer function (thick line) of the optical system. The parameters are obtained by the fit of the MTF. The step function represents the pixels of the CCD.

undersampled sinusoidal signal appears with a lower frequency. A certain modulation is observable at 40 mm^{-1} . There occurs only one oscillation. The existence of a modulation indicates that the optical system does not limit the resolution until this point.

In Fig. 3.6 the averages of the modulation of 10 images and the standard deviations are plotted. The solid line denotes a fit of the Fourier transformation of a convolution function, that is composed of a step function, representing the pixel of the CCD, and the transfer function of the optical system. The best fitting results gave a transfer function consisting of the sum of two Gaussian distributions. In Fig. 3.7 the step function and the transfer function in position space are plotted, using the parameters obtained by the fit. The width of the step function amounts to 9.9 μm , the size of one pixel of the CCD. The half width of the half maximum of the Gaussian functions determines the resolution r of the optical system to

$$r = 12.6 \mu\text{m} . \quad (3.3)$$

In Sec. 5.3 we will see that one pixel of the CCD chip corresponds to $\approx 25 \mu\text{m}$ at the screen or in our case at the patterned film. The distance of two points has to be at least 50 μm to distinguish them. This means that the resolution of the total system is limited by the CCD chip of the camera.

3.4 The kicker

As mentioned above the OTR screen used to make the charge distribution visible, is an off-axis screen. Thus “quasi-parasitic” measurements are possible. This means that LOLA images can be taken while the linac works in normal operation. To lead the beam onto the screen, a kicker is installed.

A kicker is a dipole magnet with special properties. It is used to produce a magnetic field for a short time. A high inductance would enlarge the rise and fall time. Thus it is minimized by using air-core coils with a small number of windings. Such a low inductive coil has to be impressed with a voltage in the range of kilovolts, to produce a strong magnetic field. In our case 3.8 kV are sufficient to center

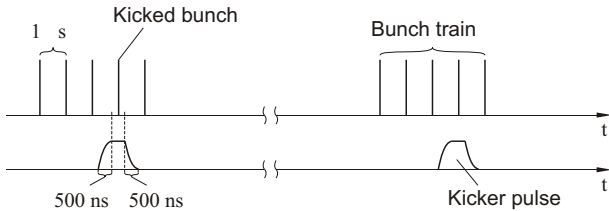


Figure 3.8: Sketch of the timing of the kicker pulse. With a rise and a fall time of the kicker pulse of 500 ns each, it is possible to kick only one bunch out of the bunch train.

the bunch horizontally at the screen. The duration of the kicker pulse is shorter than $1 \mu\text{s}$. The time delay between the bunches within a bunch train amounts to $1 \mu\text{s}$. So, with a rise time of 500 ns and the equal fall time only, one bunch is kicked. The other bunches remain undisturbed (see Fig. 3.8).

At the kicker the corresponding part of the metallic vacuum chamber was exchanged for a ceramic one. Thus eddy currents are avoided so that the magnetic field of the kicker penetrates the chamber faster and the pulse duration is short. A thin metallic film is necessary to discharge currents (“wake fields”) generated by the passing bunch. Therefore, the interior surface is sputtered with copper.

The kicker is positioned in front of LOLA. So, the kick to the right with respect to the flight direction occurs before the vertical streak. In the cavity the electric field distribution is independent of the horizontal position. Therefore, the streak is independent of the kicker position.

Since the kicker bends the beam trajectory, dispersion is generated. The dispersion D is defined in Eq. (2.65) as

$$D = \frac{\Delta x}{\Delta p/p_0} , \quad (3.4)$$

where Δx is the horizontal position-offset at a certain position of the linac, and $\Delta p/p_0$ the fraction of the momentum difference and the total momentum. Δx can be derived by using the Lorentz force

$$\Delta x = eldB \left(\frac{1}{p} - \frac{1}{p_0} \right) , \quad (3.5)$$

with e the elementary charge, l the length of the magnetic field B of the kicker, and d the distance between the center of the kicker and the screen (see Fig. 3.9). The dispersion amounts finally to

$$D = 10 \text{ mm} . \quad (3.6)$$

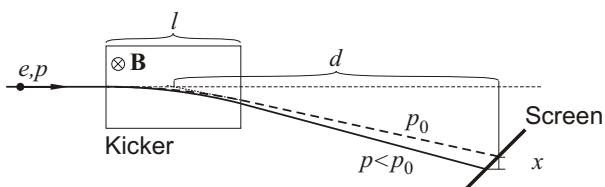


Figure 3.9: Dispersion at the screen of LOLA, caused by the kicker. Particles with a momentum p deviating from the nominal momentum p_0 strike the screen with a position-offset Δx because of a different deflection in the magnetic field \mathbf{B} .

We will see in Sec. 5.3 that one pixel of the CCD chip of the camera corresponds to $\approx 26.8 \mu\text{m}$ at the screen. So, with a reasonable estimation of an energy spread of 1% the total position-offset error at the screen amounts to

$$\Delta x \approx 100 \mu\text{m} \hat{=} 4 \text{ px} . \quad (3.7)$$

The total bunch has a width of 2 mm or 75 px. So, the position-offset error caused by the kick is about 5%. We will neglect this contribution in the following.

3.5 The beam position monitors

For many purposes it is necessary to know at which transverse position the beam passes an element of the linac. For example, if a bunch enters a quadrupole off-axis it experiences not only focussing or de-focussing but also a kick. With every kick, unwanted dispersion is produced. Therefore, the aim is to guide the bunch on-axis through the entire linac.

The beam has to be centered in various components also in order to minimize transverse wake fields. If a charge distribution travels within a conducting vacuum chamber electromagnetic fields travel together with it. At irregularities of the chamber, e.g. at flanges or edges, a part of these fields get trapped and are left behind by the bunch. Such fields are called wake fields. They can disturb the motion of the following bunches significantly and have to be minimized by choosing the optimal orbit.

Therefore, it is important to measure the transverse position of the beam. The devices designed for this purpose are beam position monitors (BPM). Around LOLA so-called stripline BPMs are installed. Fig. 3.10 shows schematically how they work. The vacuum chamber, that is just a round pipe, is surrounded by four bulges. Within these

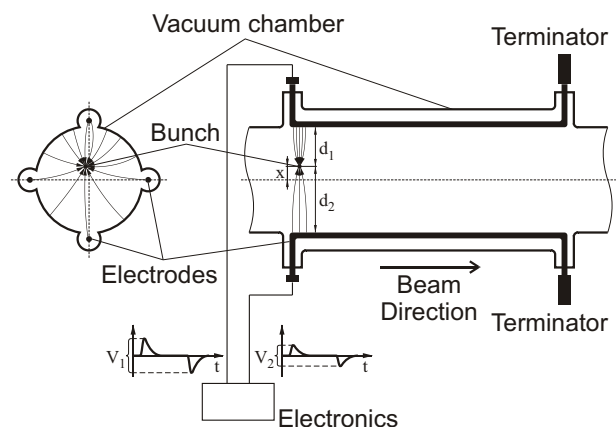


Figure 3.10: Principle of a stripline BPM. A transverse (left) and a longitudinal (right) cut are shown. The electric field of the bunch causes a current in the electrodes that divides into two signals. One of the signal flows directly to the electronics. The other one flows to the terminator, is reflected and enters the electronics with negative amplitude. The electronics considers the amplitudes V_1 , V_2 of signals of electrodes at opposite sides which depend on the distances d_1 , d_2 between bunch and electrode. Then the fraction of the difference Δ and the sum Σ are calculated. This can be used to calculate the transverse position x of the beam within the vacuum chamber.

bulges wires are clamped. One end of each wire is terminated with a 50 Ω resistor and the other end is connected to the readout electronics.

The electric field of the bunch induces a voltage in the wire. A current flows in both directions. The signal that travels to the terminator is reflected and returns with a phase jump of 180 deg. Therefore, it enters the readout electronics with negative amplitude and with a time delay with respect to the first signal. The difference V of the amplitudes of these time-delayed signals is used for the following evaluation because it is less error-prone than taking only the positive or the negative amplitude.

The amplitudes of the signals from two opposite wires are proportional to the ratio of the charge q within the bunch and the distance d between the bunch and the wire. With that relation, it is possible to calculate the position x of the bunch within the vacuum chamber by normalizing the difference Δ of the amplitudes V_n with their sum Σ , assuming $(d_2 - d_1)/(d_2 + d_1) \ll 1$

$$\begin{aligned}\Delta &= V_1 - V_2 \sim q \cdot \left(\frac{1}{d_1} - \frac{1}{d_2} \right) = q \cdot \left(\frac{d_2 - d_1}{d_1 d_2} \right) \\ \Sigma &= V_1 + V_2 \sim q \cdot \left(\frac{1}{d_1} + \frac{1}{d_2} \right) = q \cdot \left(\frac{d_2 + d_1}{d_1 d_2} \right) \quad (3.8) \\ \frac{\Delta}{\Sigma} &\sim (d_2 - d_1) = 2x .\end{aligned}$$

To figure out the factors of proportionality, one has to do a calibration measurement using the steerers in front of each BPM.

3.6 The magnets around LOLA

Fig. 3.1 shows that the facility around LOLA is equipped with many different magnets. While the quadrupoles are used to focus the beam, the dipoles, called steerers, fine-tune the position-offset of the beam.

3.6.1 The quadrupole magnets

The electrons in an accelerator exhibit an angular divergence. If one would not compensate that, the transverse size of the bunch would increase until the particles impinge at the vacuum chamber and get lost. At energies larger than 4 MeV quadrupoles are used to avoid this. Fig. 3.11 shows how focussing with such a magnet works.

Via four hyperbolically shaped pole shoes a transverse magnetic field is excited. This magnetic field has the property

$$B_x = gy, \quad B_y = gx, \quad B_z = 0 \quad \text{with } g = \frac{\partial B_y}{\partial x} . \quad (3.9)$$

Because $\text{rot}\mathbf{B} = 0$ within the vacuum chamber the gradients g in both directions are equal

$$g = \frac{\partial B_y}{\partial x} = \frac{\partial B_x}{\partial y} . \quad (3.10)$$

The resulting equations of motion of the electrons within the magnet are

$$x'' + kx = 0 \quad (3.11)$$

$$y'' - ky = 0 , \quad (3.12)$$

where $k = \frac{eg}{p}$ with the elementary charge e and the momentum p . For $k > 0$ the trajectory is sinusoidal in horizontal and exponentially increasing in vertical direction. Thus

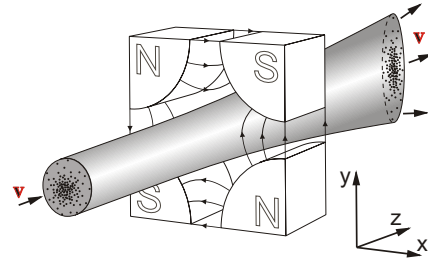


Figure 3.11: The focussing properties of a quadrupole. An electron bunch with an arbitrary distribution passes the magnetic field of a quadrupole. In this arrangement the bunch is focused in the horizontal plane and de-focused in the vertical one. To get a net focussing in both directions, a second quadrupole rotated by 90 deg with respect to the first one has to be installed (not in this drawing).

the focussing takes place only in one transverse plane. To avoid that the beam diverges in the other direction, another quadrupole with opposite field is installed. Such a doublet is called a FODO cell, an array with alternating focussing and de-focussing quadrupoles and a drift-space in-between. [Ros05]

The quadrupoles produce a gradient per coil current of 0.0692 (T/m)/A. This corresponds to $k=0.0466$ (1/m²)/A. The magnetic length amounts to 336 mm. By changing the current of the quadrupole 3 (see Fig. 3.1) behind the cavity one changes the resolution at the screen of LOLA (see Sec. 5.5). To be independent of the quadrupole current, a corresponding calibration has to be done in the future.

3.6.2 The steerer magnets

Along the accelerator, the beam can deviate from the design orbit. Small dipole magnets are used, to correct these deviations. Such magnets are called steerers or correction coils. They consist of a small coil and an iron yoke.

For example the steerers in front of the undulators correct the position-offset of the beam, to optimize the SASE efficiency. Steerers at other positions along the linac are used for calibrations in many forms. For example the beam position monitors (BPM) can be calibrated, because the steerers change the position-offset of the bunches in a known way.

3.7 The collimator

When the electrons of a bunch transit the OTR screen a shower of particles is produced. Directly downstream of LOLA there are another camera and a lot of electronics which have to be protected against such showers. For that purpose, a collimator is installed to absorb the particles. However a certain amount of particles pass this collimator. They are able to damage the permanent magnets of the undulators. To avoid this, other collimators with a much smaller aperture are installed 3 m downstream of the screen of LOLA. They are not shown in Fig. 3.1.

The collimator directly behind the screen is a block of the Aluminium alloy AlMg_{4.5}MnF₂₇. This alloy is very hard and ensures that the collimator survives high beam-losses. On-axis of the vacuum chamber there is a bore hole inside this block with a diameter of 30 mm (technical

specifications originate from [Sch05]). The unkicked bunches transit the collimator through this hole. The kicked bunch and the particles produced in the screen enter the collimator off-axis and are absorbed.

4 Realization of the synchronization

LOLA is supposed to streak the electrons within a bunch. The centroid of the charge distribution has to stay nearly undeflected. This means that the bunch has to enter the cavity at the zero-crossing of the deflecting RF. Therefore, a synchronization of the RF and the timing of the accelerator is necessary. The aimed precision is about 100 fs rms, corresponding to 0.1 deg rms of the deflecting wave. Thus, a safe assumption on the maximum expected phase error is $\approx 4 \times 100$ fs, which would occur at a probability of $< 10^{-5}$ if a random error distribution is assumed. At the maximum RF power of 18 MW, this would cause a maximum, vertical jumping of the bunch of 2.7 mm at the OTR screen. This corresponds to 16% of the vertical dimension of the screen. With an additional rms timing-jitter of the bunch of 100 fs, the vertical jumping will be 23%. The realization of the synchronization is presented in this chapter.

4.1 The frequency generating setup

All reference and timing signals are derived from the master oscillator running at 9.027775 MHz. The 1.3 GHz reference signal is generated by multiplication with 144 yielding 1.2999996 GHz [Edw95]. Many elements of the VUV-FEL get a trigger signal which relates to one main trigger event, generated by the so-called rep-rate generator. This device excites a signal, synchronized to the 50 Hz of the public mains and the 9 MHz of the master oscillator. It detects a zero-crossing of the 50 Hz and waits then for the next zero-crossing of the 9 MHz. At this moment the trigger signal is generated in terms of a rising edge. This prevents fluctuations due to a shifting phase of the mains, and ensures a stable phase relation of the beam and the RF of the acceleration modules. Indeed, it has been found, that the zero-crossings of the mains jitter by up to 100 μ s.

Because the mains is not stable, the distance of the triggers signals vary by ≈ 100 μ s.

With this mode of operation, only a partially satisfying solution (described in Sec. 4.2) of the synchronization of the 2.856 GHz to the master oscillator was possible. Because there is no multiple of the 9 MHz master oscillator within the tuning range of the LOLA structure, each beam trigger occurs at a seemingly random phase of the 2.856 GHz.

To guarantee a proper operation of LOLA, there are in principle two solutions: The frequency generation could be restarted with each machine trigger or the machine trigger could be modified such, that there is always an integer number of cycles of the 2.856 GHz between two macro pulses.

The first possibility would have offered the most flexibility, but it was considered problematic for the stability of the reference signal, if the generator would have had to perform a step-change for each RF pulse. Instead it was decided to manipulate the trigger generator. It was calculated that a multiple of $\frac{9}{11}$ MHz = 820 kHz is close enough to the 2.856 GHz so that the tuning was possible without too much effort. Therefore, one input was added to the rep-rate generator so that it could be synchronized to 9 MHz, 50 Hz, and 820 kHz. The 820 kHz were generated with a counter module producing one output pulse every

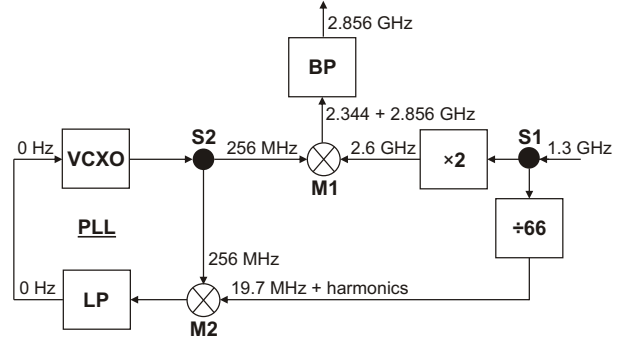


Figure 4.1: Synchronization of the RF with the accelerating modules. The resulting frequency of 2.859 GHz is a mixture of the doubled 1.3 GHz, which the accelerating modules use, and the 256 MHz. The latter is generated via phase lock loop (PLL). The input of the PLL is the 13th harmonic of the 66th fraction of the 1.3 GHz. A more detailed description is found in the text.

11th input pulse. [Hue05a]

Fig. 4.1 shows a sketch of the circuit generating a 2.856 GHz signal synchronized to the 9 MHz master oscillator. To generate such a signal, two different frequencies of 2.6 GHz and 256 MHz are mixed (M1). The advantage over direct multiplication is the favorable phase noise. A mixer is an electronic device that multiplies two sine oscillations obeying the formula

$$\sin(f_1 t + \varphi_1) \cdot \sin(f_2 t + \varphi_2) = \frac{1}{2} \left(\cos[(f_1 - f_2)t + (\varphi_1 - \varphi_2)] - \cos[(f_1 + f_2)t + (\varphi_1 + \varphi_2)] \right). \quad (4.1)$$

The result are two superimposed signals, the first with a frequency of the sum of the incoming ones (2.856 GHz) and the second with the difference (2.344 GHz). We are only interested in the frequency of 2.856 GHz and cut off the other one using a bandpass (BP) filter. The phase of the mixed signal is the sum of the individual phases, and hence the phase jitter is the sum of the jitter of the individual signals. This explains the advantage of this method: With the multiplication method, a signal at 820 kHz would have to be multiplied by 3480. Every phase noise within the bandwidth of the PLL would have been multiplied by the same amount. In the chosen solution the phase noise of the 1.3 GHz is doubled and added with the noise of 19.7 MHz multiplied by 13. [Hue05a]

To generate two different frequencies which are mixed in M1, the incoming signal with $144 \cdot 9$ MHz = 1.3 GHz is split (S1). The frequency of one of the resulting signals is doubled and then led directly to the mixer M1. The other signal outgoing of S1 is divided by 66. This is accomplished with counter chips producing a short needle pulse every 66th cycle of the 1.3 GHz. Thus a 19.7 MHz signal with higher harmonics results.

The 13th harmonic is exactly the 256 MHz we require. To separate it from the other frequencies and to produce

a clean and noiseless sine wave, a phase lock loop (PLL) is used: A voltage controlled crystal oscillator (VCXO) generates a frequency of about 256 MHz. Via an external DC voltage this frequency can be fine-tuned. The DC voltage results from a mixture (M2) of the 13th harmonic of 19.7 MHz and the 256 MHz generated by the VCXO. The difference frequency between the 13th harmonic of the 19.7 MHz and the 256 MHz is approximately 0. According to Eq. (4.1) this results in a low frequency signal proportional to the phase difference between the two. All other harmonics produce harmonics of 19.7 MHz on the IF-side [Hue05a]. A low-pass filter is used to only choose the DC part. The higher the difference of the phases of the two signals at M2, the higher is the DC voltage and the more the 256 MHz are tuned. The VCXO works as a proportional regulator in phase and as an integral regulator in frequency so that the differences of the two input signals at M2 are minimized. The splitter S2 divides the resulting signal so that it can be used for the mixture at M1 and thus for the generation of the 2.856 GHz signal used for LOLA.

4.2 Temporary solution

As described above the 256 MHz are generated by many multiplications and divisions. The incoming 1.3 GHz frequency is the product of 144 · 9 MHz. Then it is divided by 66 and multiplied with 13. Starting from the 9 MHz the decomposition of the prim factors of the 256 MHz is

$$9 \text{ MHz} \cdot \frac{2^3 \cdot 3 \cdot 13}{11} \approx 256 \text{ MHz} .$$

Obviously 256 is not an integer multiple of 9. Therefore, it was not possible to synchronize the 2.856 GHz to 9 MHz as long as the synchronization of the master oscillator to the $\frac{9}{11}$ MHz = 820 kHz was not realized.

To be able to take measurements with LOLA anyway, we had to find another solution. Thus we divided the incoming 1.3 GHz by 432 and obtained 3 MHz with harmonics. The 85th harmonic is about 255 MHz, very close to the desired 256 MHz. The corresponding decomposition of the prim factors is

$$9.027775 \text{ MHz} \cdot \frac{5 \cdot 17}{3} \approx 255.786958 \text{ MHz} .$$

Of course 255.786958 is also not an integer multiple of 9.027775. But the advantage was that at every third shot the RF of LOLA was synchronized to the beam. So, we have had a probability of 1:2 that we hit the bunch at the right time and kick it onto the off-axis screen. And indeed if we took ten images at least three of them showed the bunch.

Besides the poor efficiency the drawback of this solution was that the harmonics of the 3 MHz are very close. Therefore, the PLL had difficulties to distinguish between the different frequencies.

Another point to mention is, that the cavity had to be modified. The resulting frequency of this configuration was 2.855 GHz. It is smaller than the normal 2.856 GHz. This means that the wavelength of the RF is oversized with respect to the geometrical dimensions of the cavity. To increase its length, the temperature of the cavity was increased.

5 Calibration measurements

Due to many external influences, systematic deviations from the ideal functioning of a device occur, which are almost impossible to predict. In order to determine the quantitative properties of a measuring system such as LOLA, calibration measurements need to be done.

5.1 Measurement of the RF power of LOLA

As described in Ch. 3, electro-magnetic fields are used to deflect and to streak the electron bunch. The high power radio frequency (RF) is generated in a klystron and then transported to the cavity of LOLA via waveguides. This transport is afflicted with losses and, therefore, power measurements are necessary. Fig. 5.1 illustrates the principle of the power measurements. At a reasonable position along the waveguide, for example in front of the cavity, two holes are drilled. Thus a very small fraction of the RF is coupled out. A second, welded waveguide leads the RF to antennas. The holes have a distance of $\lambda_{\text{RF}}/4$, where λ_{RF} is the wavelength of the RF. Due to destructive interference in the backward direction, power can be measured only at the forward antenna. The backward antenna is useful to measure the reflected power that travels through the waveguide in the other direction. The antennas are arranged with a distance of $\lambda_{\text{RF}}/4$ to the closed end of the waveguide. So, the reflected electro-magnetic fields from the closed ends and from the antennas interfere destructively. In this way the whole power is absorbed. This principle of course can only work properly at a certain wavelength λ_{RF} and harmonics. [Hue05a]

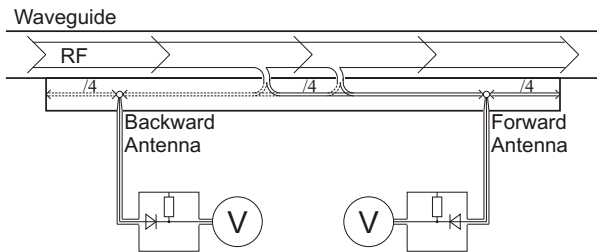


Figure 5.1: Principle of RF power measurement. A small amount of RF is coupled out through two holes into a second waveguide. The distance of $\lambda/4$, where λ is the wavelength of the RF, has the effect that the forward antenna only measures forward power (solid lines) and the backward antenna only the reflected one (dashed lines). The antennas are arranged in a distance to the closed end of $\lambda/4$ so that they absorb the whole RF. Using a potential divider consisting of a diode and a resistor the amount of power can be measured via a voltmeter.

Using coaxial cable a potential divider, consisting of a diode and a resistor, is connected to the antennas to measure the power of the RF. As a diode is a rectifying device the current flows only in one direction through the resistor and the diode. The average current is, therefore, larger than zero despite the alternating voltage. The total amount of this average current is determined by the characteristic curve of the diode sketched in Fig. 5.2. The

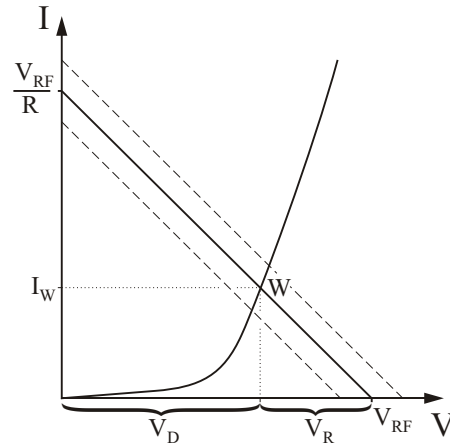


Figure 5.2: Characteristic curve of a diode. The shape is similar to an exponential function. The solid straight line is the resistance line at a certain total voltage V_{RF} and resistance R . The intersection points with the axes denote the current $I = \frac{V_{\text{RF}}}{R}$ and the voltage $V = V_{\text{RF}}$ if the diode was not in the circuit. The intersection point of diode and resistance line corresponds to the working point W and, therefore, the working current I_W and the distribution of the total voltage among the resistor V_R and the diode V_D . The dashed straight lines are examples for different V_{RF} and thus for different power of the RF.

characteristic curve of a diode obeys approximately an exponential function

$$I_W = \frac{V_R}{R} \sim \exp(V_D) , \quad (5.1)$$

where V_R and V_D are the voltages at the resistor with resistance R and the diode, respectively, and I_W is the current through the series connection at the working point. We measure the voltage V_R at the resistor and thus indirectly the current. The power P can then be calculated by

$$P = I^2 R . \quad (5.2)$$

By these relations, we are able to calibrate the set-up so that it measures the power of the RF. A provisional pre-calibration is already done by the manufacturer of the power measuring system described above. The resulting values are displayed in a control panel. Tab. B.1 contains the measuring data of the new, more precise calibration where the values of the display P_{display} are compared with the real RF power P_{real} measured with a network analyzer. These values originate from [Jon04]. In Fig. 5.3 these data are plotted. The solid line represents an exponential fit with the resulting parameters

$$P_{\text{real}} = 13.3 \text{ MW} \cdot \exp(0.050 \cdot \frac{P_{\text{display}}}{\text{MW}}) - 13.5 \text{ MW} . \quad (5.3)$$

It is obvious that a measurement at low power is difficult because of noise and the vanishing current below the threshold voltage of the diode. To increase the dynamic

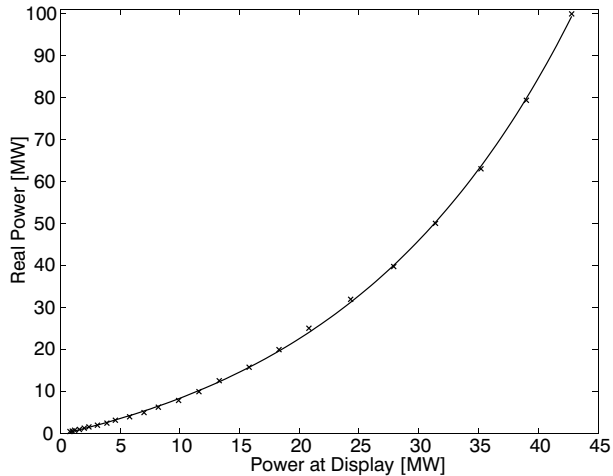


Figure 5.3: Calibration of the power measurement. Using a network analyzer the display on the control panel is compared with the real power in the waveguide. The corresponding data are listed in Tab. B.1. The solid line denotes an exponential fit (see Eq. (5.3)). At a power of 15.8 MW the display shows the correct value.

range, a system with two diodes was developed together with physicists of the SLAC, Stanford, USA [Fri05a].

The power is divided by a directional coupler into two signals. One of them is attenuated by 10 dB. After another attenuation of 8 dB the diode module used for the high power measurement is connected. The other output of the directional coupler is attenuated by 3 dB and filtered using a low pass filter. It is then followed by the diode module for the low power measurement.

Thus, the low power diode is supplied with a greater fraction of the RF power than the other. Its output signal increases very strongly and saturates at a certain power. The output of the high power diode increases more slowly and

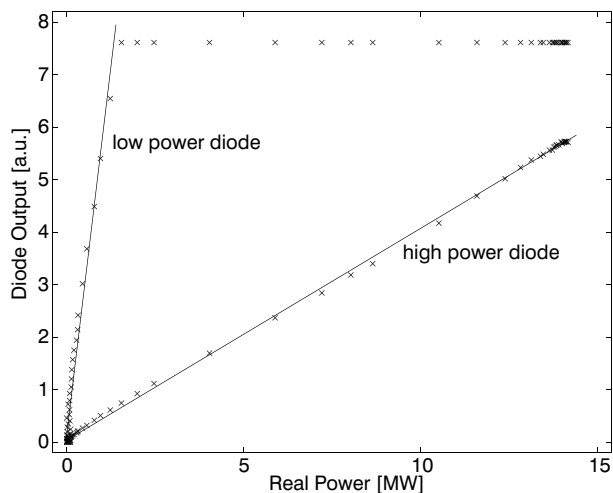


Figure 5.4: Calibration of the power measurement using two diodes. On the abscissa the real power is plotted. This scale is obtained using the calibration made by [Jon04] (see Eq. (5.3)). The solid lines denote the linear fits which are used for power calculation. The low power diode exhibits a steeper slope than the high power diode and saturates.

does not saturate. Fig. 5.4 shows the behavior of the diodes and the corresponding linear fits. The data are scaled for a better comprehension. The correct equations used to calculate the power in the cavity are

Low power diode :

$$P = (-1.88 \cdot 10^{-4} \cdot O_{low} + 1.36) \text{ MW} \quad (5.4)$$

High power diode :

$$P = (-2.48 \cdot 10^{-3} \cdot O_{high} + 20.87) \text{ MW} , \quad (5.5)$$

where P is the power and O_{low} and O_{high} are the output signals at the low and high power diode with arbitrary units.

5.2 The phaseshifter

It is not only necessary to know the power of the RF in LOLA, but also its correct phase. Sec. 3.1 describes how the deflection of the particles works. One can see that only at two special phases of a period the bunch is streaked without deflecting the center of mass. Therefore, between these points, called zero-crossing, the whole bunch is kicked. If the RF power is constant the strength of the kick depends on the phase. The position of the bunch can be measured with a beam position monitor (BPM). Fig. 5.5 shows a scan where the phaseshifter is moved over its full range and where the position is measured with BPM 2 (Fig. 3.1) located 4 m behind the center of the cavity (see Ch. 3). The set values correspond to a provisional calibration of the phase shifter.

This scan was made before the synchronization of the RF worked properly (Sec. 4.2). The probability to kick a bunch at the correct phase was 1:2. So, if one bunch would enter the cavity at a phase of 0 deg, the other two phases bunches sometimes experience are 120 deg and 240 deg. Therefore zero crossing with a spacing of 60 degrees is to

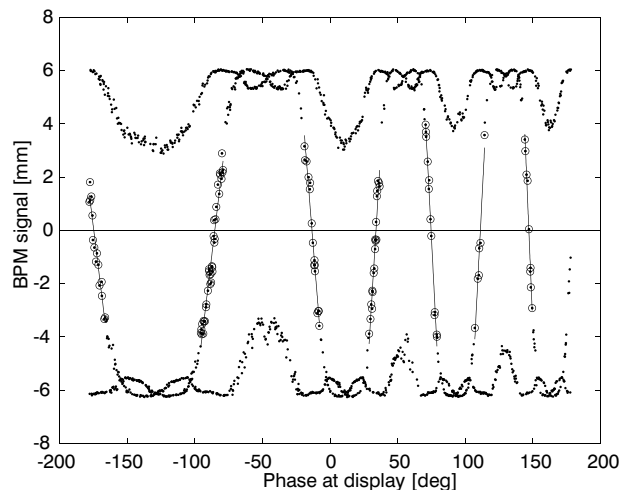


Figure 5.5: Vertical kick vs. RF phase. For several phases of the RF of LOLA the vertical position of the bunch behind the cavity was measured using the beam position monitor BPM 2. To determine the zero-crossings, linear fits are made (solid lines). The data used for these fits are encircled. The other data points should not be trusted. They originate from secondary particles which are produced by kicking the bunch at the vacuum chamber. The zero-crossing data are plotted in Fig. 5.6.

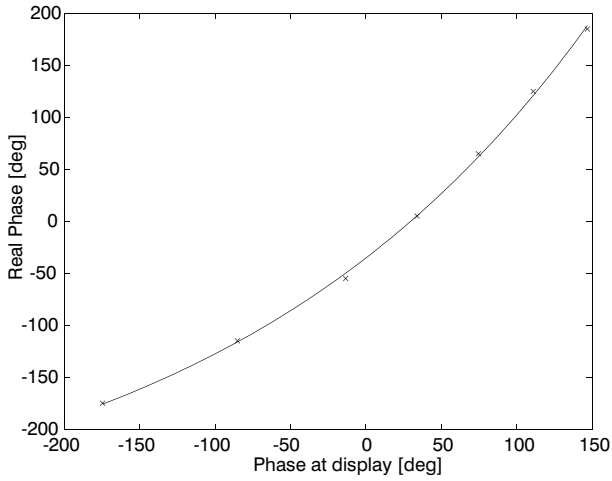


Figure 5.6: Expected zero-crossing distances vs. RF phase at the display on the control panel. The data originate from the zero-crossings of the fit-lines in Fig. 5.5. The correct distances between them should amount to 60 deg. The ordinate is adjusted so that the data points exactly have these distances. The solid line represents an exponential fit (see Eq. (5.6)).

be expected. However, at higher phases these distances become smaller.

Fig. 5.6 reveals the behavior of these distances between the zero-crossings. The data points are the zero-points of the straight lines obtained by linear regressions using the circled points in Fig. 5.5. The abscissa of Fig. 5.6 shows the phase given by the phase shifter display. The scale of the ordinate is adjusted so that the data points have a distance of 60 deg. Many χ^2 -fits were made and an exponential function yielded the best provisional results

$$\varphi_{\text{real}} = 280 \cdot \exp(0.00400 \cdot \varphi_{\text{shifter}}) + \text{offset} . \quad (5.6)$$

This was the first indication that the phase shifter does not work properly. A more precise measurement has been

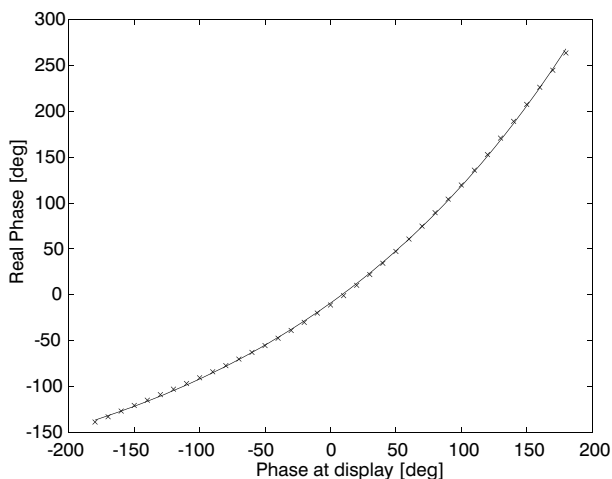


Figure 5.7: Behavior of the phaseshifter measured with a network analyzer. The real phase is plotted vs. the phase the display on the control panel shows. The data are listed in Tab. B.2. The solid line represents an exponential fit (see Eq. (5.7)).

done using a network analyzer. The obtained values are listed in Tab. B.2 and plotted in Fig. 5.7. The fit delivers the function

$$\varphi_{\text{real}} = 236.5 \cdot \exp(0.00431 \cdot \varphi_{\text{shifter}}) - 245.6 . \quad (5.7)$$

This equation is used to set and to measure the correct phase.

5.3 Correlation between the dimensions of OTR screen and CCD camera

When the bunch is imaged at a CCD chip the units of the picture are pixels. The CCD camera produces pictures with a size of 640 pixels vertically and 480 pixels horizontally. The CCD camera needs to be calibrated in order to know the conversion between pixels and millimeters.

For that purpose, the screen holder, to which the screen is mounted, is equipped with calibration marks. To get them into the field of view of the camera, one has to move the screen holder down. Fig. 5.8 shows a resulting photograph. In the upper half one can see four of the calibration marks. These are boreholes with a distance of 5 mm between each other. In the lower half there are two screws with the screen is mounted with. At the bottom of the photograph the screen is visible which has a range from 120 to 330 px.

The field of view is illuminated using a common lamp. The resulting reflections at the edge of the holes are very advantageous. Using a small part of the image containing

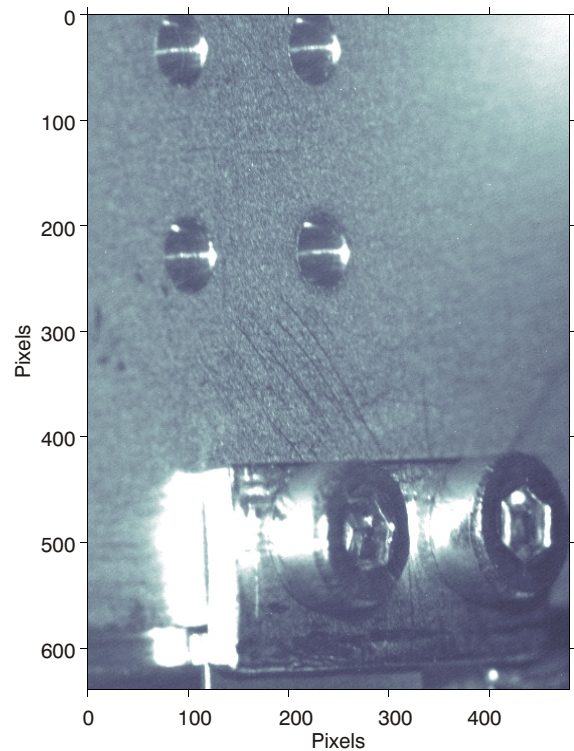


Figure 5.8: A photograph of the screen holder showing the calibration marks. In the upper half there are four boreholes with which the calibration is done. The distance between them amounts to 5 mm. Horizontally the observable distance is shortened by a factor of $\sqrt{2}$ because of a 45 deg tilt with respect to the vertical axis. In the lower part two screen-holding screws and the top margin of the screen itself are visible.

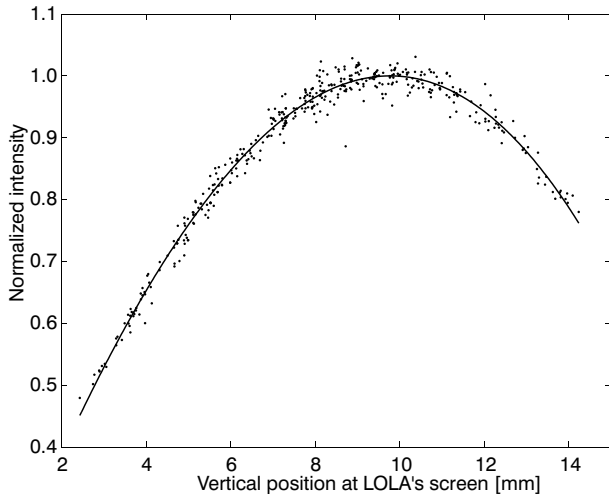


Figure 5.9: Position dependence of the OTR intensity collected with a CCD camera. The data points are acquired by adding up the values of all the CCD pixels of one image. Only images showing the whole bunch are considered. The abscissa shows the centers of mass of the vertical positions. The solid line denotes a third order polynomial fitted to these points. The data are normalized with respect to the maximum of this fit curve.

only two holes, we calculated the vertical or horizontal profile. The two maxima of the profiles denote the positions of the reflections. Their distance give the amount of pixels, that corresponds to 5 mm at the screen.

Attention should be paid to the fact that the screen is tilted horizontally by an angle of 45 deg. Therefore, the observed horizontal distance between the marks is shortened by a factor of $\sqrt{2}$. The results of the measurements are

$$\text{Vertical :} \quad 1 \text{ px} \hat{=} (25.8 \pm 0.2) \mu\text{m} \quad (5.8)$$

$$\text{Horizontal :} \quad 1 \text{ px} \hat{=} (26.8 \pm 0.2) \mu\text{m} . \quad (5.9)$$

The horizontal value is larger than the vertical. This indicates that the tilt may not be exactly 45 deg but 47.1 deg.

5.4 Position dependence of the sensitivity at the OTR station

According to the emission characteristics of transition radiation (see Sec. 5.4.1) its intensity observed with a camera depends on the position of its origin at the OTR screen. The observable vertical size of the screen is about 16 mm. The bunch is streaked only vertically and usually spans the whole screen. Thus the position dependence of the radiation collected by the camera is not negligible in this dimension. Due to the small absolute width of the bunch of about 1-2 mm, the horizontal position dependence of the intensity was not investigated.

Using a weakly streaked and horizontally centered bunch we made a scan where the vertical position of the bunch at the LOLA OTR screen was changed by varying the phase of the RF. First the bunch was streaked in a way that its head was at the bottom and its tail at the top of the image. Then images were taken at several positions at the screen. Second the bunch was flipped by changing the phase of about 180 deg and the procedure was repeated.

The resulting images are two-dimensional matrices with each entry containing a value correlated to the radiation intensity absorbed by the corresponding pixel of the CCD. After subtracting the background image¹ all the entries were added up. The resulting value denotes the intensity which is plotted as a data point in Fig. 5.9 after normalization. The corresponding position was calculated as the center of mass (cm).

If we consider only the error of the normalized intensity that is caused by the noise at the images it would be $\sigma_I = 0.0032$. This is much too small. Caused by charge jitter, beam-losses and various other error sources the error must be at least 5 times larger. To preserve the clarity of the plot, the errors are not shown in Fig. 5.9.

The solid line in Fig. 5.9 results from a fit of a third order polynomial. The data points and the fitted curve are normalized with respect to the maximum of this curve. In this way we can compare them to the theoretical values described below. The normalized polynomial is given by the equation

$$I_{\text{norm}} = -1.49 \cdot 10^{-4} p^3 - 6.90 \cdot 10^{-3} p^2 + 1.78 \cdot 10^{-1} p + 6.19 \cdot 10^{-2} , \quad (5.10)$$

where I_{norm} is the normalized intensity and p the vertical position at the screen in mm.

While the screen spans from 0 mm to 16.6 mm, the diagram shows only data points from 2 mm to 14 mm. The reason is the finite expansion of the spot. To guarantee that we sum over the whole bunch to calculate the intensity, images containing only a part of the bunch are rejected. The marginal values are extrapolated using the obtained fit curve Eq. (5.10).

All images taken after this calibration are corrected by division by this curve. Therefore, the noise at the top and at the bottom of the images is increased (see Fig. 6.1).

5.4.1 Comparison with theoretical values

Transition radiation is emitted when a charged particle traverse two media with different dielectric constants ϵ . The radiation is emitted in forward and backward direction. Ginzburg and Frank predicted this first in 1945 [GF45]. Assuming a perfect vacuum ($\epsilon_1 = 1$) and a perfect reflecting metal surface ($\epsilon_2 = \infty$) the radiated energy per frequency interval of the radiation $d\omega$ and per solid angle $d\Omega$ obeys the following distribution

$$\frac{d^2 W}{d\omega d\Omega} = \frac{e^2}{4\pi^3 \epsilon_0 c} \frac{\beta^2 \sin^2 \vartheta}{(1 - \beta^2 \cos^2 \vartheta)^2} , \quad (5.11)$$

where e is the elementary charge, ϵ_0 the dielectric constant and $\beta = v/c$ with c the velocity of light and v the velocity of the electron. The angle ϑ is defined between the specular reflection of the moving direction of the particle for backward radiation or the continuative trajectory for forward radiation and the direction of view. For particles with ultra relativistic energy ($\beta \approx 1$) even at an angle of incidence of 45 deg the radiation characteristic is rotationally symmetric and the maximum intensity occurs at an angle of

$$\vartheta_{\text{max}} = \frac{1}{\gamma} , \quad (5.12)$$

where γ is the Lorentz factor of the particle. Eq. (5.11) also reveals that there is no dependence on the frequency ω of

¹ Background image - An image without beam that contains the secondary effects originating in the accelerator, e.g. darkcurrent.

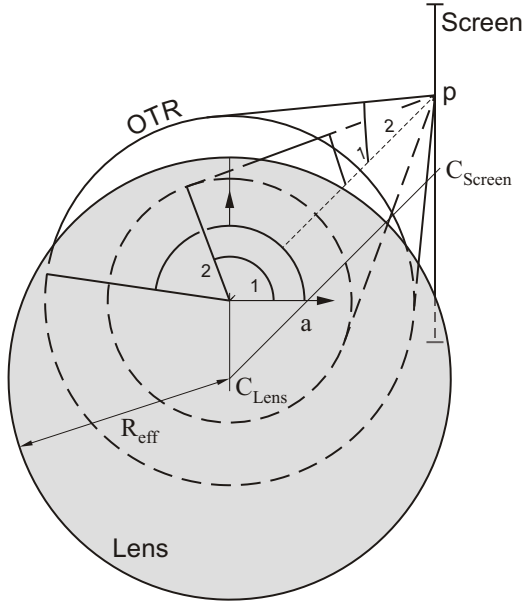


Figure 5.10: Examples for integration of OTR using spherical angles. At the vertical position p at the screen (background) transition radiation originates and enters the lens (front). OTR is axially symmetrical. The figure shows the corresponding angles φ for two different opening angles ϑ . To calculate, how much radiation enters the lens, we have to integrate over the lens and ignore the radiation that passes it. So, at a small angle ϑ_1 we could integrate φ_1 over the whole circle. If the opening angle exceeds a certain limit like ϑ_2 the integration boundaries of φ_2 are determined by the interception point of the lens and the circle of the OTR. So, φ_2 has to be integrated over the dashed circular arc.

the emitted light. Thus there are no corrections necessary if we only consider the optical fraction of the radiation ($\lambda \approx 400 - 800$ nm). For an overview of transition radiation see [Gei99].

A certain fraction of the radiation enters the objective of the camera and is absorbed at the CCD surface. Each pixel delivers a signal proportional to the number of photons it absorbs. The spectral response of the CCD can be neglected for our purpose. The energy distribution of the radiation is given by Eq. (5.11). To calculate the total amount of energy per frequency-interval collected by the camera, we have to integrate over the solid angle $d\Omega = \sin \vartheta d\vartheta d\varphi$.

The integration boundaries for an integration over ϑ and φ are very complicated to define. Fig. 5.10 reveals the difficulties which would arise if we integrated in spherical coordinates: The emission characteristic is axially symmetrical. So, for small ϑ like ϑ_1 we were able to integrate φ_1 over the full circle. But if ϑ exceeded a certain limit like ϑ_2 the circle for φ_2 is cut by the contour of the lens of the objective. The corresponding integration boundaries are, therefore, dependent on ϑ and R_{eff} . In addition, these boundaries are different for each vertical position p of the radiation source. So, we decided to carry out a coordinate transformation.

For that purpose, we have to adapt Eq. (5.11) to the setup of the imaging system. The spherical angles ϑ and φ are transformed to cylindrical coordinates r , α and z which are related to the lens of the objective of the camera (see

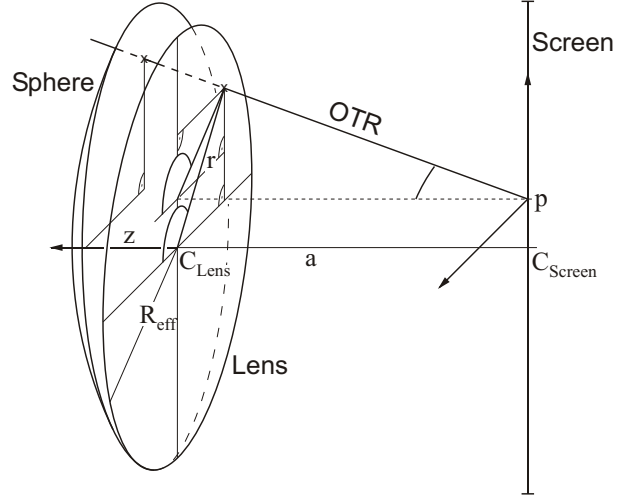


Figure 5.11: Coordinate transformation from spherical to lens-parameters. The optical transition radiation (OTR) originates at the screen at the vertical position p and penetrates first the lens plane and then the sphere. The spherical parameters ϑ and φ are substituted by the new parameters (r, α, z) , which relate to the lens. The penetration point of the sphere determines the z coordinate. The spherical angles are independent of z . Thus the surface of the sphere is projected onto the lens plane. The distance between the center of the lens C_{Lens} and the center of the screen C_{Screen} amounts to $a = 600$ mm. A horizontal offset of the screen to the symmetry axis of the lens is not in the drawing.

Fig. 5.11). The big advantage of this coordinate transformation is that the integration boundaries are well defined. We integrate r from 0 to the effective radius R_{eff} , which is given by the aperture within the objective, and α from 0 to 2π . For every vertical position p the angles ϑ and φ can be expressed by only r and α :

$$\vartheta(r, \alpha, p) = \arcsin \left(\sqrt{\frac{(r \sin \alpha - p)^2 + (r \cos \alpha)^2}{(r \sin \alpha - p)^2 + (r \cos \alpha)^2 + a^2}} \right) \quad (5.13)$$

$$\varphi(r, \alpha, p) = \arcsin \left(\frac{r \sin \alpha - p}{\sqrt{(r \sin \alpha - p)^2 + (r \cos \alpha)^2}} \right), \quad (5.14)$$

where a is the distance between the OTR screen and the lens of the camera and p the vertical position of the radiation source at the screen. In this way we project the surface of the sphere around the radiation source along the OTR rays onto the lens plane. An integration over the whole lens plane has the same result as an integration over the corresponding solid angle.

Now we have to convert the infinitesimal angles $d\vartheta d\varphi$ using the Jacobian determinant $|J|$

$$d\vartheta d\varphi = \left| \frac{\partial(\vartheta(r, \alpha, p), \varphi(r, \alpha, p))}{\partial(r, \alpha)} \right| dr d\alpha = |J(r, \alpha, p)| dr d\alpha. \quad (5.15)$$

So, the whole integral, dependent on the respective vertical

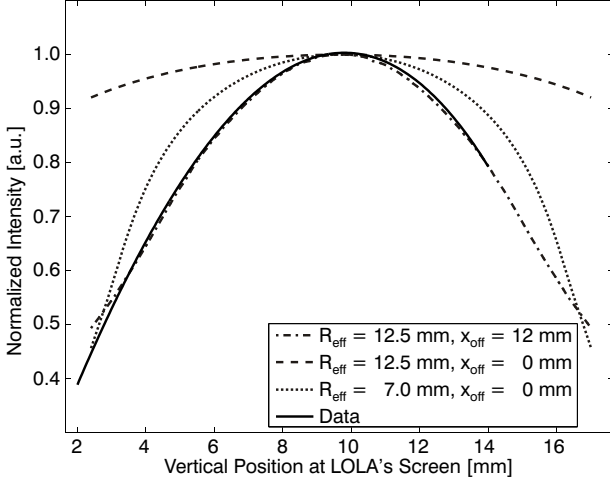


Figure 5.12: Comparison of measured intensity with theoretical predictions. The thick solid line represents the fit to the measured data already shown in Fig. 5.9. The theoretical curves are calculated for several effective lens radii R_{eff} and horizontal offsets x_{off} . Each curve is divided by its own maximum to normalize it and make it comparable. The asymmetry and the fact that the maxima are not located at the middle of the screen, indicate that the lens of the objective and the OTR screen are not parallel to each other.

position p , results in

$$\frac{dW}{d\omega}(p) = \frac{e^2}{4\pi^3 \epsilon_0 c} \int_0^{2\pi} \int_0^{R_{\text{eff}}} \frac{\beta^2 \sin^2 \vartheta(r, \alpha, p)}{(1 - \beta^2 \cos^2 \vartheta(r, \alpha, p))^2} \cdot \sin \vartheta(r, \alpha, p) |J(r, \alpha, p)| dr d\alpha . \quad (5.16)$$

This double integral was only solvable by numerical integration. We used the standard operation `NIntegrate` of `MATHEMATICA5` without any specifications ([Beu05]).

In addition, we considered a horizontal offset x_{off} of the screen to the symmetry axis of the lens. Due to the rotational symmetry of the OTR the vertical position p can easily be substituted by

$$p \longrightarrow \sqrt{p^2 + x_{\text{off}}^2} . \quad (5.17)$$

A comparison of the measured data with the calculated ones is shown in Fig. 5.12. The diagram displays the normalized fit (black solid line) of the measured data as already shown in Fig. 5.9. The other lines represent the normalized theoretical calculations with different assumed effective lens radii R_{eff} and horizontal offsets x_{off} . The real, effective radius of the objective was set to 12.5 mm (see Sec. 3.3). At $R_{\text{eff}} = 12.5$ mm and $x_{\text{off}} = 12$ mm the coincidence between experimental and theoretical curve near their maxima is best; on the fringes they diverge. The asymmetry of the experimental curve and the offset of its maximum (at 9.8 mm) to the middle of the screen (at 8.3 mm) indicate that the camera and the OTR screen are tilted with respect to each other.

5.5 The longitudinal resolution

To reveal the longitudinal properties of a charge distribution, it is streaked vertically and then imaged on an OTR

screen. Depending on the power of the radio frequency (RF) in the cavity the strength of this streak varies. In order to measure the bunch length in femto-seconds, the imaging system needs to be calibrated, and the procedure used is described in this section.

Assuming two particles with a certain distance enter the cavity on the axis of the vacuum chamber one after the other. The phase of the RF the particles experience are different. With a velocity $v \approx c$ and a longitudinal distance d_{long} , the phase difference $\Delta\Phi$ according to the RF frequency f amounts to

$$\Delta\Phi = 2\pi \cdot \frac{d_{\text{long}}}{c} f \hat{=} 360 \text{ deg} \cdot \frac{d_{\text{long}}}{c} f . \quad (5.18)$$

Therefore, the deflecting electric fields the particles experience is different. Fig. 5.13 shows a possible situation. Since the RF of LOLA is a travelling wave with a phase velocity $v_p = c$ (see Ch. 3) the particles experience a constant deflecting force due to the co-propagating electro-magnetic field. When the two particles arrive at the OTR screen they have a vertical distance that is proportional to their longitudinal distance. This is only valid if the particles are located within the linear range of the sine, but in the normal operation mode of LOLA this can be assumed.

To calibrate the correlation between the vertical position on the screen and the longitudinal position within the bunch, the phase dependent deflection of the bunches is measured. By changing the phase of the RF the bunch moves over the screen. At several phases 10 images were taken. Then the vertical profile of each image (see Fig. 6.1) was calculated. The maxima of the profiles were used as a secure reference for the position variation at the screen.

Fig. 5.14 shows the result of this calibration. The vertical position in pixels of the CCD camera is plotted vs. the phase of the RF in degrees. Each data point is the mean of 10 values resulting from 10 images which were taken per phase. The corresponding standard deviations are shown as error bars. The solid line denotes a linear fit yielding to the equation

$$p = (73.7 \pm 3.9) \frac{\text{px}}{\text{deg}} \cdot \Phi + (544 \pm 13) \text{ px} , \quad (5.19)$$

where p is the position at the screen and Φ the phase of the RF. Using Eq. (5.18) and Eq. (5.19) we are able to calculate the resolution r

$$r = \frac{1}{(73.7 \pm 3.9) \text{ px/deg}} \cdot \frac{1}{360 \text{ deg} f} = (13.20 \pm 0.70) \frac{\text{fs}}{\text{px}} , \quad (5.20)$$

where f is the frequency of the RF. Depending on the given problem it may be more advantageous to consider the arrival time or the longitudinal position within the bunch. For the conversion the values can be multiplied with the velocity of the particles which usually is c .

Of course, the calibration given by Eq. (5.20) corresponds to a certain RF power. We have to qualify the power while this calibration was made, to calculate the resolution at arbitrary power. For that purpose, we took another series of measurements beforehand.

First we increased the setpoint on the control panel so that the power display showed 15.8 MW. We know from the power calibration described in Sec. 5.1 that this is also the real power. Then we connected a reference signal of the RF of LOLA with an oscilloscope. In this connection we installed a couple of attenuators so that the signal at the scope was in a suitable range. Then we decreased the

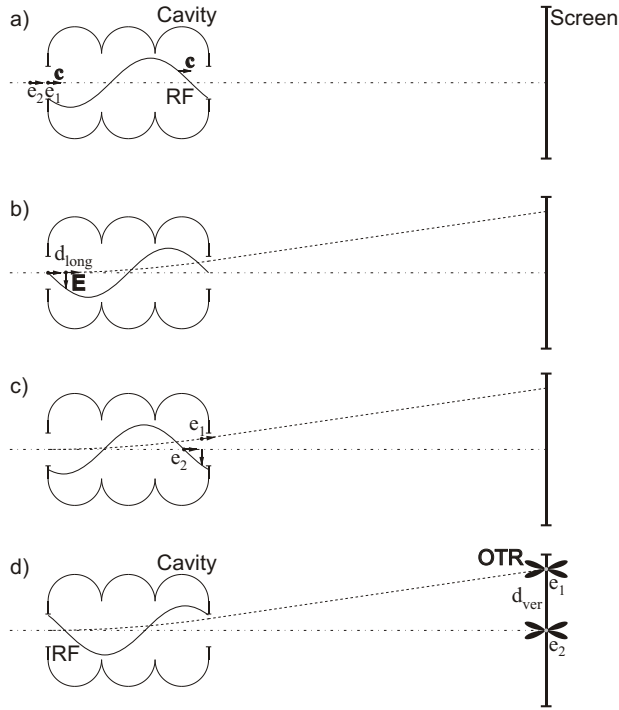


Figure 5.13: Principle of resolution calibration. a) Two electrons e_1 and e_2 enter the cavity on axis (dashdotted line). Their and the RF's phase velocity are equal to the velocity of light c . The wavelength of the RF spans three cells of the cavity. b) The longitudinal distance d_{long} between the particles determines the phase difference with respect to the RF and thus the difference of the electric field \mathbf{E} . c) In this example the electric field that e_1 experiences is negative. Therefore, the deflection occurs upward. e_2 enters the cavity at a zero-crossing and undergoes no deflection. d) After the electrons have left the cavity, the motion is straight. They strike the screen with a vertical distance d_{ver} and produce optical transition radiation (OTR), that is imaged with a CCD camera. So, the vertical distance at the screen is correlated with the longitudinal distance.

attenuation by removing one of the attenuators. Therefore, the signal at the scope increased. We decreased the reference signal by readjusting the setpoint of the power of the RF so that the scope showed the same level as before. Tab. B.3 lists the iterations. The amount of the attenuation is well known. Thus we are able to calculate the power of the RF at the different setpoints.

For the calibration described above we chose the setpoint at 0.848. The attenuation amounted to 15.826 dB. The measurement started at a power of 15.8 MW and an attenuation of 26.066 dB. Thus the power P_{ref} we used for the resolution calibration and as reference power in Eq. (5.22) amounts to

$$P_{\text{ref}} = 15.8 \text{ MW} \cdot 10^{(15.826 - 26.066) \text{ dB} / 10} = 1.50 \text{ MW} . \quad (5.21)$$

Now we are able to calculate the resolution at arbitrary RF power. We know that the acceleration of a charged particle within an electric field is proportional to the voltage V . The corresponding power P is proportional to V^2 . Thus the resolution r at an arbitrary power P is calculated

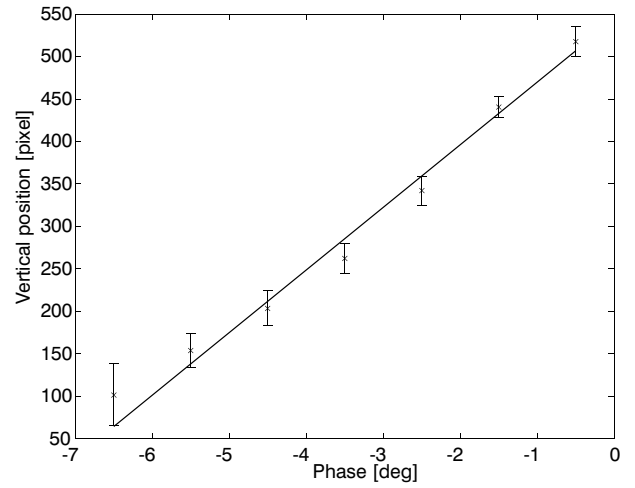


Figure 5.14: Dependence of the RF phase on the vertical position of the electron beam at the screen of LOLA. The data are the means of the maxima of the longitudinal bunch profiles. The errorbars denote the corresponding standard deviations. The solid line denotes a linear fit according to Eq. (5.19). By changing the phase of the RF the bunch travels vertically over the screen.

by

$$r = r_{\text{ref}} \cdot \sqrt{\frac{P_{\text{ref}}}{P}} , \quad (5.22)$$

where r_{ref} is the reference resolution originating from Eq. (5.20).

The maximum input power of the cavity, amounts to $P_{\text{max}} = 18 \text{ MW}$. The corresponding maximum resolution, achievable with LOLA, is $r_{\text{max}} = 3.81 \text{ fs/px}$.

The measured intensity distribution is a convolution of the streaked longitudinal and the vertical beam distribution. Assuming a Gaussian beam distribution in both the y and l direction, where y and l are the vertical and longitudinal coordinates, respectively, the measured beam size σ_{meas} can be expressed by

$$\sigma_{\text{meas}}^2 = \sigma_{\text{vert}}^2 + \sigma_{\text{long}}^2 . \quad (5.23)$$

Here σ_{vert} is the vertical and σ_{long} the longitudinal rms beam size.

To minimize the influence of the transverse profile, the bunch can be focused at the screen using the quadrupole 2 in front of LOLA (see Fig. 3.1). Considering the whole bunch, the design values for the vertical beta function β at the position of the screen and the vertical, normalized emittance ε^n are [Gol05]

$$\begin{aligned} \beta &= 73.7 \text{ m} \\ \varepsilon^n &= 2 \pi \cdot \text{mm} \cdot \text{mrad} . \end{aligned} \quad (5.24)$$

With an energy of the bunch of 445 MeV, the vertical focussing function K of the quadrupole and the theoretical, vertical bunch width σ_{vert} amount to

$$\begin{aligned} K &= -1.19 \text{ m}^{-2} \\ \sigma_{\text{vert}} &= 412 \text{ } \mu\text{m} . \end{aligned} \quad (5.25)$$

According to Eq. (2.23), the vertical beam width can be minimized by minimizing the beta function. This means,

the optimum focusing function of the quadrupole has to be found. The optimum values are

$$\begin{aligned}\beta_{\text{opt}} &= 5.62 \text{ m} \\ K_{\text{opt}} &= -1.09 \text{ m}^{-2} \\ \sigma_{\text{vert,opt}} &= 114 \text{ } \mu\text{m} .\end{aligned}\tag{5.26}$$

To reduce the measuring errors, the beam optic should be changed in this way. But this is in conflict with the normal operation of the FEL.

In the upper estimation, the emittance is assumed as constant. Due to disturbing effects as for example wake fields, the emittance increases along the accelerator and depends on the beam optics. The vertical beam width is dependent on the vertical emittance (see Eq. (2.23)). Therefore, the error in the measurements of the longitudinal bunch shape increases with increasing emittance.

Assuming a vertical beam size as given in Eq. (5.26), the corresponding unstreaked bunch width will span $114 \text{ } \mu\text{m}/(25.8 \text{ } \mu\text{m}/\text{px}) = 4.42 \text{ px}$ of the CCD. Therefore, the spike has to have at maximum streak a longitudinal length of at least 4.42 px. The measured bunch width will then be

$$\sigma_{\text{meas}} = \sqrt{\sigma_{\text{vert}}^2 + \sigma_{\text{long}}^2} = \sqrt{2} \cdot 4.42 \text{ px} = 6.25 \text{ px} .\tag{5.27}$$

This means, that the spike length has to be at least

$$\sigma_{\text{long}} = 4.42 \text{ px} \cdot 3.81 \frac{\text{fs}}{\text{px}} = 16.8 \text{ fs} ,\tag{5.28}$$

to be resolvable. This is the maximum, theoretical resolution of the spike length obtainable with LOLA.

6 Measurements

6.1 Longitudinal charge distribution

In this section, the measurement of the longitudinal charge distribution is presented, by means of a measurements with different RF input power at LOLA, resulting in different streaks of the bunch. The general procedure of evaluation of data obtained with LOLA is also discussed.

At the considered measurement the beam energy at LOLA amounted to 445 MeV. The charge of the bunches was up to 0.87 nC. The phase of ACC1 was set to -7.8 deg off-crest, the phase of ACC2/3 to an unknown value.

Fig. 6.1 shows images (upper part) of the streaked bunch at different RF power in LOLA. The images show the color-coded intensity on the OTR screen as measured with the CCD (see Sec. 3.3). The colorbar at the right of Fig. 6.1 denotes this color-code.

As discussed in Sec. 5.4, the sensitivity of the optical setup depends on the vertical position of the origin of the radiation. Therefore, the images are corrected using Eq. (5.10). A side-effect of this correction is an increased noise towards the top and the bottom of the image.

The vertical axis shows the longitudinal coordinate of the bunch in units of pico-seconds. With increasing power, the streak increases and the scale of this axis is stretched. The horizontal axis denotes the millimeters at the screen of LOLA. The total horizontal size of the images taken with the camera of LOLA amounts to 12.9 mm. Because of the small width of the electron bunch it is possible to select a region of interest which is considerably narrower than the screen width. This reduces the noise of the vertical profiles.

The vertical profiles are presented in the lower part of Fig. 6.1 (solid lines). A profile is the sum of the intensities. In this figure they are normalized to the maximum height of the left profile.

The profiles are used to measure the vertical width of the spike at the OTR screen. One possibility is to fit a Gaussian curve (thick, dashed lines) into the head region. Then the width of the Gaussian denotes the width of the spike. At some measurements the shape of the bunch fails a Gaussian fit. For example at the measurements presented in the next section, the bunch exhibits a double-spike structure (see Fig. 6.4). In such cases, the FWHM¹ is measured. The arrows in Fig. 6.1 denote the FWHMs of the presented profiles.

In Fig. 6.2 the averages of the Gaussian widths and the FWHMs are shown, which result from the evaluation of 10 images at each setpoint of power. The corresponding standard deviations are represented as errorbars. The data points are connected for clearness reasons. The vertical axis shows femto-seconds, according to the calibration presented in Sec. 5.5. The width of the spike gets smaller with increasing power and seems to saturate.

This behavior is a result of the convolution of the longitudinal and the transverse profile. In case of Gaussian distributions, the measured spot-size is given by Eq. (5.23). At small streaks, the transverse size of the spike dominates the spot-size measured on the screen. Its contribution converted into femto-seconds is large at small streaks and de-

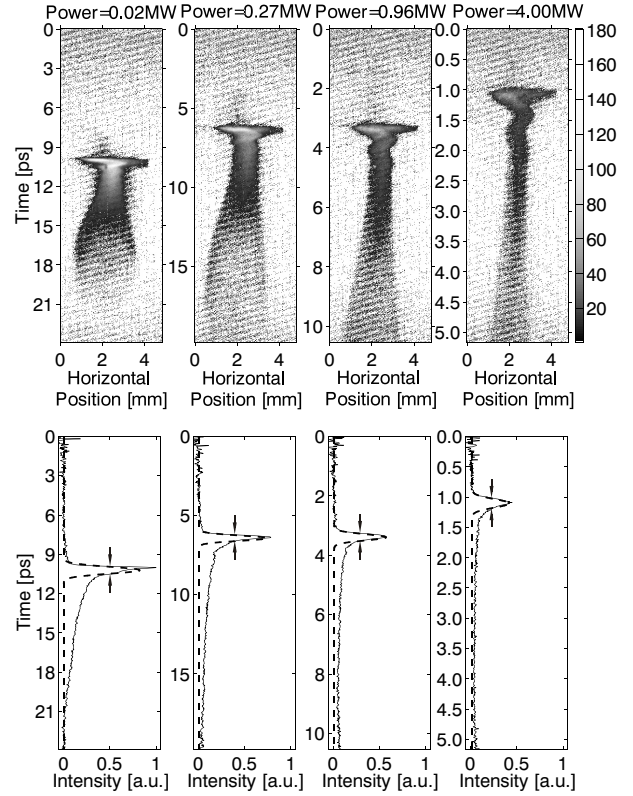


Figure 6.1: Bunch shape and longitudinal profiles at different RF power. The upper part shows images taken with the camera of LOLA at different RF input power. The streak increases from left to right. The lower part shows the longitudinal profiles (solid lines) of the upper images. The height of the profiles is normalized to the height of the left one. The dashed lines represent fits of a Gaussian curve. The arrows denote the FWHM of the spike.

creases with increasing RF power. Therefore, the values in Fig. 6.2 approaches to the correct longitudinal spike length.

The Fig. 6.3 shows the measured width of the spike taken from the same set of data as Fig. 6.2. The vertical axis shows μm at the screen. The deflecting voltage of the RF at the horizontal axis is calculated using Eq. (2.73). The dash-dotted lines in the figure belong to the values of the FWHM and the dashed lines to the Gaussian widths. The thick lines represent fits using the equation

$$\sigma_{\text{meas}} = \sqrt{\sigma_{\text{vert}}^2 + (\sigma'_{\text{long}} \cdot V_{\text{RF}})^2}. \quad (6.1)$$

This equation results from Eq. (5.23) considering the linear dependence of the longitudinal spike width at the screen σ'_{long} from the deflecting voltage V_{RF} . This dependence is suggested by the linear increase. The vertical spike width σ_{vert} is constant and is represented by the straight, horizontal lines. The intersection point is at a voltage of 9.3 MV. Here the vertical and the longitudinal spike widths are equal.

¹ FWHM - Full Width Half Maximum

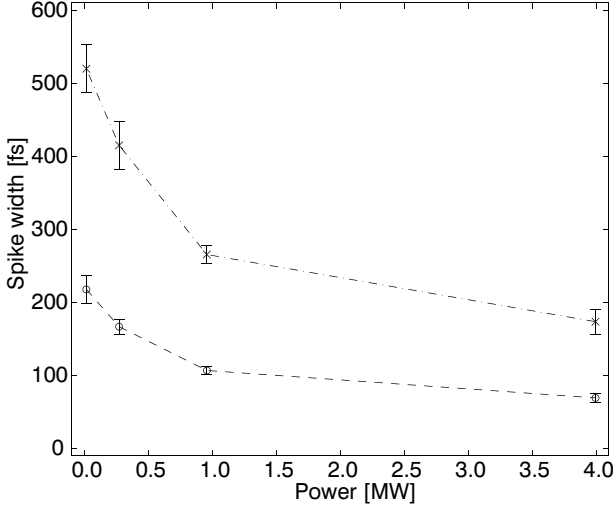


Figure 6.2: Spike width in fs vs. RF power. The “x” represent the FWHMs and the “o” the Gaussian widths. The standard deviation is shown as errorbars. The points are connected to guide the eye.

The absolute longitudinal spike width σ_{long} can be calculated by

$$\sigma_{\text{long}} = \sigma'_{\text{long}} \cdot C, \quad (6.2)$$

where C is a constant obtained in the following way: The dependence of the streak on the power is given by Eq. (5.22). The reference resolution r_{ref} is divided by the calibration constant of Eq. (5.8). In addition, we convert the reference power P_{ref} into deflecting voltage using Eq. (2.73) and get

$$\begin{aligned} C &= 13.20 \frac{\text{fs}}{\text{px}} \cdot \frac{1}{25.8 \mu\text{m}/\text{px}} \cdot 1.6 \text{ MV} \cdot 3.64 \cdot \sqrt{1.50} \\ &= 3.65 \frac{\text{MV} \cdot \text{fs}}{\mu\text{m}}. \end{aligned} \quad (6.3)$$

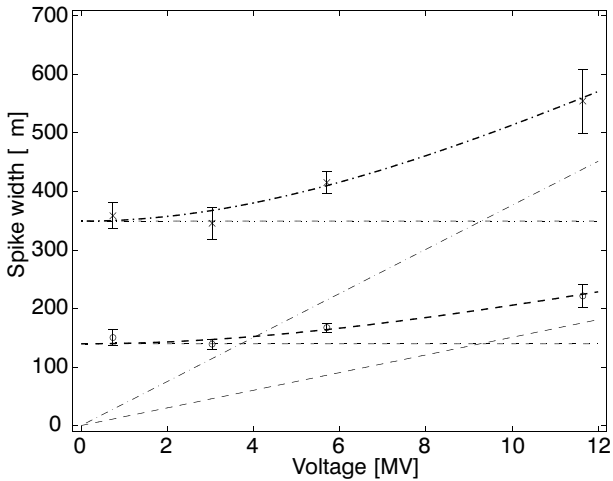


Figure 6.3: Spike width in μm at the screen vs. deflecting voltage. The “x” represent the FWHMs and the “o” the Gaussian widths. The standard deviations are shown as errorbars. The thick lines represent fits using Eq. (6.1). The thin lines are results of the fits and represent the vertical (horizontal line) and the longitudinal spike width (increasing line).

The resulting longitudinal spike width is then

$$\text{FWHM: } \sigma_{\text{long}} = (137 \pm 14) \text{ fs} \quad (6.4)$$

$$\text{Gaussian width: } \sigma_{\text{long}} = (55.0 \pm 5.5) \text{ fs} . \quad (6.5)$$

In Sec. 2.2.1 we calculated an bunch length of 26 fs with an energy spread of 5 keV (see Eq. (2.49)). We measured a Gaussian width of 55 fs. This discrepancy may be due to a larger energy spread than assumed or CSR effects which are not considered in the estimation.

The corresponding vertical spike width amounts to

$$\text{FWHM: } \sigma_{\text{vert}} = (349 \pm 35) \mu\text{m} \quad (6.6)$$

$$\text{Gaussian width: } \sigma_{\text{vert}} = (139 \pm 14) \mu\text{m} . \quad (6.7)$$

The errors result from the data value with the largest standard deviation which is about 10% of the mean value. The errors of the fit parameters should be smaller.

The considerations shown here can be expanded and be automatized by doing a tomographic reconstruction. This is foreseen for the near future.

6.2 ACC1 phase scan

As mentioned in Sec. 2.2 the compression of the bunch depends on its energy chirp. Dependent on the phase of the RF, the slope of the energy chirp changes. This results in a different compression of the bunch. In this section the longitudinal bunch shape and the bunch length as a function of the RF phase of ACC1 is studied.

6.2.1 Data analysis

The off-crest phase ϕ_0 of the RF of the first acceleration module ACC1, upstream of the bunch compressors, was changed from -2.0 deg to -13.5 deg in steps of 0.5 deg. At each step, 10 images were taken. The average background was subtracted and the vertical position dependence of the OTR was corrected, according to the correction function described in Sec. 5.4. In Fig. 6.4 the resulting longitudinal charge distributions and the corresponding profiles at off-crest phases of -6.5 deg to -13.5 deg are shown. The profiles are normalized with respect to their maximum. The compression of the bunch increases with decreasing ϕ_0 . In the range from -2.0 deg to -6.5 deg no spike is visible. The evaluation of these images was, therefore, not reasonable and was omitted.

The spike length was obtained by measuring the full width of the half maximum (FWHM). The dashed lines in the image at $\phi_0 = -7.0$ deg illustrate this. At larger compression phases a double spike has formed. The measured value for the bunch length spans both spikes as illustrated in the last image of Fig. 6.4.

In Fig. 6.5 the average of the bunch lengths is plotted as a function of ϕ_0 . The corresponding standard deviations are shown as errorbars.

6.2.2 Comparison with simulations

There are two simulations which predict the bunch length and bunch shape in the VUV-FEL, done by [Kim05] (for input-files and results see [Kim05a]) and [Doh05]. For the simulation from the gun up to the beginning of the first bunch compressor (BC2), both use the *ASTRA*²-code. Additionally, the wakefields arising in ACC1 were taken into account by [Doh05].

ASTRA [Flo00] computes the development of electron bunches, considering space-charge effects. Especially at low energies, this effect influences the bunch remarkably.

ASTRA solves the equations of motion numerically, beginning with the production of the electrons within the photocathode gun. According to the given profile of the laser producing the electrons, the resulting charge distribution has a certain shape. The electric and magnetic fields and the resulting forces at this electron bunch are computed for each time-step in a grid (PIC³-code).

Coherent synchrotron radiation (CSR) is difficult to simulate. *ASTRA* is not able to calculate CSR effects. The further calculation made by [Kim05] is based on *ELEGANT* (for software and documentations see [Bor05]) and is done up to LOLA. The simulation of [Doh05] was done via *CSRTrack* (see [Doh04], [Doh00], [Doh03]) for the calculation within the bunch compressors. For the development of the charge distribution between the bunch compressors, including the accelerator modules ACC2 and ACC3, transfer-matrices considering wakefields were used.

² *ASTRA* - A space-charge tracking algorithm.

³ PIC - Particle in-cell.

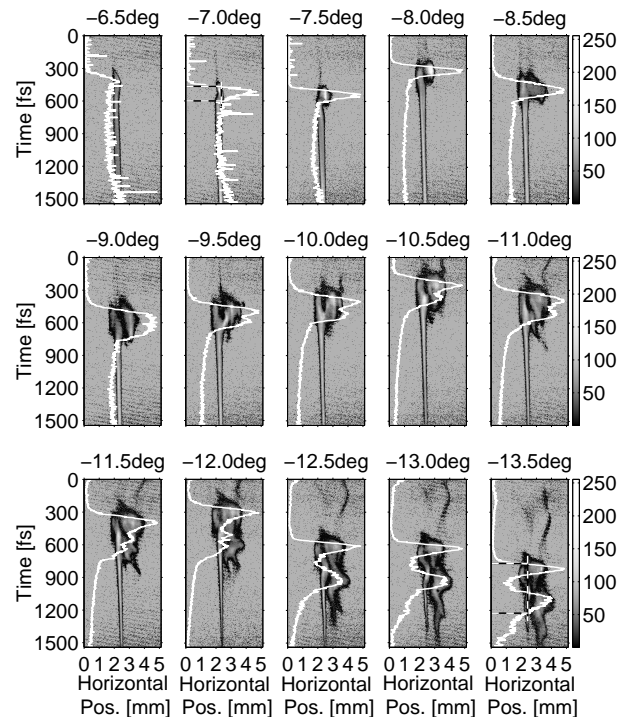


Figure 6.4: Beam images and longitudinal profiles at different compressions. The ACC1 phase offset increases from the left to the right and from the top to the bottom. The corresponding off-crest phase ϕ_0 is given in the title of each image. The vertical axes show the longitudinal dimension in femtoseconds. The horizontal axes denote the horizontal position at the screen of LOLA. Since a spike is not visible until $\phi_0 = -7.0$ deg the corresponding measurements are not evaluated.

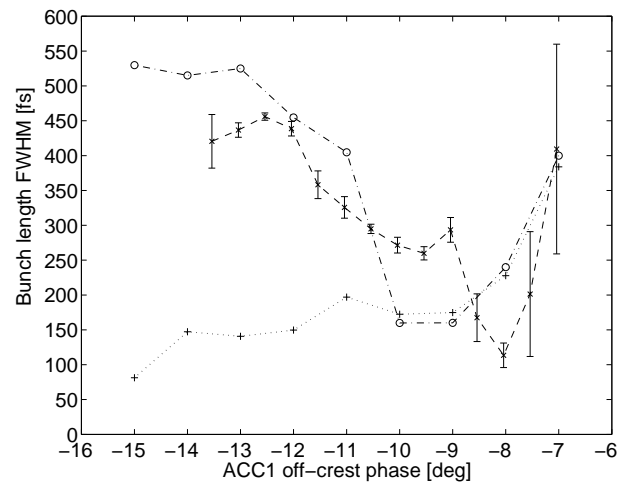


Figure 6.5: The bunch length at different compressions. The FWHM in femtoseconds of the longitudinal profiles (Fig. 6.4) are plotted vs. the RF phase of ACC1 with respect to on-crest. The “x” denote the mean of 10 measurements. The errorbars show the corresponding standard deviations. The “+” originate from the simulation [Kim05] and the “o” from the simulation [Doh05]. The data points are connected to guide the eye.

After the second bunch compressor (BC3) the calculation was stopped. So, the whole path up to LOLA including the

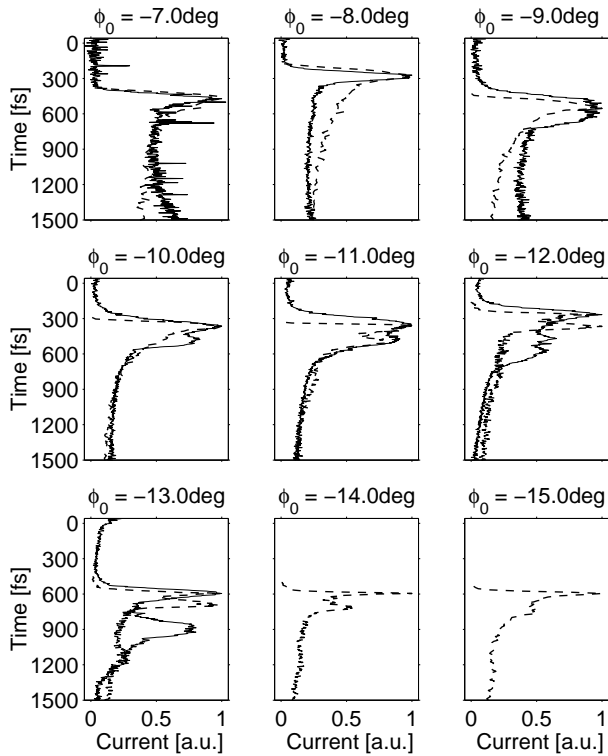


Figure 6.6: Comparison of measured and theoretical longitudinal profiles of [Kim05]. The head of the bunch is at earlier time region. The dashed lines denote the simulation. The solid lines originate from Fig. 6.4. The maxima of the profiles are normalized by their maximum.

last accelerator modules ACC4 and ACC5 was excluded. In both calculations the phase of ACC2 and ACC3 was set to on-crest, so that an additional shaping of the energy distribution is not expected.

An important issue, not considered by the simulations after ACC1, is the effect of interaction of the electrons caused by space-charge. In the used simulation codes this feature is not implemented. At high energies space-charge effects are negligible for the transverse properties of the bunch but they influence it longitudinally.

The Fig. 6.6 compares directly the profiles of the simulation [Kim05] with the profiles, obtained by the measurement. The measured profiles are also shown in Fig. 6.4. At small compressions, meaning at higher off-crest phases, the shape obtained by the simulation (dashed lines) and by the measurement (solid lines) agree. At $\phi_0 = -10.0$ deg, a second spike is visible. In the simulation the second spike grows out of the tail with decreasing phase at a nearly constant distance of about 100 fs with respect to the first one. In the measurement, the spike splits up into two spikes. The second one departs from the leading spike so that the bunch length increases with decreasing off-crest phase. This tendency does not agree with this simulation. As also shown in Fig. 6.5 the bunch lengths disagree at $\phi_0 < -10.0$ deg.

The comparison with the other simulation [Doh05] is shown in Fig. 6.7. In agreement with Fig. 6.6, the second spike grows out of the tail starting at $\phi_0 = -10.0$ deg. But the distance to the leading spike (top) is about 300 fs. Therefore, the bunch length is in good agreement with the measurement at higher compressions at $\phi_0 < -11.0$ deg

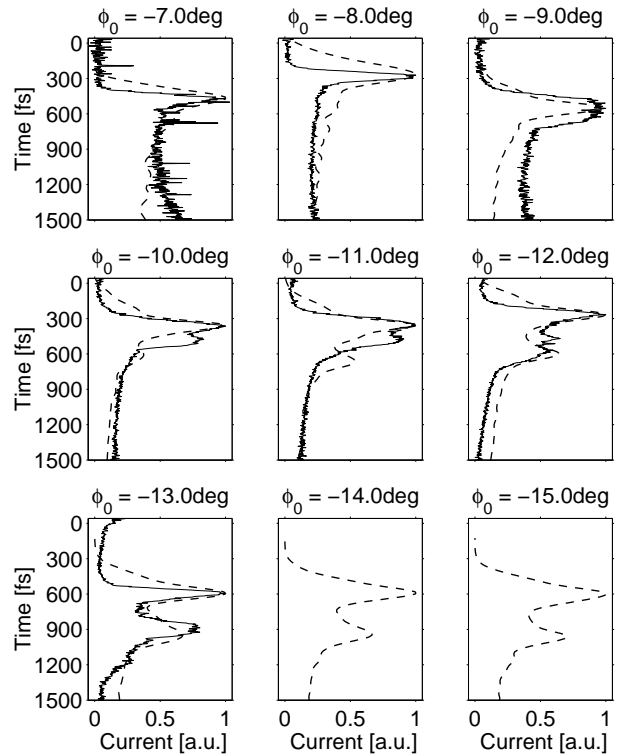


Figure 6.7: Comparison of measured and theoretical longitudinal profiles of [Doh05]. The head of the bunch is at earlier time region. The dashed lines denote the simulation. The solid lines originate from Fig. 6.4. The maxima of the profiles are normalized by their maximum.

(see Fig. 6.5). The tendency of the measured bunch length, to decrease first and then to increase with increasing phase offset, is in agreement with this simulation.

Another difference between the simulations is the slope of the leading head region of the bunch. In Fig. 6.7 the slope increases more gently. This disagrees with the LOLA measurements. The simulated profiles may be smoothed to much. Additionally, it is to mention that in Fig. 6.6 the second spike vanishes at $\phi_0 \leq -15.0$ deg, while it persists in the other simulation.

6.2.3 Discussion of the results

During the evaluation of the measured data, it turned out, that unfortunately the RF of ACC2 and ACC3 was not set to the on-crest phase. This means that the longitudinal phase-space of the beam was impressed additionally with an energy modulation within these acceleration modules. Therefore, the shape of the bunch obtained in the simulations does not precisely reflect the situation during the measurement.

Fig. 6.4 reveals some interesting properties of the bunch: After a spike has formed at the first time at an off-crest phase of -7.0 deg in ACC1, it gets narrower and higher up to $\phi_0 = -8.0$ deg, with respect to the tail. The bright spot in the head denotes a high charge-density (refer to the colorbar). Here the bunch length is minimal and amounts to (114 ± 18) fs at FWHM. In comparison to the simulations, this minimum bunch length occurs at a higher off-crest phase. Probably, this is an effect of the additional energy modulation caused in ACC2 and ACC3. This modulation

could cause an over-compression. The result would be, that this single spike gets wider and loses height, as visible up to -9.0 deg.

At $\phi_0 = -9.5$ deg, we see a double spike in the profile at the first time. The pictures suggest, that the second spike seems to accumulate charges of the tail. In addition, the spike gets more and more narrow while its charge-density increases. Due to the increasing energy chirp produced in ACC1, the tail gets shorter up to $\phi_0 = -12.5$ deg. The distance of the two spikes increases, therefore, the FWHM increases. At this phase the length of the spike in the head of the bunch is maximal and amounts to (456 ± 5) fs. We know from a measurement at BC2, that at a phase of $\phi_0 = -13.0$ deg with respect to on-crest, the bunch is fully compressed. At smaller off-crest phases the head of the bunch experiences an over-compression. Therefore, the structure in the head of the bunch smears out.

At phases $\phi_0 < -11.0$ deg the compression in BC2 increases further. Therefore, coherent synchrotron radiation, arising in the magnetic chicane, becomes the dominant effect for bunch length expansion. The bunch length calculated by *ELEGANT* is half as long as the measured one. This may be due to underestimation of CSR effects. The strength of CSR fields in the *ELEGANT* simulations can be increased by using a larger number of bins, which indicates that it is underestimated in the present simulation [Kim05].

At phases $\phi_0 > -9.0$ deg, the shape of the measured profiles, in particular the rising edge at the head of the bunch, are better agreed with the simulation done by [Kim05]. At these small compressions, the CSR effects are small. So, the reason for the difference between the simulations has to be searched in the upstream part of the accelerator. Since both simulations used the same *ASTRA* input-file to calculate the initial charge distribution in the gun, the only difference is the addition of the wakefields by [Doh05]. An overestimation of the wakefields is possible.

6.3 Emittance of the spike

As already shown in the previous chapters, the TTF produces a bunch with a longitudinal structure consisting of mainly two parts: A very short intense spike and a long, less-intense tail. Due to its importance for the SASE process, the emittance of the spike is a quantity of interest.

In general, with OTR screens, one can only analyze the transverse properties of the whole bunch [Loe05], because the spike and its tail can not be separated. The longitudinally distributed electrons hit the screen back-to-back and the camera integrates all the transition radiation, so that the information of the longitudinal position of each particle gets lost.

But with LOLA a separation of the spike from its halo is possible. With little RF power in the transverse deflecting cavity, the streak is not large enough to reveal the longitudinal profile of the spike, but sufficient to do the desired separation (see Fig. 6.8).

6.3.1 Considerations on the experimental setup

The section around LOLA, relevant for the measurement of the emittance, consists of many elements, as shown in Fig. 3.1. These elements have different influences on the beam, which can disturb our measurement.

The steerers are dipole magnets. They change the orbit of the incoming electrons by a certain angle. The angles of the particles with respect to each other remain constant. Thus also their transverse distances at the OTR screen are not affected in first order. Because we are only interested in these distances, the correction magnets can be considered as drift-spaces.

In the cavity the bunch is streaked. This means, that the electrons with the same longitudinal displacement l experience the same electro-magnetic field. Such a region is called a slice. Each electron of a slice undergoes thus the same change of its angle. Their transverse distances are not affected. Therefore, we can consider LOLA as a drift-space, too, as far as beam optics are concerned.

With these simplifications, the relevant lattice consists of only five elements:

1. The horizontally de-focussing quadrupole 2
2. Drift-space
3. The horizontally focussing quadrupole 3
4. Drift-space
5. The off-axis OTR screen of LOLA

The transfer-matrix \mathbf{R} (see Sec. 2.1.1) from quadrupole 2 up to the screen of LOLA, can be calculated by multiplying the transfer-matrices of each element,

$$\mathbf{R} = \mathbf{R}_{L2} \cdot \mathbf{R}_F \cdot \mathbf{R}_{L1} \cdot \mathbf{R}_D, \quad (6.8)$$

where \mathbf{R}_{L1} denotes the transfer-matrix of the first drift-space with the length L_1 , \mathbf{R}_{L2} of the second drift-space with length L_2 , \mathbf{R}_D of the horizontally de-focussing quadrupole and \mathbf{R}_F of the horizontally focussing quadrupole.

To estimate the emittance of the spike, we use the first row of Eq. (2.18), transform it and get, using Eq. (2.23),

$$\sigma_{\text{rms}} = \sqrt{\frac{\varepsilon}{\pi} (R_{11}^2 \beta_0 - 2R_{11}R_{12}\alpha_0 + R_{12}^2 \gamma_0)}. \quad (6.9)$$

The width of the spike at the OTR screen is measured (see description below). Since $\beta\gamma - \alpha^2 = 1$, Eq. (6.9) contains three unknown parameters ($\beta_0, \alpha_0, \varepsilon$). Therefore, we have to measure σ_{rms} for at least three different conditions.

In our case, eleven different conditions were generated by changing the current of the quadrupole 2 (Fig. 3.1) in front of LOLA. In this way, we changed the strength of this magnet and thus the transfer-matrix up to the screen. Fig. 6.8 shows some examples of bunches at different currents of the quadrupole.

6.3.2 Data analysis

Fig. 6.8 shows amongst others the profiles of the corresponding bunch. At the longitudinal profile (vertical axis), the spike is visible. In the pictures themselves, the spike is visible as a spot with high intensity (refer to the colorbar). To this peak, we fitted a Gaussian by using the χ^2 -method. An algorithm found out, how many data points of the longitudinal profile had to be used for this fit, by looking for the fit with the smallest χ^2 . Then the whole image was cut horizontally at the last data point of the used longitudinal profile. The white, dashed line in Fig. 6.8 f) illustrates, where this cut was made. Then also a Gaussian was fitted into the horizontal profile of the remaining image. In this way, we ensured, that we use the same region of the bunch for both the horizontal and vertical fit.

At eleven different currents of the quadrupole 2, ten images were taken. The mean of the resulting widths of the Gaussians versus quadrupole current and the standard deviations as errorbars are plotted in Fig. 6.9. With Eq. (6.9), the corresponding Twiss parameters β_0 , α_0 and the emittance ε were found by using the χ^2 -methode. The solid lines in Fig. 6.9 show the resulting curves. The correspond-

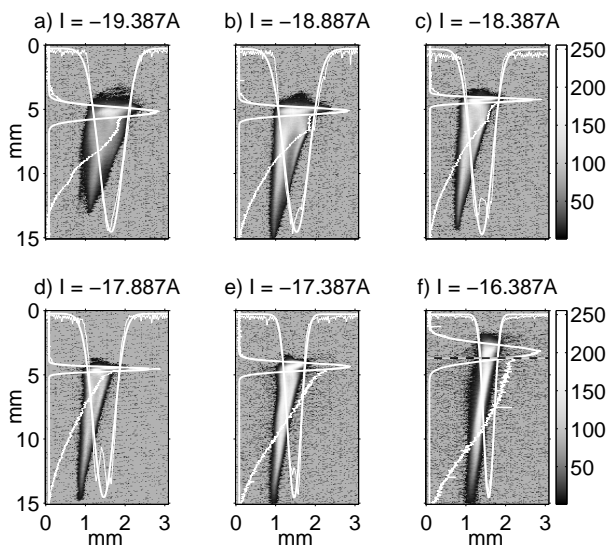


Figure 6.8: Examples of little streaked bunches at different currents I of the quadrupole. The colorbars give the correlation between the color and the intensity of the transition radiation. The thin lines denote the longitudinal and horizontal profiles. The thick lines are the fitted Gaussians. The widths of these Gaussians are plotted in Fig. 6.9. In part f), the dashed line denotes, where the cut of this image was made. Only the part of the image above this line was used for fitting. The units of the axes are millimeters at the OTR screen.

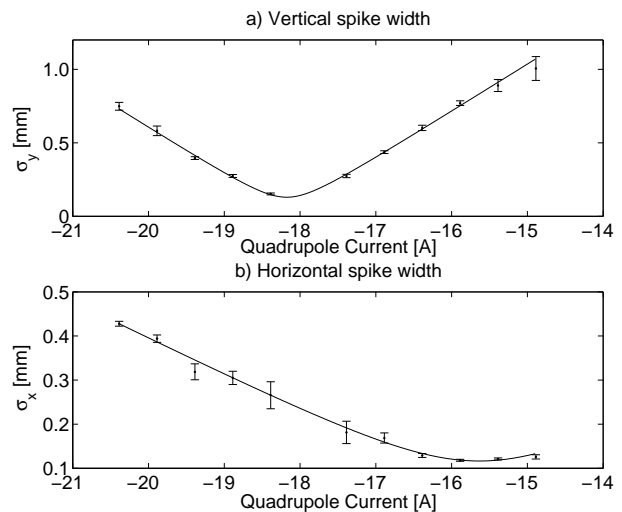


Figure 6.9: Spike width in horizontal and vertical direction vs. quadrupole current I . Each data point is the mean of 10 values. The corresponding standard deviations are presented as errorbars. The solid lines result from Eq. (6.9) and the beam-parameters acquired by a χ^2 -fit. These parameters are given in Tab. 6.1.

Vertical	
β_0 (m)	172.99 ± 0.11
α_0 (1)	57.296 ± 0.035
γ_0 (m^{-1})	18.983 ± 0.026
ε ($\pi \cdot \text{mm} \cdot \text{mrad}$)	0.004921 ± 0.000094
$\gamma\varepsilon$ ($\pi \cdot \text{mm} \cdot \text{mrad}$)	4.285 ± 0.082
Horizontal	
β_0 (m)	45.75 ± 0.13
α_0 (1)	-9.432 ± 0.029
γ_0 (m^{-1})	1.967 ± 0.013
ε ($\pi \cdot \text{mm} \cdot \text{mrad}$)	0.003380 ± 0.000052
$\gamma\varepsilon$ ($\pi \cdot \text{mm} \cdot \text{mrad}$)	2.943 ± 0.046

Table 6.1: Beam-parameters of the spike at the screen of LOLA for vertical and horizontal direction.

ing parameters are given in Tab. 6.1.

There will always be mixing between the particles of the tail and the particles of the spike. To really disentangle them, tomography is required. This method is not implemented during this thesis. A quick solution is to streak sufficiently, so that the tail is smeared out far enough, so that it only shows small intensity. At some point, one will see the effect of the streaking on the spike, and then the transverse and longitudinal sizes are intermingled. So, the trick is to find the point in between. This point is the point with the minimum vertical size of the spike on the screen in the above scan. Once this point is found, a quadrupole scan can be performed. [Hue05a]

6.3.3 Comparison of bunch parameters from different origins

The emittance of the whole bunch was measured behind BC2, one day before we made our measurement. The resulting normalized emittance was for the vertical direction

$$\varepsilon_y^n = \gamma\varepsilon_y = (4.285 \pm 0.082) \cdot \pi \cdot \text{mm} \cdot \text{mrad}$$

	Vertical bunch width (mm)	Horizontal bunch width (mm)
<i>half-theoretic:</i>		
17.04.2005,00:26	0.295 ± 0.134	0.694 ± 0.037
<i>measured at the screen of LOLA:</i>		
13.04.2005,19:49	0.318 ± 0.007	0.154 ± 0.004
13.04.2005,22:26	0.292 ± 0.006	0.148 ± 0.004
14.04.2005,13:33	0.145 ± 0.004	0.276 ± 0.008
15.04.2005,08:44	0.083 ± 0.002	0.205 ± 0.006
29.04.2005,06:33	0.437 ± 0.021	0.146 ± 0.008

Table 6.2: Widths of unstreaked bunches in vertical and horizontal direction. The "half-theoretical" value is calculated with Eq. (6.10) using the emittance, measured behind BC2, and the beta function, calculated by [Gol05]. The errors result from statistical considerations. Systematical effects are not contained.

and for the horizontal direction

$$\varepsilon_x^n = \gamma \varepsilon_x = (2.943 \pm 0.046) \cdot \pi \cdot \text{mm} \cdot \text{mrad} .$$

With these values and with the theoretical beta function at the OTR screen of LOLA, calculated by [Gol05], the width of the whole bunch can be calculated using Eq. (2.23) and Eq. (2.24)

$$\sigma_{x,y} = \sqrt{\frac{\varepsilon_{x,y}^n}{\pi \gamma^{(\text{screen})}} \cdot \beta_{x,y}^{(\text{screen})}} , \quad (6.10)$$

where $\sigma_{x,y}$ is the rms bunch-width at horizontal or vertical direction, $\varepsilon_{x,y}^n$ is the normalized emittance, measured at the diagnostic section behind BC2 and $\gamma^{(\text{screen})}$ and $\beta_{x,y}^{(\text{screen})}$ are the Lorentz factor and the theoretical beta function at the screen of LOLA. Tab. 6.2 compares these "half-theoretical" values with some bunch widths, measured at the screen of LOLA. The date specifications state when the corresponding measurement was made.

The high values of σ_x and σ_y can be attributed to a badly matched beam. This means, that the beam-parameters do not accord to the design values. Therefore, the horizontal, half-theoretical bunch width is much too high. The vertical widths are comparable. The differences between the measured values amount up to a factor 5. This indicates, that the optical setup of the accelerator was changed, between the measurements. The very small errors result only from statistical consideration. They contain no systematical effects. Such effects are for example space-charge effects or timing jitter, that causes variable arrival times at the accelerating modules and results in variable compressions in the bunch compressors.

7 Conclusion

The longitudinal bunch length and bunch shape are important parameters for the operation of the VUV-FEL. The transverse deflecting cavity LOLA IV was installed, to investigate the longitudinal structure of the electron bunches. An electro-magnetic radio-frequency (RF) wave travels with the bunch along the structure and streaks it vertically. An optical transition radiation (OTR) screen makes the longitudinal charge distribution visible.

During this thesis, LOLA was commissioned at the VUV-FEL. First images were taken with a synchronization, allowing to image the streaked bunch with a probability of 1/3. With an upgraded trigger generator, it was possible to synchronize LOLA to one bunch at each bunch train.

The imaging setup has been calibrated, yielding a resolution of the imaging setup of about $26 \mu\text{m}$ at the OTR screen per pixel of the CCD-camera. Because LOLA streaks the bunch vertically, the vertical axis of the screen has been calibrated, in order to measure the longitudinal dimension of the bunch. With a maximum RF power of 18 MW, the achievable streak amounts to 3.8 fs/pixel which corresponds to a resolution of 17 fs with a dedicated setup.

The power measurement-system has been upgraded with a second diode, to enlarge the dynamical range. The vertical streak of the bunch makes it necessary to utilize the whole vertical range of the OTR screen. Since the OTR sensitivity of the optical setup is position dependent, measurements for a correction of this effect had to be made.

LOLA separates the spike from the tail of the bunch. Therefore, it was possible to measure the emittance of the spike. The results are $\epsilon_x^n = (2.943 \pm 0.046) \pi \text{ mm mrad}$ and $\epsilon_y^n = (4.285 \pm 0.082) \pi \text{ mm mrad}$. The spike length was measured at $(137 \pm 14) \text{ fs}$ FWHM, corresponding to $(55.0 \pm 5.5) \text{ fs rms}$.

Investigations of the bunch shape revealed a double-spike structure. The distance of the two spikes depends on the phase of the RF in the accelerating modules. The total, FWHM, bunch length varies between 114 and 456 fs. A comparison with current simulations showed, that the used methods reproduce the basic features of the bunch shape. A detailed comparison, however, yields considerable differences which vary also depending on the computer code.

Outlook

An interesting parameter of the beam is the fraction of charge that is accumulated in the head of the bunch. To measure this, the number of the accumulated electrons of each pixel of the CCD in LOLA's camera becomes important. This number depends on the absorbed number of photons and on the setpoint of the gain of the camera. The yield of photo electrons in the CCD depends non-linearly on the intensity of the absorbed light. So, a calibration has to be done to obtain this curve at different gain setpoints. For that purpose, a method has to be developed by which the screen is illuminated uniformly. Additionally, the correlation between the total charge within the electron bunch and the sum of the pixel values has to be found. With the knowledge gained in this way, it should be possible to calculate the charge contained in every chosen fraction of the image. Possibly, a camera with a higher performance has

to be installed.

The resolution at the screen of LOLA, in terms of femtoseconds per pixel, is dependent on the current of the quadrupole 3, that is positioned between the cavity and the screen. To be independent of it, the calibration described in Sec. 5.5 has to be done for different quadrupole currents.

The measurement of the emittance of the spike presented in this thesis was done ignoring a mixing between the particles of the tail and the particles of the spike. A tomography has to be done to disentangle them. A measurement with the optimal streak is also possible. This means that the power of the RF in LOLA is high enough to separate the tail and the spike, and low enough to not streak the spike itself. At this operation point, where the vertical spike size is minimal, the quadrupole scan has to be redone.

Since a high peak current is essential for an optimal SASE production, the bunch length has to be reduced. Due to a folding over of the longitudinal phase-space distribution in the bunch compressors, a higher peak current than actual is hardly to achieve. With the installation of a third-harmonic cavity that will reshape the curvature impressed on the energy distribution, a folding over will be avoided and a smoother compression will be achievable. Possibly, a camera with a higher performance has to be installed.

A The Panofsky-Wenzel theorem

We consider a particle with the charge q and the velocity vector \mathbf{v} that travels fast enough parallel to the axis of the cavity. This direction is defined as the z -direction. The field distribution consists of pure TE- or TM-modes. The gained transverse momentum of the particle is assumed to be negligible compared to the longitudinal momentum. The infinitesimal, transverse momentum $d\mathbf{p}_\perp$ of the particle that travels in a time dt through the field can be calculated using the Lorentz force with

$$d\mathbf{p}_\perp(t) = \mathbf{F}_\perp(t) \cdot dt = q \cdot [\mathbf{E}_\perp(t) + (\mathbf{v} \times \mathbf{B})_\perp(t)] dt . \quad (\text{A.1})$$

The total transverse momentum gained in a cavity with the length L is

$$\Delta\mathbf{p}_\perp(L) = \frac{q}{v} \cdot \int_{z=0}^{z=L} [\mathbf{E}_\perp(z) + (\mathbf{v} \times \mathbf{B})_\perp(z)] dz . \quad (\text{A.2})$$

Here the integration variable was exchanged with $dt = dz/v$ where v is the norm of the velocity vector. The position $z=0$ determines, where the particle enters the cavity and $z=L$ where it leaves. If we have no free charges producing the field distribution, we can introduce the vector potential \mathbf{A} and substitute the electric and magnetic field using

$$\mathbf{E} = -\frac{\partial\mathbf{A}}{\partial t} \quad \text{and} \quad \mathbf{B} = \nabla \times \mathbf{A} . \quad (\text{A.3})$$

With the double vector product¹ this leads to

$$\Delta\mathbf{p}_\perp(L) = q \cdot \int_{z=0}^{z=L} \left[-\left(\frac{1}{v} \frac{\partial}{\partial t} + \frac{\partial}{\partial z} \right) \cdot \mathbf{A}_\perp(z) + \nabla_\perp \mathbf{A}_z(z) \right] dz . \quad (\text{A.4})$$

The first term of the right side is the total differential of the transverse vector potential. So, we can write

$$\Delta\mathbf{p}_\perp(L) = -q \cdot \int_{\mathbf{A}_\perp(z=0)}^{\mathbf{A}_\perp(z=L)} d\mathbf{A}_\perp(z) + q \cdot \int_{z=0}^{z=L} \nabla_\perp \mathbf{A}_z(z) dz . \quad (\text{A.5})$$

Assuming that the fields have a harmonic time dependence and complex amplitudes $\underline{\mathbf{A}}_\perp(z)$, $\underline{\mathbf{E}}_\perp(z)$ Eq. (A.3) yields

$$\underline{\mathbf{A}}_\perp(z) \cdot e^{i\omega t} = \frac{i}{\omega} \underline{\mathbf{E}}_\perp(z) \cdot e^{i\omega t} , \quad (\text{A.6})$$

with $t = z/v$. The transverse momentum change is the real part of Eq. (A.5)

$$\Delta\mathbf{p}_\perp(L) = \Re \left\{ -\frac{iq}{\omega} \cdot \int_{\underline{\mathbf{E}}_\perp(z=0)}^{\underline{\mathbf{E}}_\perp(z=L) \cdot e^{i\omega L/v}} d(\underline{\mathbf{E}}_\perp(z) \cdot e^{i\omega z/v}) + \frac{iq}{\omega} \cdot \int_{z=0}^{z=L} \nabla_\perp \underline{\mathbf{E}}_z(z) \cdot e^{i\omega z/v} dz \right\} . \quad (\text{A.7})$$

Because the electric field is always perpendicular to conductive surfaces, the first integral

$$\Delta\mathbf{p}_\perp^{(1)}(L) = \Re \left\{ -\frac{iq}{\omega} \cdot (\underline{\mathbf{E}}_\perp(z=L) \cdot e^{i\omega L/v} - \underline{\mathbf{E}}_\perp(z=0)) \right\} = 0 \quad (\text{A.8})$$

vanishes, if the cavity has walls perpendicular to the axis at both ends. If we insert beam openings, it vanishes only

¹ $\mathbf{a} \times (\mathbf{b} \times \mathbf{c}) = \mathbf{b} \cdot (\mathbf{a}\mathbf{c}) - \mathbf{c} \cdot (\mathbf{a}\mathbf{b})$

if the frequency is below the cut-off². Then the marginal transverse field is attenuated at the entry and the exit, so that this integral can be neglected also in this case.

In case of a negligible $\Delta\mathbf{p}_\perp^{(1)}$ the second term determines the whole gained transverse momentum

$$\Delta\mathbf{p}_\perp^{(2)}(L) = \Re \left\{ \frac{iq}{\omega} \cdot \int_{z=0}^{z=L} \nabla_\perp \underline{\mathbf{E}}_z(z) \cdot e^{i\omega z/v} dz \right\} . \quad (\text{A.9})$$

This is called the Panofsky-Wenzel theorem. An ultra-relativistic particle is deflected, if there is a non-zero, transverse, gradient of the longitudinal component of the electric field. For references see [Nag04] and [Wan98].

² The cut-off frequency is the smallest frequency with which the wave can propagate in a certain waveguide.

B Tables

Power at display (MW)	Real Power (MW)
0.8	0.5
1.0	0.6
1.2	0.8
1.6	1.0
2.0	1.3
2.4	1.6
3.1	2.0
3.9	2.5
4.6	3.2
5.8	4.0
7.0	5.0
8.2	6.3
9.9	7.9
11.6	10.0
13.3	12.6
15.8	15.8
18.3	20.0
20.8	25.1
24.3	32.0
27.9	39.8
31.4	50.1
35.2	63.1
39.0	79.4
42.8	100.0

Table B.1: Calibration of the RF power measurement. The power of a pre-calibration shown in a display of a control panel compared with the real RF power measured with a network analyzer. [Jon04]

Phase at display (deg)	Voltage at shifter (V)	Real Phase (deg)
180.0	4.0036	263.70
170.0	3.8927	244.90
160.0	3.7822	226.33
150.0	3.6707	207.70
140.0	3.5597	189.14
130.0	3.4493	170.79
120.0	3.3379	152.97
110.0	3.2271	135.90
100.0	3.1156	119.67
90.0	3.0050	104.30
80.0	2.8941	89.47
70.0	2.7828	74.82
60.0	2.6720	60.70
50.0	2.5615	47.22
40.0	2.4491	34.28
30.0	2.3383	22.02
20.0	2.2276	10.32
10.0	2.1161	-1.05
0.0	2.0055	-11.26
-10.0	1.8948	-20.10
-20.0	1.7833	-30.20
-30.0	1.6727	-39.00
-40.0	1.5611	-47.40
-50.0	1.4506	-55.40
-60.0	1.3397	-62.90
-70.0	1.2282	-70.20
-80.0	1.1176	-77.30
-90.0	1.0068	-84.00
-100.0	0.8952	-90.50
-110.0	0.7844	-96.80
-120.0	0.6739	-103.00
-130.0	0.5627	-109.00
-140.0	0.4517	-115.00
-150.0	0.3411	-120.80
-160.0	0.2298	-127.00
-170.0	0.1190	-133.10
-180.0	0.0079	-138.90

Table B.2: Behavior of the phaseshifter measured with a network analyzer. The table contains the phase that the display on the control panel shows, the voltage at the phaseshifter and the real phase measured with a network analyzer. The data originate from [Fri05b].

Attenuation (dB)	Setpoint at display	Power at display (MW)
26.066	1.788	15.82
23.409	1.166	10.92
19.949	0.968	4.519
15.826	0.848	1.472

Table B.3: A precise power measurement using attenuators. Via a series of different attenuators some setpoints with a well known RF power are found. Starting at a power of 15.8 MW the attenuation was decreased in several steps. To do the resolution calibration (see Sec. 5.5), we choose the setpoint at 0.848.

References

- [Alt64] O. H. Altenmueller, R. Larsen, and G. Loew. *Investigations of Traveling-Wave Separators for the Stanford Two-Mile Linear Accelerator*. The review of scientific instruments, Vol. 35(4), April 1964.
- [And00] J. Andruszkow, B. Aune, and V. Ayvazyan. *First Observation of Self-Amplified Spontaneous Emission in a Free-Electron Laser at 109 nm Wavelength*. Phys. Rev. Lett., 85:3825–3829, 2000.
- [Beu05] B. Beutner, 2005. Private Communication.
- [Bor05] M. Borland. <http://www.aps.anl.gov/asd/oag/oagPackages.shtml>.
- [Bri01] R. Brinkmann et al. *TESLA: The superconducting electron positron linear collider with an integrated X-ray laser laboratory. Technical design report. Part II: The accelerator*. Technical report, DESY-01-011, 2001.
- [Bro82] K. L. Brown. *A First- and Second-Order Matrix Theory for the Design of Beam Transport Systems and Charged Particle Spectrometers*. SLAC-75, 1982.
- [Der95] Y. S. Derbenev, J. Rossbach, E. L. Saldin, et al. *Microbunch Radiative Tail-Head Interaction*. Tesla-FEL 95-05, September 1995.
- [Doh05] M. Dohlus. Private Communication.
- [Doh04] M. Dohlus. <http://www.desy.de/~dohlus/CSRtrack/>.
- [Doh03] M. Dohlus. *Two methods for the Calculation of CSR Fields*. TESLA-FEL-2003-05, 2003.
- [Doh00] M. Dohlus, A. Kabel, and T. Limberg. *Efficient Field Calculation of 3D Bunches on General Trajectories*. Nuclear Instruments and Methods in Physics Research A,, 445:338–342, 2000.
- [Edw95] D. A. Edwards. *TESLA Test Facility Linac - Design Report*. Technical report, DESY Print, TESLA 95-01, 1995.
- [Emm00] P. Emma, J. Frisch, and P. Krejcik. *A Transverse RF Deflecting Structure for Bunch Length and Phase Space Diagnostics*. In: Proceedings of the 2001 Particle Accelerator Conference, Chicago, Illinois U.S.A. 2001.
- [Flo00] K. Floettmann, September 2000. http://www.desy.de/~mpyflo/Astra_dokumentation/.
- [Flo01] K. Floettmann, T. Limberg, and P. Piot. *Generation of Ultrashort Electron Bunches by cancellation of nonlinear distortions in the longitudinal phase space*. TESLA FEL Report 2001-06, 2001.
- [Fro05] L. Fröhlich. *Bunch Length Measurements Using a Martin-Puplett Interferometer at the VUV-FEL*. Master’s thesis, Department of Physics of the University of Hamburg, 2005.
- [Fri05b] J. C. Frisch, D. McCormick, and T. Smith, 2005. Private Communication.
- [Fri05a] J. C. Frisch and T. Smith, 2005. Private Communication.
- [Gei99] M. A. Geitz. *Investigation of the Transverse and Longitudinal Beam Parameters at the TESLA Test Facility Linac*. Ph.D. thesis, Department of Physics of the Universität Hamburg, 1999.
- [GF45] V. L. Ginzburg and I. M. Frank. *Radiation of a uniformly moving electron due to its transition from one medium into another*. Journ. Phys. USSR, 9:353, 1945.
- [Gol05] N. Golubeva. Private Communication.
- [Hue03] M. Hüning and H. Schlarb. *Measurement of the Beam Energy Spread in the TTF Photo-Injector*. In: Proceedings of the 2003 Particle Accelerator Conference, Portland, Oregon U.S.A. 2003.
- [Hon04] K. Honkavaara. *Commissioning of the TTF linac injector at the DESY VUV-FEL*, August 2004. Presentation, FEL Conference 2004, Trieste, Italy.
- [Hue05a] M. Huening, 2005. Private Communication.
- [Jon04] R. Jonas. *Dioden zu Leistungsmessung bei LOLA*, 23.07.2004. Measuring data.
- [Kim05a] Y. Kim. <http://www.desy.de/~yjkim/TTF2/>.
- [Kim05] Y. Kim, 2005. Private Communication.
- [Lam83] R. L. Lamberts. *Use of Sinusoidal Test Patterns for MTF Evaluation*. Technical report, Sine Patterns LLC, 1983.
- [Lee99] S. Y. Lee. *Accelerator Physics*. World Scientific Publishing Co. Pte. Ltd., 1999.
- [Loe05] F. Löhl. *Measurements of the Transverse Emittance at the VUV-FEL*. Master’s thesis, Department of Physics of the University of Hamburg, 2005.
- [Loe65] G. Loew and O. H. Altenmueller. *Design and applications of rf separator structures at SLAC*. August. Paper presented at the fifth Int. Conf. on High-Energy Accelerators, Frascati, Italy, 1965.
- [Nag04] M. Nagl. *Physics of the Transverse R.F. Deflecting Structure*, 2004. Presentation, DESY, Hamburg.

- [Pan56] W. K. H. Panofsky and W. A. Wenzel. *Some Considerations Concerning the Transverse Deflection of Charged Particles in Radio-Frequency Fields*. Review of Scientific Instruments, 27:967, November 1956.
- [Ros05] J. Rossbach. Vorlesungsskript: *Teilchenbeschleuniger*. Department of Physics of the University of Hamburg.
- [RS93] J. Rossbach and P. Schmüser. *Basic course on accelerator optics*, 1993. Lectures given at the CERN Accelerator School, DESY internal report M-93-02.
- [Sch01] H. Schlarb. *Collimation System for the VUV Free-Electron Laser at the TESLA Test Facility*. Ph.D. thesis, University of Hamburg, 2001.
- [Sch05] H. Schlarb, M. Roehrs, and M. Huening. *Slice emittance measurement at TTF*, 2005. Presentation, DESY, Hamburg.
- [Sch04] S. Schreiber. *Commissioning of the VUV-FEL Injector at TTF*. Proceedings of EPAC 2004, Lucerne, Switzerland, 2004.
- [Sla46] J. C. Slater. *Microwave Electronics*. Rev. Mod. Phys., 18:441–512, 1946.
- [Stu04] F. Stulle. *A Bunch Compressor for Small Emittances and High Peak Currents at the VUV Free-Electron Laser*. Ph.D. thesis, Deutsches Elektronen-Synchrotron, Hamburg, 2004.
- [XFEL] The European X-Ray Laser Project XFEL. <http://xfel.desy.de/>.
- [TFR02] The TESLA Test Facility FEL team. *SASE FEL at the TESLA Facility, Phase2*. TESLA FEL Report 2002-01, 2002.
- [Wab02] H. Wabnitz, L. Bittner, A. R. B. de Castro, et al. *Multiple ionization of atom clusters by intense soft X-rays from a free-electron laser*. Nature, 420:482–485, 2002.
- [Wan98] T. P. Wangler. *RF Linear Accelerators*. John Wiley & Sons, Inc., 1998.

Acknowledgements

I would like to thank Prof. Dr. Jörg Roßbach. You was always able to enthuse me again, for the various issues of accelerator physics. I will miss the seldom but very interesting discussions in the canteen, when you picked an empty sheet of paper out of your pocket and began to sketch a current problem of the linac. It was very motivating to know that also the opinion of a little student matters.

Not less, I would like to thank Prof. Dr. Hans Fraas. Without you, an external diploma thesis at the VUV-FEL had not been possible. In addition, it was always a pleasure to listen to your lectures during the two years in Würzburg. Thanks for all support and suggestions.

I am grateful to my supervisor Dr. Markus Hüning. You always stayed cool while I annoyed you with stupid questions and with problems, I did not understand, even after several explanations. In particular, during the last weeks of my thesis you helped very much by correcting my stupid writings. Thanks a lot!

I also want to thank the fellows who shared the office with me, Bolko Beutner, Lars Fröhlich, Florian Löhl and Kirsten Hacker. Without your support, I had not been able to finish my thesis that fast. It was always pleasant to discuss about physical and non-physical issues.

A special thank goes to Bolko Beutner. You bailed me out of many dilemmas and desperations with your large knowledge and grasp. You helped to manage the problem and to not loose my head. Thanks for being a friend.

I want to thank my American colleagues Marc Ross, Joe Frisch, Doug McCormick and Tonee Smith for advice with LOLA.

Thanks to all of you, who tried to improve my poor English in this thesis: Dr. Siegfried Schreiber, Dr. Markus Hüning, Kirsten Hacker, Lars Fröhlich, Florian Löhl, Dr. Christopher Gerth, Dr. Paul Jonathan Phillips, Dr. Bernd Steffen, Dr. Nicoleta Baboi, Bolko Beutner, Dr. Yujong Kim, Dr. Hossein Delsim-Hashemi, Dr. Ernst-Axel Knabbe.

I also want to thank all the colleagues of the VUV-FEL shift crew for providing beam time for measurements and for instructive shifts.